UNIVERSITÀ DI TRENTO
Department of Industrial Engineering

Doctoral School in Materials, Mechatronics and Systems Engineering

XXXVII cycle

Development of P-3DP (Powder-based 3D Printing) technologies for the production of cement-based materials

MURSALEEN SHAHID

JUNE 2025

DEVELOPMENT OF P-3DP (POWDER-BASED 3D PRINTING) TECHNOLOGIES FOR THE PRODUCTION OF CEMENT-BASED MATERIALS

MURSALEEN SHAHID

E-mail: MursaleenShahid@live.com

Approved by:

Prof. Vincenzo M. Sglavo, Advisor
Department of Industrial Engineering
University of Trento*, Italy.*

Prof. Gian Domenico Soraru,Co-advisor
Department of Industrial Engineering
University of Trento*, Italy.*

Ph.D. Commission:

Prof.Mattia Biesuz,
Department of Industrial Engineering
University of Trento*, Italy.*

Prof. Enrico Bernardo,
Department of Industrial Engineering
University of Padua*, Italy.*

Prof. Gianfranco Dell'Agli,
Department of Civil and Mechanical Engineering
University of Cassino and Southern Lazio*, Italy.*

University of Trento,

Department of Industrial Engineering

JUNE 2025

University of Trento - Department of Industrial Engineering

Doctoral Thesis
MURSALEEN SHAHID – 2025
Published in Trento (Italy) – by University of Trento

I am dedicating this thesis to my parents, whose solid support, inspiration and sacrifices have been the backbone of my academic career. My father served as a mentor throughout my whole life. The love of parents and guidance have shaped my journey and this effort is a testament to their endless dedication.

Preface

The work presented in this thesis has been previously published in the form of three peer-reviewed journal articles:

1. Shahid M, Sglavo VM (2024) Binder Jetting 3D Printing of Binary Cement—Siliceous Sand Mixture. Materials 2024, Vol 17, Page 1514 17:1514. https://doi.org/10.3390/MA17071514

2. Shahid M, Sglavo VM (2024) Effect of water-to-quick setting cement ratio and aggregate size on mechanical properties and dimensional accuracy of binder jetting 3D-printed bodies. Open Ceramics: https://doi.org/10.1016/j.oceram.2024.100704

3. Shahid M, Pierre A, Cousture A, Sglavo VM.(2025) Selective Alkali Activation of Limestone for Additive Manufacturing in Construction: Influence of Alkali Concentration on Physical and Mechanical Properties. Applied Sciences; 15(8):4453. https://doi.org/10.3390/app15084453

Abstract

This thesis represents an effort to optimally investigate the processes involved in binder jetting 3D printing of cementitious materials by systematically studying the effects some key processing variables have on structural and dimensional performance variation of the printed components. Binder jetting has the potential for complex geometries with high precision, along with minimum material waste, which is yet to be transformed into consistent mechanical strength and dimensional accuracy, especially when scaling from the laboratory to industrial applications. This paper presents the printing of quick-setting cement-based materials using a binary cement system composed of ordinary Portland cement and quick-setting cement. The critical parameters that received most of the research effort included the water-to-cement ratio, the particle size of the siliceous sand aggregates-namely, coarse versus fine OPC: QSC mix proportion, and the layer thickness used during printing.

The experiments were conducted by fabricating specimens under different conditions using blended dry powders and deionized water. The printed products were then tested in terms of dimensional accuracy, compressive strength, and flexural strength. It follows that changes in the w/c ratio and aggregate size have a direct impact both on mix flowability and bond formation at the interlayer surface, and consequently on the mechanical performance and print fidelity of the final product. Additionally, the investigation on the binary cement mix goes on to reveal that OPC content plays a vital role in strength development and the optimum mechanical properties emerge at certain OPC:QSC ratios, especially with coupled reduced layer thickness.

Further research based on these findings now examines the mutual relationships between these variables in an integrated framework that relates process parameters to performance attributes. Lastly, this research investigates how scaling of the optimized parameters, obtained under controlled conditions in the laboratory, can be done to industrial production with the view to identify modifications that are

necessary to realize enhanced structural integrity and precise dimensional control under actual construction conditions.

The integrated approach presented in this paper will provide an advanced understanding of BJ3DP for cementitious construction and open up opportunities for more reliable, cost-effective, and scalable additive manufacturing in the construction industry.

Research Motivation

Binder jetting 3D printing (BJ3DP) of cementitious materials has recently become one of the latest fabrication technologies that might eventually revolutionize the construction industry in fabricating highly geometrically complex and precise objects. Although several initial studies illustrated that BJ3DP can realize innovative architectural forms with a minimum waste of materials, substantial understanding gaps still existed regarding how main processing parameters influenced the final properties of the printed components in cementitious materials. Thus, the present research is motivated by the need for an integrated study aimed at the systematic investigation and optimization of multiple processing variables, such as the w/c ratio, aggregate particle size, binary cement mix proportions, and layer thickness, to advance both the mechanical performance and dimensional accuracy of BJ3DP-fabricated materials.
There is a general challenge in the BJ3DP process, striving for an ideal balance between flowability, bonding of successive layers, and high-speed strength. The W/C not only dictates the rheological behaviour of the cementitious mixture but also acts as one of the decisive parameters in the achievement of early age strength during its hydration course. Meanwhile, aggregates of siliceous sand from coarse to fine size are significant in the viewpoint of powder bed packing density and uniform interlayer bonding. While overly large aggregates can prevent extrusion and lose dimensional fidelity, too small aggregates can affect strength adversely and lead to problems in workability. The following study will thus be based on the question of how changes in both the w/c ratio and aggregate size affect important performance attributes such as compressive and flexural strength and overall dimensional accuracy.

Besides these issues, the paper investigates the properties of binary cement sand mixture proportions by OPC:QSC mix ratio variation. While OPC shows excellent mechanical performance, its moderate setting time provides a limitation toward rapid printing techniques. On the other hand, QSC shows a faster setting, allowing better

stability after the building of layers-but its contribution could be diverse concerning long-term strength. The determination of an optimum blend which can provide a balance between speedy layer consolidation and high mechanical performance is one critical aspect of the work. These benefits can provide the ability to design and construct structurally optimized and geometrically intricate cementitious structures that are unattainable with traditional construction techniques.

Of paramount importance as a variable, too, is layer thickness, since it defines the resolution or surface finish the object is to be printed, as well as the strength in the interlayer connections. This study is meant to explain how these parameters will relate to each other. Understanding the interactions between the w/c ratio, aggregate size, mix proportions, and layer thickness will facilitate an integrated process model to predict performance outcomes more reliably than studies addressing these factors individually.

The motivation for this thesis is that it can further the field of cementitious BJ3DP by bridging some of the gaps in current research: integrating multiple processing variables into one coherent optimization strategy that improves structural integrity and dimensional control and assessing the scalability of such improvements for industrial application.

Organization of the Thesis

This thesis consists of six main chapters that address different topics of binder jetting additive manufacturing of cement-based materials. The chapters are arranged in an order that ensures they address a comprehensive overview, starting from the fundamentals of additive manufacturing, followed by the developed 3D printing system, experimental research, and concluding with conclusions and recommendations. The organization ensures a logical progression from theory to practice and analysis.

The first chapter "**Introduction"** offers a general background on additive manufacturing (AM) and its significance, along with its various classifications. The chapter begins with the developmental history of AM and describes the required steps involved in the process. It then describes the several categories of AM processes, including material extrusion, vat photopolymerization, powder bed fusion (PBF), material jetting, binder jetting, directed energy deposition, and sheet lamination. Each process is described according to its mode of working and applications. In addition, the chapter elaborates on the materials applied in AM, that is, concrete 3D printing materials. Different classes of materials, including cementitious binders (cement, geopolymers, magnesium potassium phosphate cement), aggregates, fillers, admixtures, and fiber reinforcements, are detailed extensively. The chapter also provides information on the historical evolution of cement-based additive manufacturing, leading to the research work presented in the following chapters.

The second chapter "**Binder Jetting and Schematic of customized printer**" explains, the working principle of binder jetting, which is one of the main AM processes studied in this research, is described. It begins with the description of the important processes in binder jetting, i.e., powder spreading, compaction, and binder drop formation, which have a significant effect on the printed structure quality.

The latter half of chapter one describes the altered 3D printing machinery designed to perform this research. The individual components, i.e., the binder unit, the valve, the

manifold, and the nozzle, are separately described highlighting the role these units serve in helping deliver precision as well as continuity to the printed shape.

Chapters III and IV present the experimental work that forms the core of this work already published. **Chapter III** "**Effect of water-to-quick setting cement ratio and aggregate size on mechanical properties and dimensional accuracy of binder jetting 3D-printed bodies**"corresponds to the first published paper and investigates the 3D-printed properties of a quick-setting cement-based material. Including dimensional stability and printability, different parameters were studied including the influence of water to quick setting cement ratio and aggregate size on the mechanical properties of 3d printed specimens. Lastly, the chapter concludes with a summary of the major findings and their relevance to the optimization of binder jetting of cement-based materials.

Chapter IV "Binder Jetting 3D Printing of Binary Cement—Siliceous Sand Mixture" corresponds to the second paper published and addresses printing a siliceous sand binary blend. The chapter used two kinds of cement quick-setting cement and ordinary Portland cement in order to examine the various mechanical properties of the printed parts.

The next chapter "**Conclusion**" draws a conclusion based on all the research findings, where several critical aspects are discussed. The chapter concludes with discussions on future research directions, identifying the potential areas and the necessary improvements in the binder jetting 3d printing process.

The **appendix** has additional results of experiments and is the third paper work with the title "**Selective Alkali Activation of Limestone for Additive Manufacturing in Construction: Influence of Alkali Concentration on Physical and Mechanical Properties**". It provides further information that corroborates the thesis findings. The study examines the important parameters such as the influence of the NaOH concentration on the physical and mechanical strength. It also analyzes the impact of binder formulation on specimen stability and printability in general. The outcomes

show that sodium hydroxide level affects the strength of the material, with high concentrations leading to reduction in strength.

Table of contents

Table of Figures

Chapter 1: Introduction

Chapter 2: Binder Jetting and Schematic of customized printer

Chapter 3: Effect of water-to-quick setting cement ratio and aggregate size on mechanical properties and dimensional accuracy of binder jetting 3D-printed bodies

Chapter 4: Binder Jetting 3D Printing of Binary Cement—Siliceous Sand Mixture

Chapter 6: Appendix – Selective Alkali Activation of Limestone for Additive Manufacturing in Construction: Influence of Alkali Concentration on Physical and Mechanical Properties

List of Tables

Introduction

Three-dimensional (3D) concrete printing by binder jetting is emerging as a digital construction technology with the potential to make considerable savings in labor costs, material waste, and building time, while enabling previously unimaginable architectural complexity. This process relies mainly on the controlled deposition of liquid binder onto a bed of cementitious powder, layer by layer, to enable complex geometry without the need for traditional formwork.

Research has put increasing focus on maximizing the interaction between binder composition and powder bed material. Tuning of binder dosage, such as setting accelerators and rheology modifiers, is of primary concern in getting rapid curing and good interlayer bonding. At the same time, powder formulation is generally optimized through the inclusion of additional cementitious materials for improving particle packing and shrinkage reduction and thereby to the overall mechanical integrity of the printed part. One of the key issues in binder jetting is managing the interface between the cementitious powder and the binder. Even distribution of the binder is essential to avoid defects and maintain uniform mechanical performance. Material engineering and printer design have been driven by the need to address these issues to achieve adequate penetration and consolidation of the printed layers to the desired level of mechanical performance.

1.1 Additive Manufacturing

Additive manufacturing (AM) is a technology of constructing objects by depositing layers of materials in sequence. This enables the fabrication of complex structures and geometries that could not be realized by conventional manufacturing.

1.2 Steps involved in AM

The AM process involves mainly eight steps, starting from the CAD file to the application [8]. These include preparation of the CAD file, conversion into STL format, transfer to the AM machine, setup of the machine, building the object, removal of the

object, post-processing, and application of the finished product. These steps are followed by almost all types of printers, as shown in Figure I.

Every additive manufacturing part starts with a software model of its external geometry. That model can be created in one of several professional CAD solid modelling packages provided it exports a 3D representation of the solid or surface. Alternatively, the representation can be captured using reverse engineering methods such as laser scanning. In the next step, the CAD file is converted into STL format where the STL file guarantees that the part must be transferable to the AM machine via GCODE or NC file.

The 3D printing machine is properly set up before the start of the build process. Once the file is transferred to the machine, parameters like size, position and orientation for the building must be considered. Step five is the automatic building of the specimen and in most cases, it doesn't need any supervision except some techniques that need a continuous supply of materials. After that removal of the specimen is done and the temperature is lower than before. Postprocessing involves the removal of support or de-powdering the excess powder. At this stage, the parts are usually weaker and are called green specimens. However, some techniques require additional treatments like a painting to achieve additional surface finishing and textures or heat treatment for a specific time and then the part is ready for application.

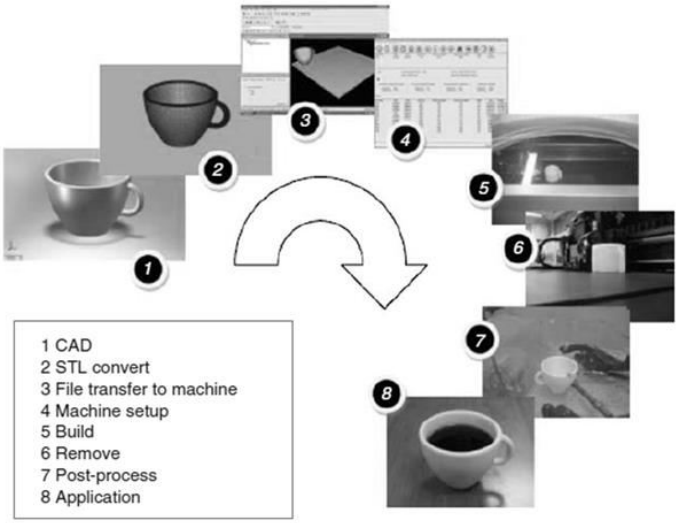

Figure I: Steps involved in the AM process [1]

1.3 Raw Material

Figure II provides an overview of the types of materials used in AM. Additive manufacturing is one of several processes that fabricates a 3D object by layer-by-layer building directly from a digital 3D model. The process begins with a 3D computer-aided design, which undergoes a "1st Layering Operation" and "Tool Path" generation to drive an additive process, potentially using the following material types:

• **Liquids**: Liquid materials include photopolymer resins that are mainly used in processes like stereolithography, where the light source cures the liquid resin layer by layer to form the object.

• **Sheets:** Sheet materials come in thin lays of metal or plastic laminated and cut to shape. There is another process called Laminated Object Manufacturing, which involves the bonding and cutting of each sheet layer by layer to build up the desired shape.

• **Wires:** In most of the processes, like Wire Arc Additive Manufacturing (WAAM), the normally used wire material is metals. A wire is melted and deposited layer by layer to build the final structure.

• **Powders:** Powder materials, including metals, polymers, and ceramics, are normally used in processes such as Selective Laser Sintering (SLS) or Electron Beam Melting (EBM). In each process, each layer of powder is selectively fused by a heat source. However, the Binder jetting technique uses powder as well as liquid supply without using any heat source.

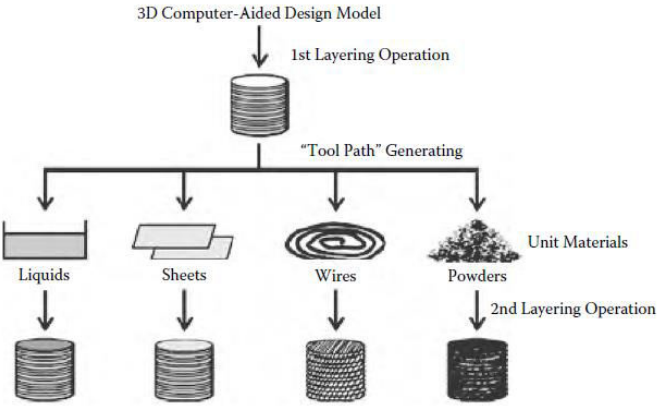

Figure II: Fabrication of a specimen with various unit materials [2]

1.4 Types of Additive Manufacturing

Additive manufacturing is mainly classified into seven types as per ASTM [3]. Binder jetting, material extrusion, material jetting, sheet lamination, VAT photopolymerization, powder bed fusion and direct energy deposition are seven different types of additive manufacturing.

1.4.1 Material extrusion

The process follows the dispersion of materials through an orifice or a nozzle. Fused deposition modelling (FDM), direct ink writing (DIW) or robocasting follows this technique. The process mainly involves melting the filament and depositing it in a two-dimensional plane and the process repeats for the next layer until the required 3D geometry is obtained as shown in Figure III. Material extrusion has become one of the most typical methods adopted by 3D printing processes from cement-based materials.

A formable cementitious mixture is compelled through a nozzle while structuring layer by layer. Typical configuration: raw material storage container, mixers, pump, and nozzle mounted on robotic arm or gantry system. It can be observed that the computer-controlled system deposits material precisely according to a pre-designed pattern, thus enabling the fabrication of complex geometries without formwork. Schematic of the process is available in the study "Fresh and Hardened Properties of Extrusion-Based 3D-Printed"[4].

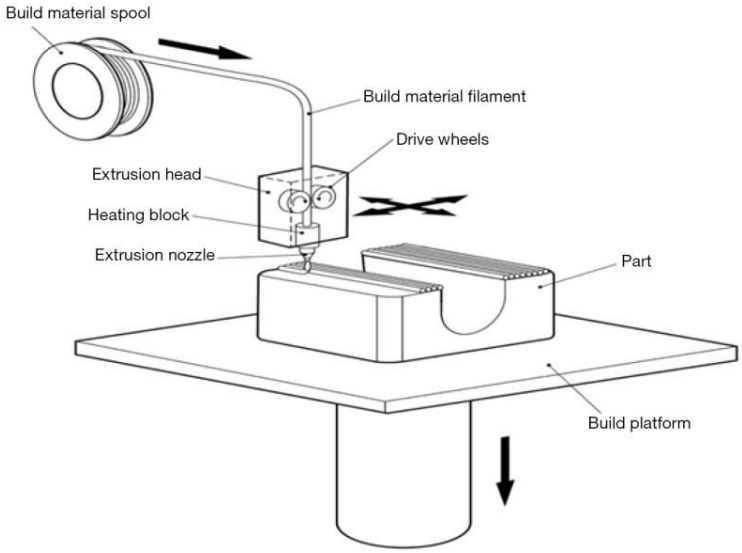

Figure III: Schematic diagram of material extrusion printing [5]

1.4.2 Vat photopolymerization

In this process, 3D objects are printed using a vat of liquid photopolymer resin. Selectively, a light source UV laser or projector cures or hardens the resin in those areas to build up each layer of the object. After a layer has been cured, the build platform moves and forms the next layer until an object is built up layer by layer, as in the case of Stereolithography (SL) (Figure IV).

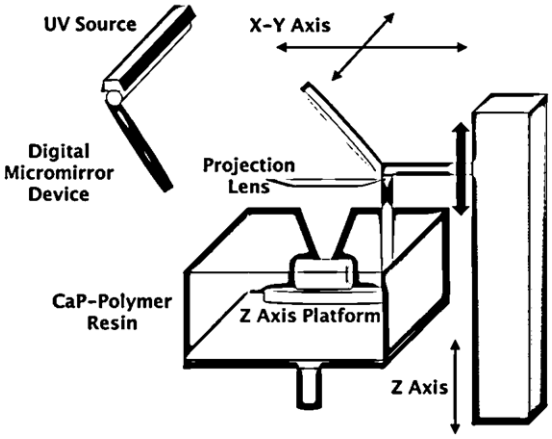

Figure IV: Schematic of Vat-photopolymerization [6]

1.4.3 Powder bed fusion (PBF)

This process of additive manufacturing fabricates three-dimensional objects by fusing layers of powdered material with the help of a heat source, mostly a laser or electron beam (Figure V). First, a thin layer of powder is spread over the build platform. Then, the heat source selectively fuses specific areas of the powder bed according to the digital design of the object. This process is repeated layer by layer until the entire part is formed.

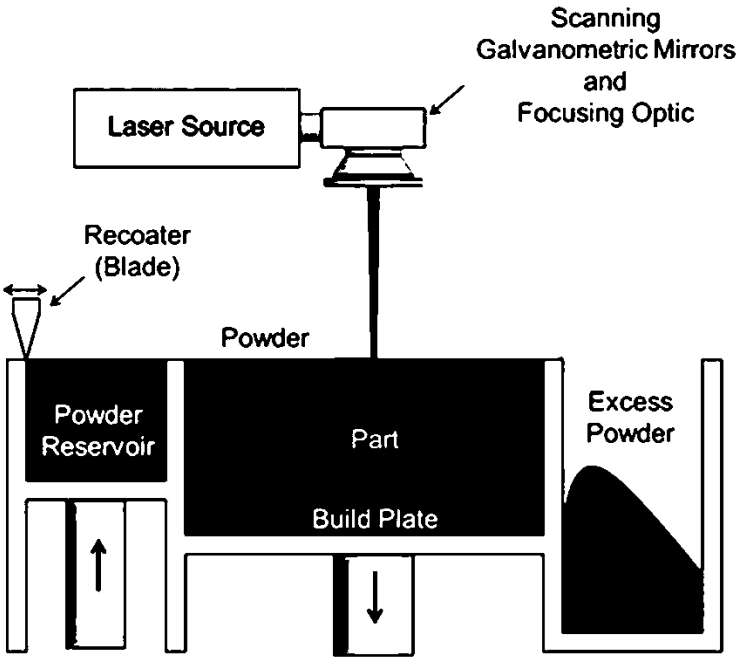

Figure V: Schematic of the laser powder bed fusion (LPBF) [7]

1.4.4 Material jetting

It follows the droplets of the build material that are selectively deposited e.g. direct inkjet printing (DIP) (Figure VI)

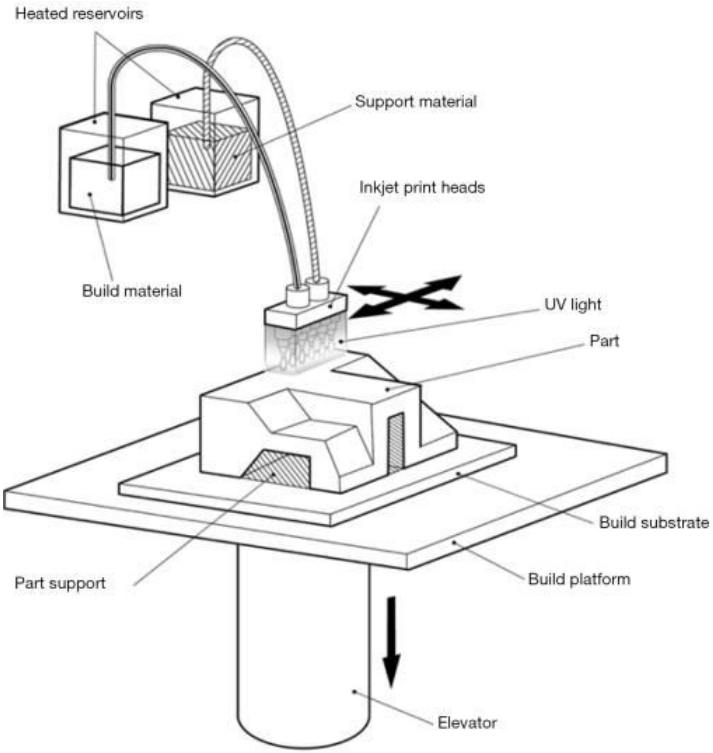

Figure VI: Schematic of material jetting 3D printing[5]

1.4.5 Binder jetting

This technique uses liquid as a binding agent to selectively deposit and join the powder materials, whereas powder-based 3D printing follows this method. Binder jetting is an additive manufacturing process in which three-dimensional objects are built in a layer-by-layer fashion, the selective deposition of a liquid binder onto a powder bed. In this process, a thin layer of powdered material, ceramic, or even sand is initially spread across the build platform. A print head, in concept similar to those used in inkjet printers, moves over the surface of the bed, jetting droplets of binder onto specific areas as defined by the digital model as shown in Figure VII. The binder acts as an adhesive, bonding together the powder particles into the cross-sectional

layer of the desired object. Once a layer is complete, the build platform lowers, and a fresh layer of powder is spread over the surface area. The process is continued until the entire part is formed. After printing, the unbound powder is removed, and additional post-processing, such as curing or sintering, might be done to give more strength and properties to the parts. There is the ability to make complex geometries without supports, and generally, there are high speeds of production with a wide variety of materials.

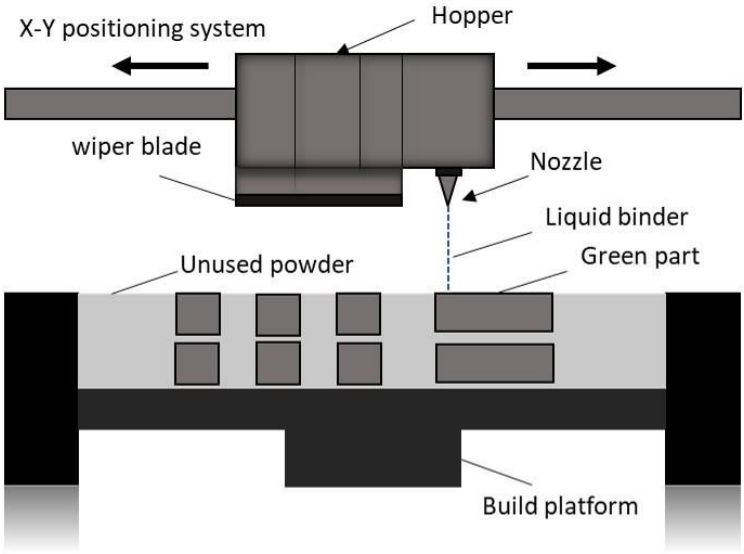

Figure VII: Schematic of binder jetting 3D printing

1.4.6 Directed Energy Deposition

The process fabricates or repairs a component by melting and depositing the material simultaneously. This process is accomplished by focusing an energy source onto a substrate (such as a laser, electron beam, or plasma arc), while concurrently feeding the material, in powder or wire form, into the melt pool (Figure VIII).

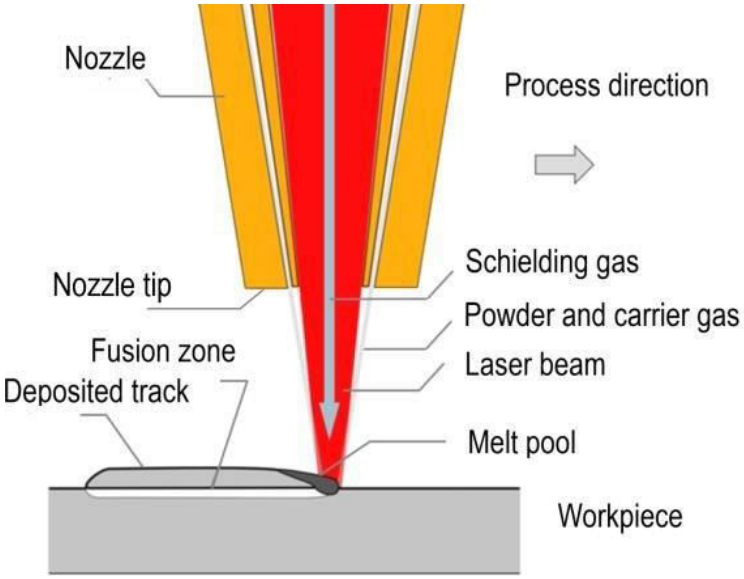

Figure VIII: Schematic of Direct energy deposition using co-axial nozzle [8]

1.4.7 Sheet lamination

An object is formed by bonding sheets of materials like in laminated object manufacturing (LOM). The 3D printing process of sheet lamination builds three-dimensional parts by stacking and bonding sheets of a given material. Essentially, the process involves placing a sheet on the platform where the model is to be built. The sheet is precisely cut utilizing a cutting tool, most often a laser or a blade, to adapt to the geometry of the section in question set by the 3D model. After it is cut, it's bonded to the previous layer with adhesives, heat, pressure, or ultrasonic welding, depending on the material type and how it is bonded as shown in Figure IX.

This layer-by-layer sequence would continue until the creation of a full object. In post-processing, the extra material surrounding the part is removed to reveal the structure. Some of the most important advantages of sheet lamination are the real process speed combined with low costs, which also allows compatibility with multi-material processes. Producing very little waste and not requiring complex support structures, it's also a very efficient method of producing large parts or prototypes.

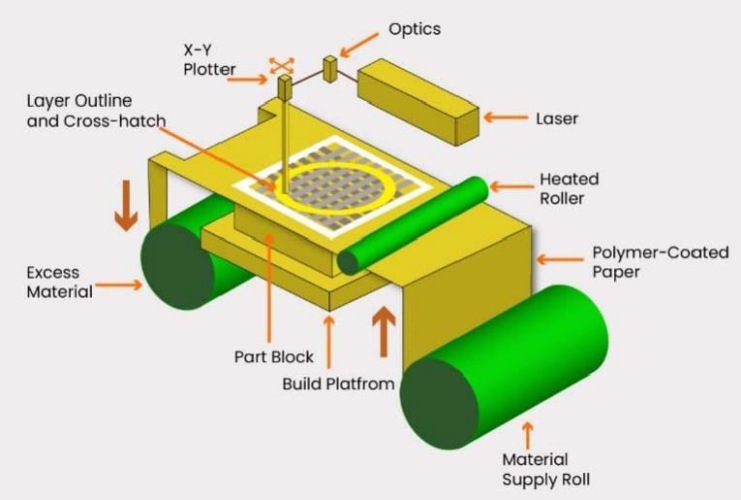

Figure IX: Schematic of sheet lamination process [9]

Depending on the way material is deposited while printing, AM technologies can also be divided into two groups: direct and indirect. In the case of direct techniques, material is precisely placed at the location of an object; this group belongs to material extrusion, material jetting, and directed energy deposition. Indirect methods, on the other hand, include binder jetting, sheet lamination, vat photopolymerization, and powder-bed fusion, whereby material is laid down over a surface and the object's cross-section is defined within it. This latter approach therefore requires excess material to be removed after printing, which also acts as structural support for subsequent layers.

Yet, most direct methods often involve supports for printing overhanging features that can be rather tedious and skill-intensive to remove after printing. On the other hand, the use of indirect procedures in dealing with closed-porosity objects often poses several drawbacks because of trapped material excess within an object. In instances involving even tiny pores or open-cell structures, it may still not be fully removable.

In the indirect methods, such as powder-bed fusion and binder-based approaches, the surface quality is degraded due to partially bonded particles. However, these indirect methods could be faster in production since an entire cross-section is formed in each

layer, enabling the simultaneous fabrication of multiple parts. In contrast, direct AM methods deposit materials one by one; hence, their production efficiency is low.

The more functional properties are expected in the AM of ceramics from design and prototyping to manufacturing, the more several technical problems, remain common in most AM technologies. Research has so far been dominated by the fabrication of porous structures such as lightweight lattices, concrete structures, tissue engineering scaffolds, filters, and catalyst carriers. Most current direct AM methods are intrinsically suitable for the manufacturing of highly meshed structures, and this allows very accurate control of pore distribution, orientation, and geometry, hardly reachable by traditional routes. In this way, AM competes less with the traditional techniques but opens new perspectives. Many of these applications allow a certain random porosity, which is often useful for functionality enhancement.

1.5 Applications of Additive Manufacturing

Additive Manufacturing has emerged in recent years as a revolutionary manufacturing technology across industries, enabling unparalleled efficiency and novelty in product design and development. For this reason, it helps reduce the product design cycle and development time considerably; hence, it is a very important enabler for manufacturers to bring new products fast into the market in a secure and controlled manner. This advantage has been particularly exploited by automated manufacturing systems.

Additive manufacturing has gained significant entry time into the construction industry for offering different solutions in the development of buildings and infrastructure. Capable of 3D printing complex architectural designs, AM enables the making of customized structures and components that were either too difficult or more costly to make with traditional methods. Large-scale AM technologies, such as concrete 3D printing, create entire sections of buildings in a shorter time with reduced waste of construction materials. AM will also continue to support sustainability through the development of more environmentally friendly materials, the recycling of construction waste, and designing optimal shapes for the use of minimal resources as shown in Figure X.

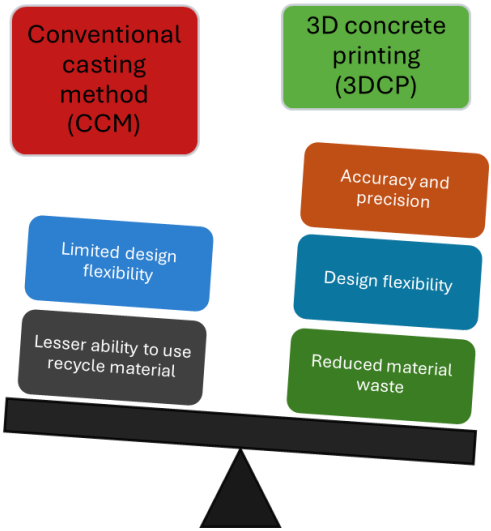

Figure X: Benefits of 3D concrete printing over conventional methods

The aerospace industry [10–13] has shown great interest in AM due to its ability to directly fabricate complex high-performance metal parts, such as titanium components, which are ideal for aircraft applications. AM techniques like Electron Beam Melting (EBM) and Selective Laser Sintering (SLS) are now widely employed in the aerospace sector to produce lightweight, precise, and durable components without the need for traditional tooling. Both the automotive and aerospace industries have one common goal: to make vehicles and aircraft lighter. In this regard, AM technologies are well suited to meet the need for lightweight yet mechanically robust parts. Examples of the adoption of AM in aerospace applications include verification of an airline electrical generator, casting patterns for impeller compressor shrouds, and making flight-certified production castings. In automotive, AM has been used successfully for applications such as prototyping complex gearbox housings in support of design verification, building cast metal engine blocks, and producing tools for rear wiper motor covers [14]. Petrovic et al. [15] presented empirical studies that compared conventional manufacturing processes, such as gravity die casting, cross drilling, electrochemical deburring, and hole blanking, with AM processes in the fabrication of

aerospace and automotive parts. These studies indicated that parts made with AM exhibited equivalent mechanical properties while using 40% less material. It also revolutionized artistic and jewellery because of its high intricacy in design. Among many techniques for AM technology, SLA developed by 3D Systems has proved efficient in creating a model of fine jewellery, based on high-resolution printing of parts. AM technologies have already shown great potential in several biomedical applications, both basic and advanced. Introducing AM to imaging technologies such as CT or MRI, for instance, will enable direct fabrication of complicated anatomical structures from scanned data. These physical models improve the understanding of complex anatomies, support meticulous preoperative planning, and allow surgeons and medical trainees to practice surgical techniques in a lifelike manner. Besides, they act as an excellent medium for the interaction between clinicians and patients.
[16–18].

1.6 Materials used in 3D printing of concrete

1.6.1 Cementitious Materials

Cement

Cement is the most common binder in concrete and mortars, traditionally manufactured by mixing with water and aggregate. Recently, several cementitious materials have been developed with the capability to create structures in a layer-by-layer fashion for 3D printing applications. Such types of materials provide the advantages of design flexibility, reduced labour costs, and pace of construction. The type of cementitious material used in 3D printing can be classified as:
Portland Cement-Based Mixes: Those are by far the most common, based on traditional Portland cement, with the addition of fine aggregates and admixtures to improve flowability and setting times. Mix design adjustments must be made to achieve the required rheological properties for extrusion and buildability.
Adaptive foam concrete (AFC) is such a versatile material, and its properties can be designed to a large degree by adjusting its mix design and density. In research work in which its hardened properties have been explored [19], a mixture of type I limestone

powder and cement gave 28-day compressive strengths of 0.1 to 0.4 MPa at a density of 180 kg/m³, and when the density was increased to 550 kg/m³, the strengths were around 2 MPa. Additional tests with the printers modified to achieve higher density showed three ranges of densities Figure XI: low-density ones (150 kg/m³ and 280 kg/m³) that were poor in strength and only suitable for insulation and filling but not for structural load. AFC, on the other hand, with a density over 1000 kg/m³, had a compressive strength of 1.9 MPa and thus was adequate to bear static loads. Interestingly, one of the foam-free mixes attained 62.1 MPa after 28 days, highlighting the trade-off between foam incorporation and mechanical performance. This sort of variability illustrates AFC's potential for application customization, where specific density and strength requirements can be engineered to meet the demands of both structural and non-structural applications.

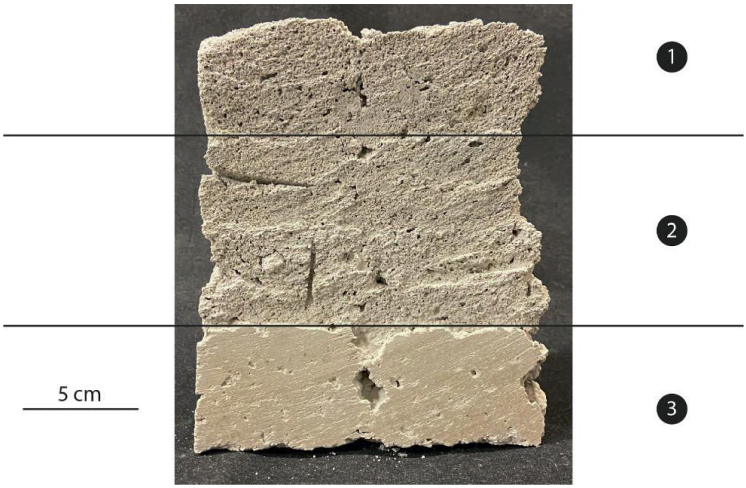

Figure XI: Specimen fabricated using adaptive foam concrete (AFC) at varying density conversion during the printing. (1) 150 kg/m3; (2) 280 kg/m3; (3) 1070 kg/m3 [19]

Geopolymer

These are ecological geopolymers, industrial byproducts used such as fly ash or slag, which get activated with alkaline solutions. In applications, it presents a lower carbon footprint and is fire resistant, finding uses in sustainable construction.

The binder jet 3D printing of non-cementitious materials is presumed to be a promising approach toward sustainable construction, provided that the powder bed formulation is precisely optimized. Using geopolymer, metakaolin was mixed with an inert aggregate; the choice of sand determines the packing density and pore structure of the bed. According to Figure XII from Odaglia et al. (2020) [20], the type of sand influences binder uptake and, consequently, the process of selective activation: jetted binder promotes local reactions in metakaolin-rich areas, forming green parts that develop early strength, while unactivated powder remains stable. This material approach not only increases the dimensional accuracy and buildability of the fabricated specimens but also contributes to environmental sustainability by allowing waste-free, integrated formwork arrangements.

Figure XII: Prined bars with different materials: Gneiss sand, Concrete sand and Brick sand (from bottom to top) [20]

Magnesium potassium phosphate cement (MKPC)

Weng et al. [21] investigated the feasibility of paste for 3D printing applications. According to their investigation, MKPC exhibited rapid setting times and acceptable mechanical properties, making it a promising candidate for 3DCP, especially in scenarios requiring quick demolding or load-bearing capabilities.

1.6.2 Aggregates and Fillers

Aggregates constitute a major determining factor in establishing the rheology, printability, and mechanical performance of the 3D-printed concrete.

Fine Aggregates: Due to the restrictions of extrusion-based printing methods, fine aggregates are very frequently utilized, such as silica sand, which provides good flow and minimizes blockages of the nozzle.

Lightweight Aggregates: The addition of lightweight aggregate materials such as expanded clay or perlite decreases the final density of the printed parts and enables specific practical uses, such as building façades and other large modular parts.

1.6.3 Admixtures and Additives

In improving fresh and hardened concrete mix properties in 3D printing,
some admixtures and additives are realized:

Superplasticizers: These will improve the flowability without adding water to the mix so that the required strength and durability can be maintained.

Viscosity-Modifying Agents: These are used to control the rheology of the mix, ensuring stability during extrusion while preventing segregation.

Accelerators and retarders can also be added depending upon the demand during printing processes and speeding up/delaying accordingly to allow an appropriate setting time.

1.6.4 Fiber Reinforced

Addition of fiber is one common approach for attempting improvement in the mechanical properties with less cracking among the 3D-printed concrete:

Steel Fibers: It improves tensile strength and toughness but has possible problems with clogging during the printing process. Steel reinforcement is crucial in concrete because it significantly enhances tensile and flexural properties by bridging cracks. However, as shown in Figure XIII, in 3D printed concrete the steel fibers are oriented entirely parallel to the fracture surface rather than being partially pulled out to bridge interlayers [22]. This results in the fibers not reinforcing the interlayer region, which

causes the flexural strength of printed specimens with fibers (PF) to be about 11% lower than that of conventionally printed concrete (CF) without fibers—highlighting that the bonding between layers depends solely on the matrix and the voids between layers, making it more vulnerable.

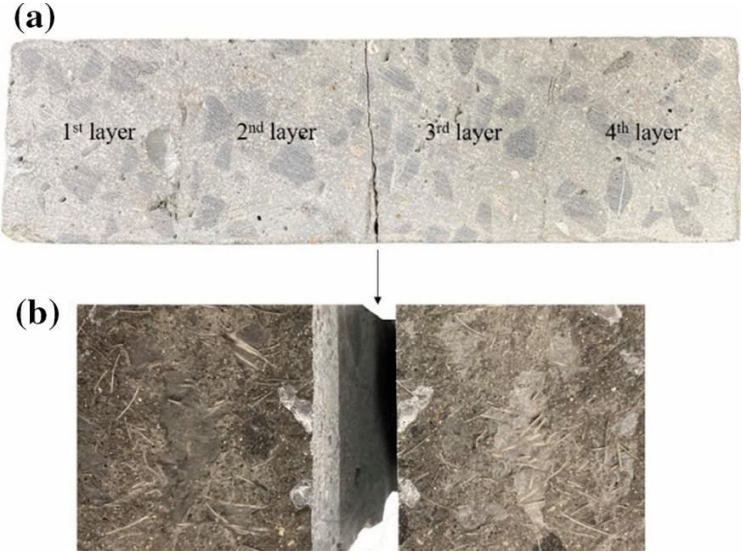

Figure XIII: Failure behaviour of the four-layer samples in the flexural test; b fracture surface [22]

Polypropylene Fibers: The utilization of polypropylene fibers in 3D printed concrete not only fulfills the structural performance criteria but also provides an economical and sustainable reinforcement solution. Polypropylene fibers are utilized because of their wide availability, low price, and high durability, which help to improve the mechanical performance of the printed structures by enhancing crack resistance and minimizing shrinkage. Their low weight and minimal density serve to enhance the workability of the fresh mix and minimize the weight of the printed structures without sacrificing structural strength. The fibers also impart enhanced chemical resistance, thereby guaranteeing long-term strength and toughness in varying environmental exposures. Through the replacement of higher-cost fibers such as carbon, aramid, or basalt, polypropylene fibers reduce the cost of 3D printed structures without a compromise in

performance and therefore represent an economic alternative to enable sustainable construction [23].

1.7 Historical developments in cement-based additive manufacturing

The concept of additive manufacturing in the construction industry originated in the late 20th century, with early research focused mainly on extrusion-based fabrication. Techniques like robocasting and contour crafting gained attraction mainly because of their extrusion properties in a controlled manner. However, these methods faced several challenges including restricted geometric freedoms and interlayer bonding issues. The introduction of binder jetting technology in the cement industry is an alternative approach to print. It was observed that cement-based materials become more popular in the binder jetting process. It is required that different mixed design procedures be optimized until they are suitable to print using BJ3DP technology. Not all types of mix designs are suitable for fabrication as the printing process is quick and requires optimized material composition for the ideal setting time, the reaction among particles and the flowability of the materials. The use of cement-based materials in the binder jetting 3D printing technology has been widely explored in the last decades because of the inherent benefits of cement such as high mechanical properties, durability and fire resistance behaviour.

Pegna's [24] research shows the use of ordinary Portland cement on the layer of silica sand to fabricate the mortar parts, but the findings were limited and don't show the mechanism of mixing and the percentage content of the mixing at different water-cement ratios in the matrix. As cement has the most prominent use in the infrastructure so more research is needed to make this technique adaptable for all composite resources and robust parts.

Different parameters influence the properties of the printed specimens. One of the key parameters is the flowability of the dry powder. This parameter is directly linked to the uniformity of the layer deposition. Poor flowability can result in uneven powder spreading, resulting in inconsistencies in the printed structure. Moreover, the interaction between the powder and the liquid binder significantly affects the properties of the printed specimen. Xia et al.[25] analyzed the impact of binder saturation level

on the printed specimen's mechanical properties and dimensional accuracy, resulting in the higher saturation level improved interaction but may lead to the dimensional distortion of the printed specimen. In addition to the binder saturation level, shell to-core ratio was also observed and the findings suggest that changing the shell-to-core ratio from 1:1 to 1:2 along with increasing the binder saturation level significantly improves the mechanical behaviour of the the printed specimens.

Figure XIV illustrates the printed process and printed specimen used for mortar materials.

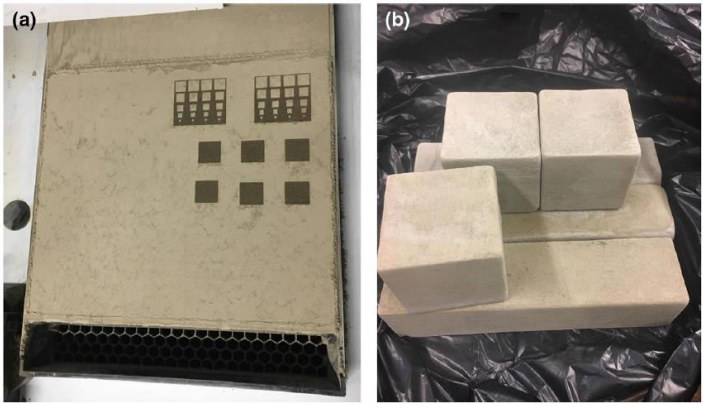

Figure XIV: (a) Printing process for cement-based mortar material (b) Prined specimens for mechanical testing [26]

An important parameter that directly affects the mechanical properties, porosity and dimensional stability of the printed specimens is the water-to-cement (w/c) ratio. Previous research by McEleney [27] et al. examined the binder spreading behaviour on the powder bed and concluded that the liquid drop penetration increases with the reduction of macro voids on the powder bed.

Another important parameter is the size of the aggregate which mainly influences the mechanical properties of the finished product. Experimental results of previous research emphasize that aggregate proportions are of vital importance in governing binder deposition during the 3D printing of coarse composite concrete powders. The single droplet tests, shown in Figure XV, illustrate an increase in the aggregate ratio

that yields horizontal binder expansion significantly less predictable; this can be explained by reduced powder bed density with higher porosity, compromising the homogeneity of binder placement.

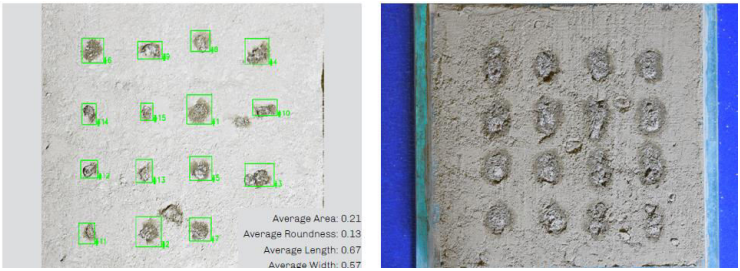

Figure XV: Single droplet printing test and shortline printing test for cement:sand: aggregate (1:1:2)[28]

The work also explains the 2 mm binder spacing with the 3.5 mm spacing as shown in Figure XVI.

Figure XVI: For a layer thickness of 5 mm and the 2 mm binder spacing on the left and 3.5 mm binder spacing on the right [28]

Magnesium potassium phosphate cement (MKPC) was used in some other research to repair concrete structures. This material has benefits for rapid setting and resistance to severe conditions. Figure XVII shows the MKPC printed specimen showing the bounded structure embedded in a loose powder bed.

Figure XVII: MKPC fabricated specimen [29]

The development of the microstructure of the printed part in dependency on binder saturation. It can be seen from Figure XVIII that a series of cross-sectional images, with the decrease of layer thickness and an optimum binder adjustment, indicate proper development of interlayer bonds and distribution of voids. This also creates more homogeneously consolidated interlayer interfaces that are reflected in better compressive and flexural strengths. It confirms again the crucial importance of printing parameters in material performances and underlines the potential in process optimization that could bridge laboratory-scale experiments up to industrial application.

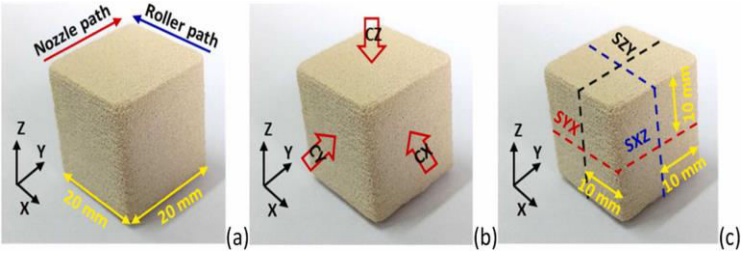

Figure XVIII: (a) Printing and loading directions of specimens (b) compressive test and (c) splitting tensile test[30]

Ingaglio et al. [31] examined the behaviour of the fine aggregates that eventually increase the density of the specimen using Calcium Sulfoaluminate (CSA), where the printed component is shown in Figure XIX.

Figure XIX: Fabricated specimens using CSA cement [31]

Powdered silica sand (300um) and calcium sulfaluminate (CSA) were used, along with humectants and water as binders. Kunchala et al. [32] observed that both density and compressive strength can be increased by using a densifier of alumina nanoparticles in the printing liquid. The compressive strength of the specimen can be enhanced up to 743% by the addition of up to 15% alumina densifier.

The flexibility of the powder-based 3D printing method is illustrated by specimen geometries shown below. The cubic samples of 20 × 20 × 20 mm were printed using a geopolymer-based powder, mixed especially for digital construction applications (Figure XX). It is a designed combination of industrial slag, anhydrous sodium metasilicate milled down to fine grains, and silica sand in such a proportion that it can make intricate geometries with finer structural details. The selection of these materials and the strict control of the parameters of printing further underline the possibilities of the method for producing complex, structurally sound components, while enhanced post-processing could yield better "green" strength.

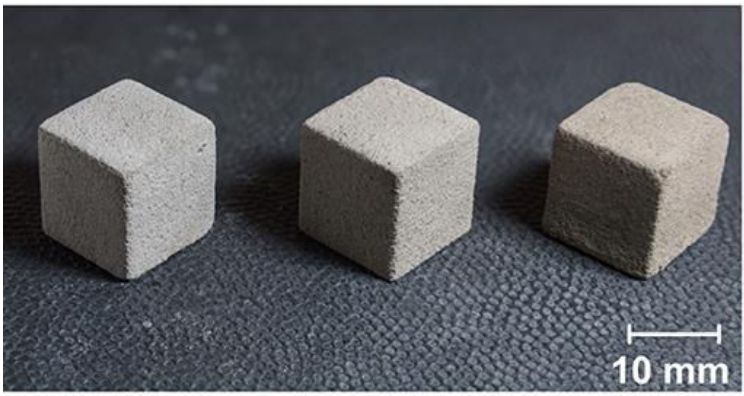

Figure XX: 3D printed structures using geopolymer-based material 20 × 20 × 20 mm cubic samples [33,34]

Optimization and choice of the raw material are key to releasing the technology's full potential. However, continued research and development in this intend to overcome existing constraints and keep new openings for innovative applications for construction and more.

Quick-setting cements are less frequently utilized in 3D printing, but they have specific benefits in cases where early stiffening is essential. Natural quick-setting cement (CNP PM NF) by Vicat was employed in this research. This is not a generic product but a highly engineered binder made by calcination of an argillaceous limestone at 1000–1200 °C to a distinct mineralogical composition. Tricalcium silicate (C_3S) and dicalcium silicate (C_2S) are the main components, with tricalcium aluminate (C_3A) and calcium ferroaluminate (C_4AF) also predominant. Finally, spurrite ($Ca_5(SiO_4)_2(CO_3)$) and calcite ($CaCO_3$) are also contained herein, and there are trace amounts of lime, magnesia, and several alkali sulfates.

Chemically, the lack of gypsum in this composition permits instant hydration of C_3A to calcium aluminate hydrates (C_3AH_6) that prompts very quick setting—typically under 1 to 20 minutes. C_3S hydration contributes to early strength by the reaction with C-S-H and calcium hydroxide (CH) formation. The moderate-temperature grinding retains reactivity phases and prevents overburning, increasing early reactivity and allowing the binder to be suitable for quick build-up of layers in AM applications. This

mineralogical constitution and reactivity make CNP PM NF different from standard Portland cement and recommend its application in experimental printing processes where immediate setting is beneficial. By contrast, the OPC hydrates slightly more slowly: its alite (C_3S) phase forms C–S–H gel gradually over days, and its belite (C_2S) phase hydrates very slowly. The portlandite ($Ca(OH)_2$) of OPC provides calcium for later growth of C–S–H.

References

1. Gibson, I.; Rosen, D.; Stucker, B. Generalized Additive Manufacturing Process Chain. *Additive Manufacturing Technologies* **2015**, 43–61, doi:10.1007/978-1-4939-2113-3_3.
2. Zhai, Y.; Lados, D.A.; Lagoy, J.L. Additive Manufacturing: Making Imagination the Major Limitation. *JOM* **2014**, *66*, 808–816, doi:10.1007/S11837-014-0886-2/TABLES/2.
3. Terminology for Additive Manufacturing - General Principles - Terminology. **2015**, doi:10.1520/ISOASTM52900-15.
4. Li, Z.; Hojati, M.; Wu, Z.; Piasente, J.; Ashrafi, N.; Duarte, J.P.; Nazarian, S.; Bilén, S.G.; Memari, A.M.; Radlińska, A. Fresh and Hardened Properties of Extrusion-Based 3D-Printed Cementitious Materials: A Review. *Sustainability 2020, Vol. 12, Page 5628* **2020**, *12*, 5628, doi:10.3390/SU12145628.
5. Otton, J.M.; Birbara, N.S.; Hussain, T.; Greil, G.; Foley, T.A.; Pather, N. 3D Printing from Cardiovascular CT: A Practical Guide and Review. *Cardiovasc Diagn Ther* **2017**, *7*, 50726–50526, doi:10.21037/CDT.2017.01.12.
6. Trombetta, R.; Inzana, J.A.; Schwarz, E.M.; Kates, S.L.; Awad, H.A. 3D Printing of Calcium Phosphate Ceramics for Bone Tissue Engineering and Drug Delivery. *Ann Biomed Eng* **2017**, *45*, 23–44, doi:10.1007/S10439-016-1678-3/TABLES/2.
7. Bevans, B.; Barrett, C.; Spears, T.; Gaikwad, A.; Riensche, A.; Smoqi, Z.; Halliday, H.; Rao, P. Heterogeneous Sensor Data Fusion for Multiscale,

Shape Agnostic Flaw Detection in Laser Powder Bed Fusion Additive Manufacturing. *Virtual Phys Prototyp* **2023**, *18*, doi:10.1080/17452759.2023.2196266.

8. Jardon, Z.; Guillaume, P.; Ertveldt, J.; Hinderdael, M.; Arroud, G. Offline Powder-Gas Nozzle Jet Characterization for Coaxial Laser-Based Directed Energy Deposition. *Procedia CIRP* **2020**, *94*, 281–287, doi:10.1016/J.PROCIR.2020.09.053.

9. Rajora, A.; Kumar, R.; Singh, R.; Sharma, S.; Kapoor, S.; Mishra, A. 3D PRINTING: A REVIEW ON THE TRANSFORMATION OF ADDITIVE MANUFACTURING. *International Journal of Applied Pharmaceutics* **2022**, *14*, 35–47, doi:10.22159/IJAP.2022V14I4.44597.

10. Campbell, I.; Bourell, D.; Gibson, I. Additive Manufacturing: Rapid Prototyping Comes of Age. *Rapid Prototyp J* **2012**, *18*, 255–258, doi:10.1108/13552541211231563/FULL/XML.

11. Joshi, S.C.; Sheikh, A.A. 3D Printing in Aerospace and Its Long-Term Sustainability. *Virtual Phys Prototyp* **2015**, *10*, 175–185, doi:10.1080/17452759.2015.1111519.

12. Granda, J.J.; Montgomery, R.C. Automated Modeling and Simulation Using the Bond Graph Method for the Aerospace Industry. *AIAA Modeling and Simulation Technologies Conference and Exhibit* **2003**, 1–11, doi:10.2514/6.2003-5527.

13. Nobrega, B.N.; Ristow, W.; Machado, R. MIM Processing and Plasma Sintering of Nickel Base Superalloys for Aerospace and Automotive

Applications. *Powder Metallurgy* **2008**, *51*, 107–110, doi:10.1179/174329008X286659.

14. Rapid Prototyping: Principles And Applications (2nd Edition) (With Companion ... - Chee Kai Chua, Kah Fai Leong, Chu Sing Lim - Google Books Available online: https://books.google.it/books/about/Rapid_Prototyping_Principles_And_Applica.html?id=mGRIDQAAQBAJ&redir_esc=y (accessed on 14 December 2024).
15. Petrovic, V.; Vicente Haro Gonzalez, J.; Jordá Ferrando, O.; Delgado Gordillo, J.; Ramon Blasco Puchades, J.; Portoles Grinan, L. Additive Layered Manufacturing: Sectors of Industrial Application Shown through Case Studies. *Int J Prod Res* **2011**, *49*, 1061–1079, doi:10.1080/00207540903479786.
16. Melchels, F.P.W.; Feijen, J.; Grijpma, D.W. A Review on Stereolithography and Its Applications in Biomedical Engineering. *Biomaterials* **2010**, *31*, 6121–6130, doi:10.1016/j.biomaterials.2010.04.050.
17. Liu, Q.; Leu, M.C.; Schmitt, S.M. Rapid Prototyping in Dentistry: Technology and Application. *International Journal of Advanced Manufacturing Technology* **2006**, *29*, 317–335, doi:10.1007/S00170-005-2523-2/METRICS.
18. Dhakshyani, R.; Nukman, Y.; Abu Osman, N.; Vijay, C. Preliminary Report: Rapid Prototyping Models for Dysplastic Hip Surgery. *Open Medicine* **2011**, *6*, 266–270, doi:10.2478/s11536-011-0012-6.

19. Schmid, R.; Hansemann, G.; Autischer, M.; Juhart, J. Adaptive Foam Concrete in Digital Fabrication. *RILEM Bookseries* **2022**, *37*, 22–28, doi:10.1007/978-3-031-06116-5_4/FIGURES/6.

20. Odaglia, P.; Voney, V.; Dillenburger, B.; Habert, G. Advances in Binder-Jet 3D Printing of Non-Cementitious Materials. *RILEM Bookseries* **2020**, *28*, 103–112, doi:10.1007/978-3-030-49916-7_11/FIGURES/7.

21. Weng, Y.; Ruan, S.; Li, M.; Mo, L.; Unluer, C.; Tan, M.J.; Qian, S. Feasibility Study on Sustainable Magnesium Potassium Phosphate Cement Paste for 3D Printing. *Constr Build Mater* **2019**, *221*, 595–603, doi:10.1016/j.conbuildmat.2019.05.053.

22. Chen, Y.; Zhang, Y.; Pang, B.; Wang, D.; Liu, Z.; Liu, G. Steel Fiber Orientational Distribution and Effects on 3D Printed Concrete with Coarse Aggregate. *Materials and Structures/Materiaux et Constructions* **2022**, *55*, 1–19, doi:10.1617/S11527-022-01943-7/FIGURES/13.

23. Ungureanu, D.; Onuțu, C.; Țăranu, N.; Vornicu, N.; Zghibarcea, Ștefan V.; Ghiga, D.A.; Spiridon, I.A. Microstructure and Mechanical Properties of Cost-Efficient 3D Printed Concrete Reinforced with Polypropylene Fibers. *Buildings 2023, Vol. 13, Page 2813* **2023**, *13*, 2813, doi:10.3390/BUILDINGS13112813.

24. Pegna, J. Exploratory Investigation of Solid Freeform Construction. *Autom Constr* **1997**, *5*, 427–437, doi:10.1016/S0926-5805(96)00166-5.

25. Xia, M.; Nematollahi, B.; Sanjayan, J. Compressive Strength and Dimensional Accuracy of Portland Cement Mortar Made Using Powder-

Based 3D Printing for Construction Applications. *RILEM Bookseries* **2019**, *19*, 245–254, doi:10.1007/978-3-319-99519-9_23.

26. Shakor, P.; Chu, S.H.; Puzatova, A.; Dini, E. Review of Binder Jetting 3D Printing in the Construction Industry. *Progress in Additive Manufacturing* 2022.

27. McEleney, P.; Walker, G.; Orr, J.; Dunne, N.J. Investigations on Drop Penetration and Wetting Characteristics of Powder-Liquid Systems in Relation to the Mixing of Acrylic Bone Cement. *International Journal of Nano and Biomaterials* **2010**, *3*, 20–35, doi:10.1504/IJNBM.2010.036105.

28. Towards Adaptive Additive Manufacturing: Image-Based Monitoring for Binder Jet 3D Printing of Coarse Composite Concrete Powders Available online: https://www.researchgate.net/publication/377977642_Towards_Adaptive_Additive_Manufacturing_Image-based_Monitoring_for_Binder_Jet_3D_Printing_of_Coarse_Composite_Concrete_Powders (accessed on 6 February 2025).

29. Fu, Y.; Cao, X.A.; Li, Z. Printability of Magnesium Potassium Phosphate Cement with Different Mixing Proportion for Repairing Concrete Structures in Severe Environment. *Key Eng Mater* **2016**, *711*, 989–995, doi:10.4028/WWW.SCIENTIFIC.NET/KEM.711.989.

30. Ma, G.; Hu, T.; Li, Z. Binder Jetting 3D Printing Rock Analogs Using Magnesium Phosphate Cement. *Constr Build Mater* **2024**, *420*, 135620, doi:10.1016/J.CONBUILDMAT.2024.135620.

31. Ingaglio, J.; Fox, J.; Naito, C.J.; Bocchini, P. Material Characteristics of Binder Jet 3D Printed Hydrated CSA Cement with the Addition of Fine Aggregates. *Constr Build Mater* **2019**, *206*, 494–503, doi:10.1016/j.conbuildmat.2019.02.065.

32. Kunchala, P.; Kappagantula, K. 3D Printing High Density Ceramics Using Binder Jetting with Nanoparticle Densifiers. *Mater Des* **2018**, *155*, 443–450, doi:10.1016/J.MATDES.2018.06.009.

33. Xia, M.; Sanjayan, J. Method of Formulating Geopolymer for 3D Printing for Construction Applications. *Mater Des* **2016**, *110*, 382–390, doi:10.1016/J.MATDES.2016.07.136.

34. Nematollahi, B.; Xia, M.; Sanjayan, J. Post-Processing Methods to Improve Strength of Particle-Bed 3d Printed Geopolymer for Digital Construction Applications. *Front Mater* **2019**, *6*, 452804, doi:10.3389/FMATS.2019.00160/BIBTEX.

Binder Jetting and Schematic of customized printer

2.1 Binder jetting

Binder Jetting 3D printing technique (BJ3DP) is a technology developed at Massachusetts Institute of Technology (MIT). This technology is useful for developing solid printed specimens. The steps involved in this process [1] are shown in Figure I

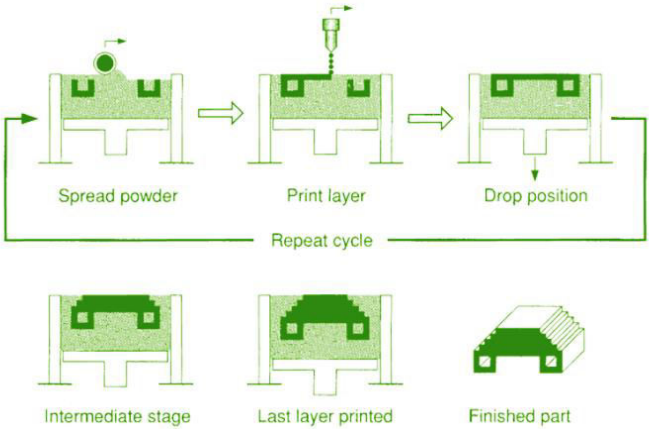

Figure I: Steps involved in BJ3DP process [1]

Following are some important steps in binder jetting

2.1.1 Spreading powder and compaction

The first step in binder jetting 3D printing is the spreading of dry powder. The hopper is mainly used to deposit the layers of the powder of required thicknesses, using a doctor blade or roller or in some cases both can be integrated into one system for

feeding and spreading (Figure II). However, for the efficient printing of the multi-material, the use of multi hopper with different materials is often recommended.

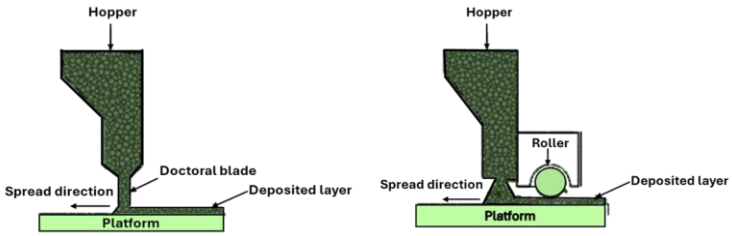

Figure II: Roller and doctoral blade-based powder delivery system

This step is linked to the packing density of the particle bed. The compaction is highly relevant to the mechanical properties of the printed specimens. Moreover, this step is quite relevant for the adjustment of the defined water-cement ratio (w/c). The required water-cement ratio can be achieved by adjusting the travel speed of the nozzle or the flow rate of the liquid. The spreading powder and compaction system used in our experiments is composed of a doctoral blade arrangement (Figure III).

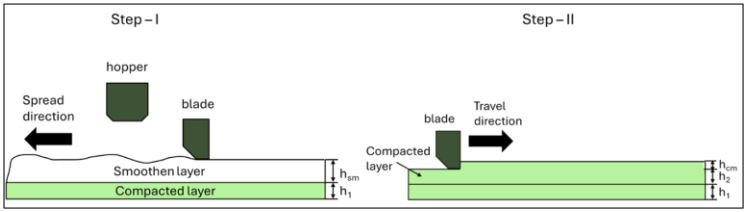

Figure III: Schematic of powder spreading and its compaction

The process of spreading the dry powder and its compaction follows the following equations:

$$h_{sm} = h_i + h_{cm}$$

$$h_i = h_{sm} - h_{cm}$$

As the blade moves in the x to x' direction, it applies force on the powder layer being spread. If the height of the smoothened layer hsm were set equal to the desired layer height hi from the very beginning, there is a chance that the blade might be over-forcing and thus damaging the underlying previously printed layer, and the compacting impact is not too prominent. To alleviate this, the smoothened layer height hsm is set to a value larger, equal to hcm, than the target layer height hi to act as a buffer. When the blade returns from x' back to x, the excess powder is skimmed off, compacting the layer to hi with controlled shear force. This acts as a compacting force less than the threshold to damage the underlying printed layer, hence ensuring integrity at the desired layer thickness.

2.1.2 Binder drops formation

A liquid binder is spread on the powder bed in either the drop-on-demand (DoD) mode or continuous stream mode. In DoD mode, individual droplets are produced directly from the nozzle allowing the liquid binder to be expelled (Figure IV). To regulate the DoD mode, the necessary pressure pulses are produced at the specific interval by either using piezoelectric, thermal, electrostatic or other actuators. However, in the continuous mode, a steady pressure is directed to the liquid tank, causing the pressurized supply of the liquid solution to be expelled from the nozzle. Besides these two modes, other technologies are experimentally tested but do not get too much interest from the industry including liquid spark jetting, ultrasonic droplet generators and electrohydrodynamic inkjet [2]. Although the DoD technique was used in this experiment, its schematic is shown here.

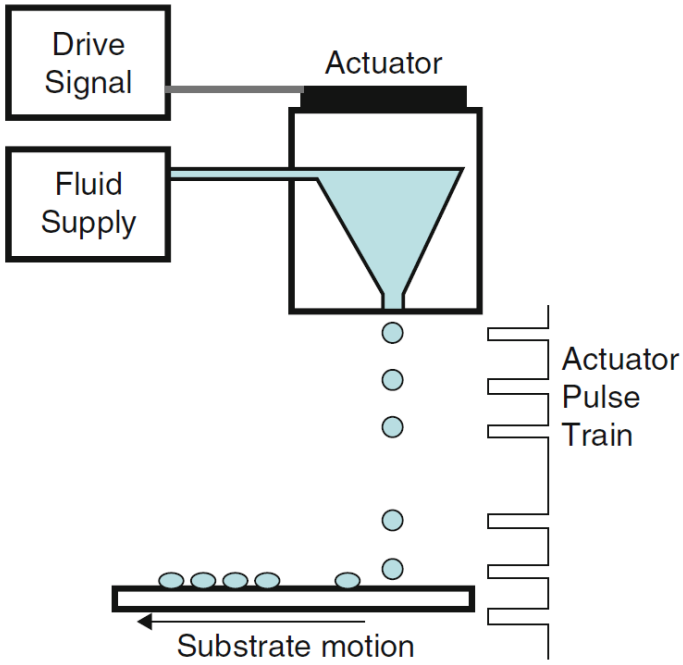

Figure IV: Schematic of drop-on-demand printing system [2]

2.2 Customized 3D printing system

An electrically powered platform is a CNC Z S-1000 T computer numerical control machine (CNC) controlled by the Nanotec NEMA23 stepper motor which moves the head of the machine along three axes x, y and z. This way the head of a machine has linear slide guides which restrict its movement. In Figure 2.5, the hopper is used for the supply of dry cement-based materials to spread uniformly on the powder bed. The machine is operated using USB-based software WIN PC NC that is connected to the device to work with NC-based files. The machine description can be illustrated using the following schematic diagram as shown in Figure V.

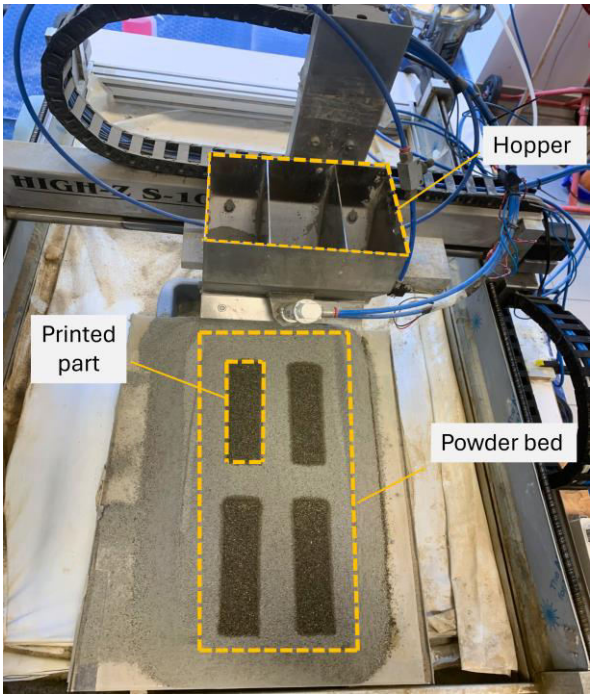

Figure V: Customized 3D printer

Hopper is mainly composed of three chambers to spread powder uniformly on the powder bed; however, the dry powder can be filled in any of them in case of a small printing area. The blended powder is stored in a hopper bin which has a lid with a pneumatic size controller. A powdery mixture stocked in a hopper bin is scattered above the plane of the print platform (for example, in positive x-direction). A pneumatic cylinder controls the lid opening of the hopper. In those locations where powder feedstock is necessary, the controller sends commands to an electro-pneumatic valve (normal close) turning on and off a vacuum pump that opens the lid.

Zero point is the reference location of coordinates in the Isometric coordinates in the working file. It is the position with a particular x and y-axis of the NC file to a particular point — say, bottom-left corner. All avoid places where the measurement of processing distances is made from here. We can also manually set the zero point as shown in

Figure VI. This involves jogging to the desired point and making it a reference zero. The positions of the axes can also be saved individually.

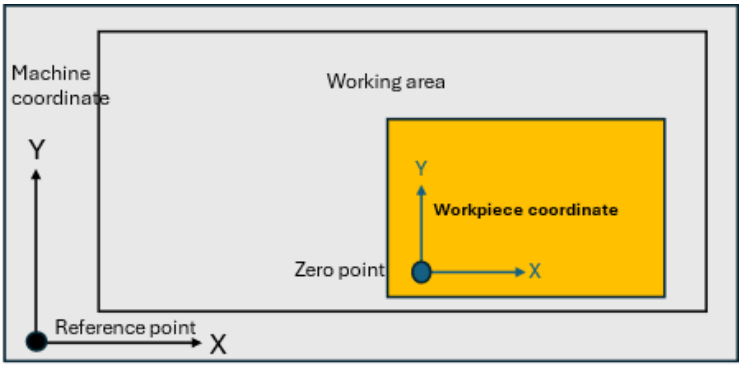

Figure VI: Working area of the machine

This CNC machine served as a 3D printer using the following improvements:

2.2.1 Binder dispensing unit

The flow rate of the binder is an important parameter that needs to be optimised before printing. This flow rate decides the amount of liquid binder required for each layer. In the experimental work, the binder flow rate was a function of liquid pressure and frequency remained constant. The dispensing unit is composed of a galvanized pressure vessel from Binks Company. These galvanized pressure tanks are primarily used for non-corrosive materials. The Binks Model II can maintain the maximum working pressure of 110 PSI where both the tank and the lid are electro-polished after constructing from heavy gauge 304 stainless steel (Figure VII).

Figure VII: Binder dispensing chamber

A manual pressure controller from Binks model HAR-511 was used to regulate the industrial air supply into the vessel as shown in Figure VIII.

HAR-511-B

	DESCRIPTION	QTY.
1	SCREW, #10-32X9/16 FILLISTER HD.	6
2	COVER	1
3	SPRING BUTTON	1
4	DIAPHRAGM SPRING	1
5	BODY	1
6	PIPE PLUG, 1/4" NPT(M)	1
7	BOTTOM PLUG	1
8	DIAPHRAGM ASSY.	1
9	O-RING	1
10	VALVE	1
11	O-RING	1
12	SPRING	1
13	O-RING	1

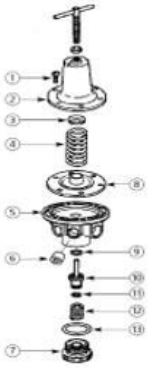

Figure VIII: HAR-511 Parts

The output of the fluidized pressure tank relates to a pipe containing the pressurized supply of liquid binder, which is then connected to the filter to prevent the unnecessary particles in the liquid binder from passing through it. This filter mainly controls the unusual clogging of the nozzle by stopping the impurities before reaching the solenoid valve. The SG111 series filter housings are used in 1/8" and 1/4" line sizes at low

pressures. The 316L stainless steel construction housing either a stainless steel or Pyrex glass bowl, the latter having a protective bowl guard. Standard SG111 housings feature NPT ports with Viton seals as shown in Figure IX. These housings are welded-free, which complies with NACE MR-01-75 standards and the SEP requirements of PED 2014/68/EU.

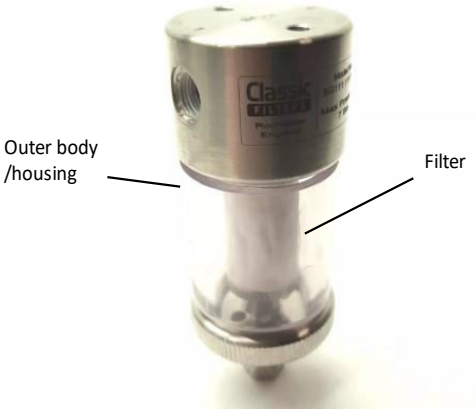

Figure IX: SG111-111 filter

2.2.2 Valve

The solenoid valve used in this study was from Staiger company, a 2/2-way generally closed (NC) to perform efficient and stable control in the printing method. With a nominal size of 0.5 mm and an outer diameter of 7 mm, it provides fast switching times required for correct substantial deposition. It operates in the pressure range of 0 - 8 bar and the Kv value <0.007 m^3 / h, providing optimal flow regulation. The lightweight valve-3 grams, of quality material, is compatible with neutral and mildly aggressive liquids, gases, and vapours. It works at a nominal voltage of 12 V DC, which is energy-efficient for long periods. The valve is attached to a manifold that enables the distribution of the material to the nozzle, with precision and consistency in extrusion important for high-quality printed components. The Staiger valve specifications are shown in Figure X.

Function	2/2 NC valve
Media	Air and inert gases, others upon request
Pneum. connection	Cartridge
Weight	4 g
IP protection class	IP65
Rated power	1 W
Electrical connection	Flying leads
Connection length	80 mm
KV value	0.12 l/min
Min. operating pressure	0 bar(g)
Max. operating pressure	8 bar(g)

Figure X: Staiger valve specifications

2.2.3 Manifold

The Lee Company-based nozzles were used to dispense the liquid binder on the powder bed. However, the nozzle is operated using a valve of 7mm from Staiger, a German company. Both Lee Co nozzle with a jewelled orifice of 1.19 mm and Staiger valve are connected using a manifold. This manifold geometry is shown in Figure XI

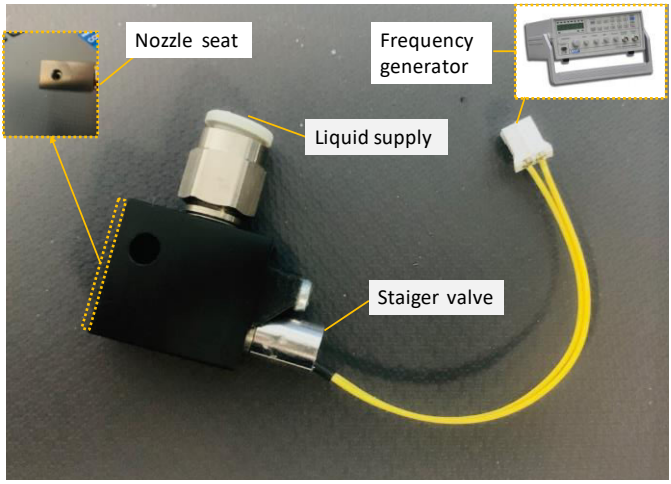

Figure XI: Mounting block or manifold for the Lee nozzle - Staiger valve arrangments

The engineering drawing shown in Figure XII is the indication of the Lee Staiger manifold that is connecting the spider valve with the nozzle.

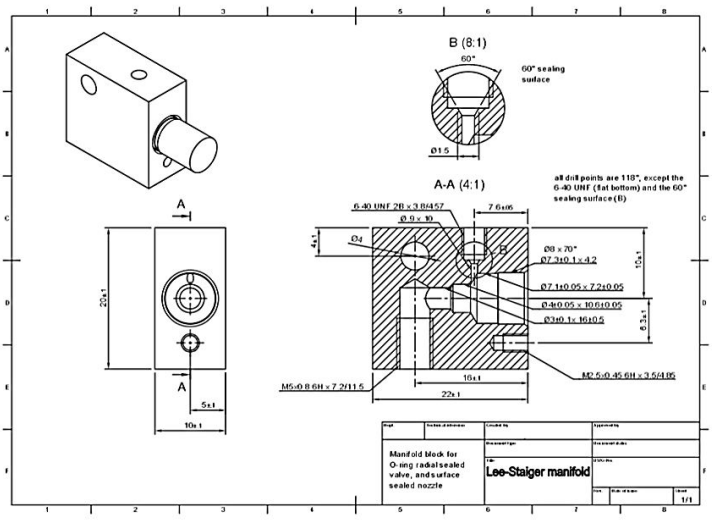

Figure XII: Engineering drawing for the manifold

2.2.4 Nozzle

The precise nozzle, from Lee Co. (Westbrook, CT, USA), with an inner diameter of 0.19 mm was utilized for the drop-on-demand dispensing of the water during the 3d printing process as shown in Figure XIII. The nozzle was integrated with the staiger valve using manifold as shown in Figure XI to ensure controlled and accurate binder deposition. The precision valve maintains the pressure to the required binder flow and the whole setup enables precise droplet formation that is essential for the uniform distribution of the binder.

Figure XIII: Nozzle used for printing

References

1. Jee, H.J.; Sachs, E. A Visual Simulation Technique for 3D Printing. *Advances in Engineering Software* **2000**, *31*, 97–106, doi:10.1016/S0965-9978(99)00045-9.
2. Gibson, I.; Rosen, D.; Stucker, B. Additive Manufacturing Technologies: 3D Printing, Rapid Prototyping, and Direct Digital Manufacturing, Second Edition. *Additive Manufacturing Technologies: 3D Printing, Rapid Prototyping, and Direct Digital Manufacturing, Second Edition* **2015**, 1–498, doi:10.1007/978-1-4939-2113-3/COVER.

Effect of water-to-quick setting cement ratio and aggregate size on mechanical properties and dimensional accuracy of binder jetting 3D-printed bodies

"Effect of water-to-quick setting cement ratio and aggregate size on mechanical properties and dimensional accuracy of binder jetting 3D-printed bodies"

OPEN CERAMICS, Elsevier

Mursaleen Shahid, Vincenzo M. Sglavo

Published – 13 November 2024

3.1 Abstract

Quick setting cement-based materials were produced in the present work using the binder jetting 3D printing (BJ3DP) technique with the aim at investigating how processing parameters like water-to-cement ratio and aggregate size affect the final properties of the products. Commercially available quick-setting cement and siliceous sand were utilized. Dimensional accuracy, compressive and flexural strength were measured for variable processing conditions and their individual effect was analysed. The results showed that the properties of printed parts are significantly influenced by the considered processing variables and, in particular, a larger water-to-cement ratio has a beneficial effect on the mechanical performances, the improvement being higher when coarser siliceous sand is used. It was also shown that the employment of finer sand results in more limited dimensional accuracy.

3.2 Introduction

The processing of cement-based materials using additive manufacturing (AM) has attracted a lot of attention from the building industry [1,2]. This shift opens a new world of possibilities, as additive manufacturing techniques promise to streamline construction processes and overcome the limitations of traditional methods. In recent years, robocasting and binder jetting 3D printing (BJ3DP) have shown themselves to be competitive substitutes for the production of cement-based materials [3,4]. Robocasting is an extrusion-based additive manufacturing technique where the concrete paste is extruded using a gantry, crane or robotic arm mechanism [5–7]. BJ3DP technique includes the layering of powder or aggregate and selective deposition of a liquid binder [8] to consolidate the desired shape layer by layer [9–12]. After hardening, the unbonded powder is methodically removed, paving the way for separate post-processing techniques aiming at achieving the desired levels of strength and durability [13–17]. An early investigation of this method was carried out by Zhou et al.[18], who studied the use of calcium sulphate hemihydrate (CaSO4.0.5H2O) in 3D printing. The potential of binder jetting technology to create high-quality parts at a

lower cost and faster rate compared to conventional manufacturing procedures has attracted a lot of interest in recent years [19].

Cement-based materials have been used in BJ3DP because of their unique properties such as high compressive strength, durability and fire resistance [20,21]. They are mainly composed of cement, aggregates and water, although their properties can be enhanced by using additives such as plasticizers, retarders and accelerators [22]. The use of cement-based materials through the BJ3DP technology offers many advantages such as increased design freedom, reduced material waste and improved sustainability [23]. Additionally, the technology makes it possible to create intricate shapes and structures that would be challenging to obtain with traditional manufacturing methods. However, this integration has forced the creation of unique mix-design protocols that are tailored to the requirements of 3D printing. It is important to remember that not all material compositions work well with the complex nature of 3D printing. Researchers have conducted significant investigations on various types [22,24–27] and amounts of cement and sand combinations [12,27–30], mostly utilizing commercially available ordinary Portland cement with sand [31]. In a previous study by Pegna [32], the use of ordinary Portland cement combined with a silica sand layer was studied for the 3D printing of mortar components. In earlier researches, specific compositions and methods used for mixing, especially with reference to the water-to-cement ratio, have not been thoroughly explained.

BJ3DP of cement-based materials is primarily influenced by the inert powder size, morphology and binder content. Several studies have been carried out and have investigated the effect of such printing parameters [14,22,33,34]. Among the variables, the characteristics of the binder flow are essential for getting the desired printing results. Xia et al. [35] analysed the effects of binder saturation level on dimensional accuracy and compressive strength. In such work, the effects of various printing parameters, such as shell-to-core ratio and binder saturation level on the dimensional correctness and compressive strength of the specimens were examined. The findings show that changing the shell/core ratio from 1:1 to 1:2 and increasing the binder saturation level significantly boosts the compressive strength. Lowke et al. [33,36] also explored the effect of the binder content using an aqueous solution on a fine cement-aggregate composite with particles smaller than 0.45 mm while employing the

selective cement activation technique. Methylcellulose thickening agent was also considered in the composition to improve the printing accuracy. An increase of compressive and flexural strength was observed to be due to wider water distribution within the layers. The study of McEleney et al. [37] also investigated the binder spreading behaviour onto the powder and the powder-binder wettability. They concluded that drop penetration increases with a reduction in macro-voids on the powder beds.

It is significant to note that spherical and coarse powders show variation in spread among adjacent particles [38]. The flowability of the powder, which must be considered and maintained uniformly throughout the process, is another important parameter. Powders with higher flowability improve the resolution of the printed specimen and the powder with lower flowability has the worst impact on the resolution of the printed specimen [39]. The angle of repose, the Hausner ratio, the flow via an orifice, the Carr's compressibility index, the Shear cell method and the Cohesion index are the most used approaches to quantify the flowability of powders[40–43].

In the exploration of aggregate size's impact, Ling et al. [44] performed an insightful study on the influence of varying sand sizes on the mechanical performance of cement-based composites enhanced with polyvinyl alcohol fibre (PVA) and nano-SiO2 (NS). They concluded that finer sand sizes lead to reduced workability and mechanical strength. However, this effect was limited to sand particles below 380 μm.

In the context of BJ3DP, the selection of aggregates must be correlated with the flowability and thickness of the printed layers [45]. In a noteworthy work, Fan et al. [46] processed carbon powder particles with diameters up to 105 μm. Their method entailed using a furfuryl resin with an acetone base as a binder. The analysis showed that the printed structures' mechanical characteristics, before the sintering stage, reached a maximum value of 5 MPa. Chun et al. [47] found that larger silica sand grain sizes improved the penetration resolution and green body strength, particularly for 70 μm particle-sized sand. Pierre et al. [34] highlighted that to achieve optimal cohesion and high compressive strength, complete filling of the sand layer's thickness with cement paste was required. Pu et al. [48]used Burger`s model to simulate the rheological properties of OPC (Ordinary Portland Cement) paste and they discovered that yield stress is a function of particle size. For cement-based materials, significant

consideration must be paid to aspects like powder size to get the appropriate printing results. Joseph et al. [43] examined a dry cementitious mix consisting of round-grain fine aggregates and calcium sulfoaluminate (CSA) cement. The results indicate that the addition of fine aggregates to CSA cement allowed the objects with rapid production capability and compatibility with conventional construction materials. Zhou et al. [47] focused on the surface homogeneity and roughness of both coarse and fine powders. They discovered that fine powder has a higher level of roughness and coarse powder has a higher level of surface uniformity.

In spite of the numerous works on BJ3DP applied to cement-based materials, a gap remains in exploring the influence of water-cement ratios on coarse and fine aggregate size and their significant impact on the mechanical properties and dimensional accuracy of 3D-printed concrete structures without additional viscosity modifying agents or thickening agents [36]. In addition, the use of materials such as quick-setting cement in the context of 3D printing, which could allow faster production systems, has not been extensively investigated.

The present study aims therefore at investigating the effects of the water-cement ratio considering two different aggregate sizes on the mechanical properties and dimensional accuracy of 3D-printed specimens using quick-setting cement.

3.3 Experimental Procedure

A customized 3D printer was used in the present work where a single nozzle by Lee Co, USA was employed to spread the binder in drop on demand manner with the help of a Staiger valve. The process starts with the creation of CAD geometry using 3D modelling software and then slicing the model into a G-code to make it readable for 3D printing [49]. The layer thickness and distance between the printing head and the powder bed were kept at 2 mm and 10 mm, respectively [31]. Binder flow and water-to-cement ratio (w/c) were controlled by varying the travel speed of the printhead between 7200 mm/min and 13000 mm/min and altering the water pressure in the 0.1 – 0.8 bar range [36].

Two different grain sizes of quartzite sand, namely 0.1 – 0.4 mm and 0.4 – 1.2 mm, were meticulously chosen for producing two different mixtures, called Mix-I and Mix-II

for fine and coarse aggregates respectively. For the former, the finest sand was homogeneously mixed with commercially available quick-setting cement from Vicat in a proportion of 1:3 by weight. The 0.43 – 1.18 mm sand was combined with the quick-setting cement in the same weight ratio to produce the second one. The particle size distribution is shown in Figure I.

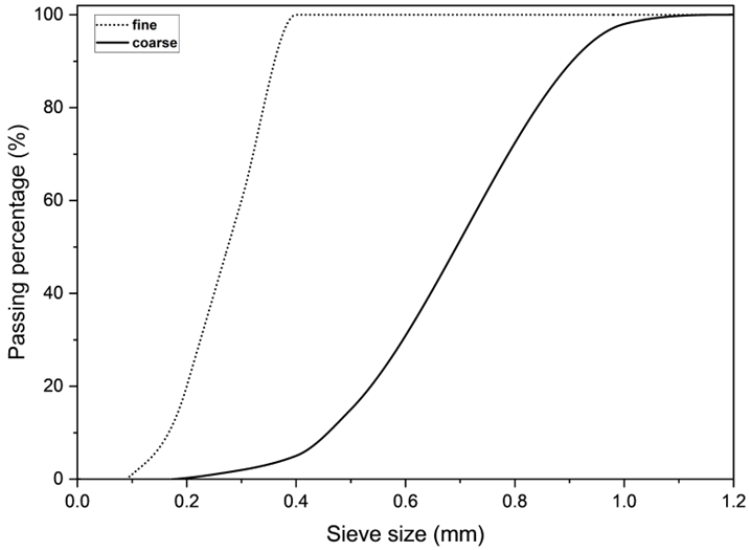

Figure I: Particle size distribution of the aggregates used in the present work

The quick-setting cement used in this study contains primarily a mixture of tricalcium silicate, dicalcium silicate, tricalcium aluminate and calcium ferroaluminate obtained by firing argillaceous limestone at 1000–1200°C, along with calcite, spurrite, and minor proportions of lime, magnesia, sodium sulphate and potassium, with traces of other elements.

Both Mix-I and Mix-II were thoroughly and separately blended for 30 min to ensure the homogeneity of the powder mixture.

The blended powders' flowability was determined using the Hausner ratio and Carr's index [12]. These parameters were calculated according to the tap volume Vt and the loose bulk volume Vb of the powder as:

$$\text{Hausner ratio} = \frac{Vb}{Vt} \qquad \text{(Eq. 1)}$$

$$\text{Carr`s Index} = \frac{(Vb - Vt)}{Vb} \times 100 \qquad \text{(Eq. 2)}$$

A graduated cylinder, as per norm ASTM D7481-18, was used to measure the loose bulk volume of the mixtures. A tap density tester was used to determine the tap volume according to the same norm [50].

A schematic of the 3D printing process is shown in Figure II: the dry powder mixture is spread from the hopper bin over the build platform and then quickly flattened with a wiper blade. Using a single nozzle with an internal diameter of 0.19 mm, deionized water [12] was sprayed onto the powder bed from a pressurized vessel. Prismatic CAD models with dimensions 160 mm x 40 mm x 40 mm were printed as per norm EN 196-1[51] to measure the flexural strength; 40 mm edge cubes were printed for compressive strength testing (Figure III). After printing, the specimens were left in the powder bed for one day to undergo controlled curing. They were then removed from the powder bed and the excess powder was removed from the surface of the printed specimens by de-powdering: a fine bristled brush was used to manually remove the loose material from the surface of the samples and partially filled cavities on the outer geometry. This gentle manual removal of excess powder needs extra care as excess force might damage the printed layers.

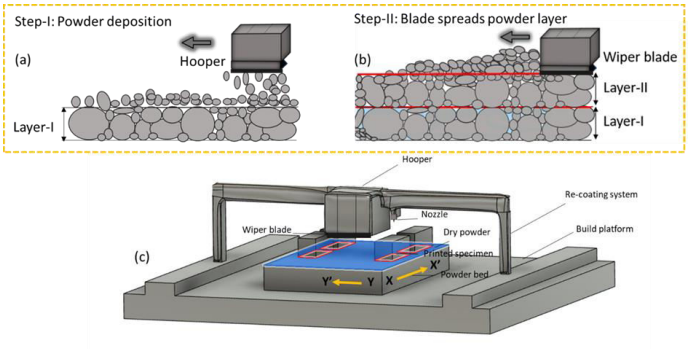

Figure II: (a, b) Powder deposition and spreading (c) Schematic of customized 3D printer.

The precision of the printed specimens establishes the level of conformity between the printed and the design dimensions. Vernier caliper was used to measure the dimensions of the printed specimens. Based on these measurements, the dimensional deviation ratio (DDR) and the X and Y printing precision in terms of xy-axis print precision were calculated to make assessments of printing accuracy [28,40]. By comparing the measured dimensions of the 3D-printed specimens to the CAD dimensions, the dimensional deviation ratio (DDR) was determined as:

$$DDR\ (\%) = \frac{L_P - L_{CAD}}{L_{CAD}} \times 100 \qquad \text{(Eq. 3)}$$

where Lp and LCAD are the printed and initial dimensions defined in the CAD model of the specimen, respectively. The proportional variation between the measured dimensional values of the 3D-printed specimens and the desired dimensions was obtained also in terms of XY-axis printing precision:

$$XY - axis\ printing\ precision\ (\%) = \frac{A_p - A_o}{A_o} \times 100 \qquad \text{(Eq. 4)}$$

where Ap and Ao are the real printed area after de-powdering and the area of the 3D CAD file, respectively. Thirty measurements across the final layer were carried out to estimate accuracy. In contrast, the dimensional deviation ratio defines the linear discrepancies between dimensions in print and the nominal dimensions. Though complex geometries may not be captured with high precision by caliper, careful measurement at several touchpoints was done to reduce inaccuracy.

During post-processing, 80-grit sandpaper was used to refine the specimen into the required dimensions for mechanical testing. The specimens were set to be cured in air and were placed under a controlled hood for periods ranging from 1 to 28 days until mechanical testing was carried out.

An Anton Paar pycnometer (Ultrapyc 5000 series) was used to measure the true density of the printed samples after 7 days. Apparent and bulk density were determined as per the norm ASTM C-642 [52] and ASTM C-20 for porosity.

Mechanical tests were carried out on a universal mechanical testing machine (model 810, MTS Systems, Minneapolis, MN, USA) to determine flexural and compressive strength. The former was measured by a three-point bending test as:

$$\sigma_f = \frac{3Fl}{2bd^2} \qquad \text{(Eq. 5)}$$

where F, l, b and d are the maximum load, length, width and thickness of the specimen, respectively. A constant loading rate (50 ± 10 N/s) was used for the test.

For the compression test, the loading rate was kept at 2400 N/s and the strength σ_c was determined as the maximum load applied over the nominal cross-section of the sample (40 mm x 40 mm).

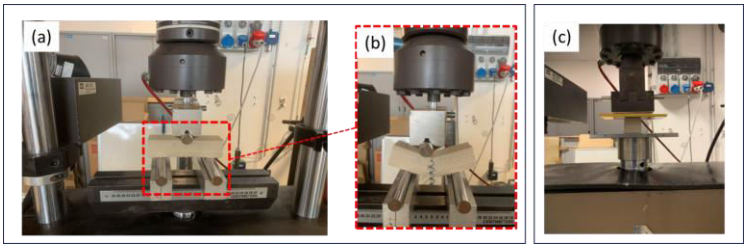

Figure III: (a) Flexural strength testing setup; (b) Fractured specimen after 3-point bending testing; (c) Compressive strength testing setup

3.4 Results and Discussions

The flowability data reveal interesting details about the two mixtures behaviour. The excellent flow characteristics of both Mix-I and Mix-II are demonstrated by their Hausner ratio equal to 0.86 and 0.9, respectively. Furthermore, their Carr's index is equal to 15.5 for Mix-I and 11.1 for Mix-II confirming that they are appropriate for the

experiment. Notably, Mix-I shows somewhat better flow properties than Mix-II, thus highlighting its potential benefit in particular applications needing ideal flowability [18]. Figure IV shows the measured true, bulk, apparent density and porosity of 3D printed specimens. The results show that the density slightly increases moving from Mix-I to Mix-II. This can be very likely correlated to the different sizes of the sand used in the two mixtures which makes the material produced with the coarser one more compact. The increased density observed in Mix-II might be mainly ascribed to the presence of coarser aggregate sizes in comparison to Mix-I. The interplay of particle size, shape, and packing properties has a considerable impact on overall density. The larger sand particles in Mix-II most likely increased interparticle interactions and reduced particle segregation during a step of powder deposition and spreading, resulting in a denser concrete matrix. The effect of the water-to-cement ratio on density is very limited, the values being just slightly higher at larger w/c. In this case, the presence of more water allows more intense hardening reactions for the cement among the siliceous sand particles thus contributing to a more compact structure. By increasing the w/c ratio, the true density of 3D-printed parts increases as well. This may be attributed to the fact that at higher w/c ratios hydration increases and this could eventually lead to a denser microstructure in printed parts. Similar findings have been reported in the literature [53] where higher true density at increased w/c ratio was attributed to the potential of natural carbonation.

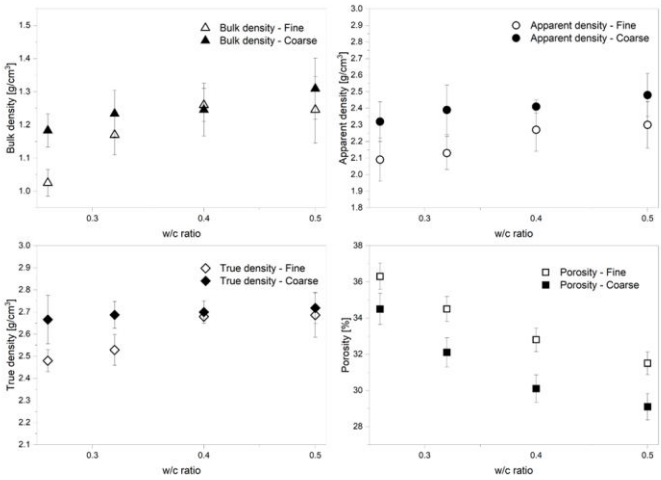

Figure IV: Density and porosity of 3D printed samples for variable w/c ratio

The flexural strength at various water-to-cement ratios and after different curing times is shown in Figure V. The strength of some samples after one day of curing was too weak and was not reported here. Notably, the relationship between flexural strength and water-to-cement ratio is substantially positive.

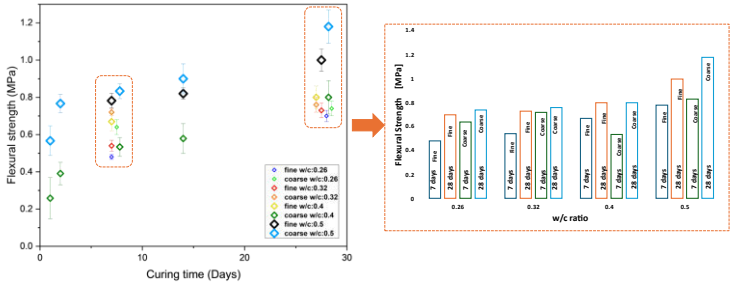

Figure V: Effect of water-cement ratio on flexural strength at different curing time

The effect can be related to the larger amount of water that penetrates between the layers and the sand particles with a beneficial effect on the cement hardening which strengthens the concrete structure, in agreement with previous results [54]. Correspondingly, as the curing time increases, the reactions can evolve thus making the bonding among the aggregate stronger. As the curing time increases, also the compressive strength of specimens cured in the air increases, as shown in Figure VI. The steady rise in compressive strength over time is again indicative of the hydration process occurring in the cementitious materials which therefore become stronger. The conventionally produced concrete specimens were prepared using the same material composition as the 3D-printed specimens but with a water-cement ratio of 0.5. All conventionally produced specimens were cast by pouring the produced mortar into moulds and curing them under ambient conditions. The compressive strength measured for conventionally produced concrete specimens was 9.3 ± 2 MPa after 7 days of curing. Conversely, in the case of the 3D-printed specimen, the compressive strength with a water/cement ratio of 0.5 after 7 days was about 2.5 MPa. This significant gap can be attributed to the fact that traditional casting methods allow denser structures with limited voids thus increasing the material bulk density to 2.1 g/cm3 and improving the compressive strength.

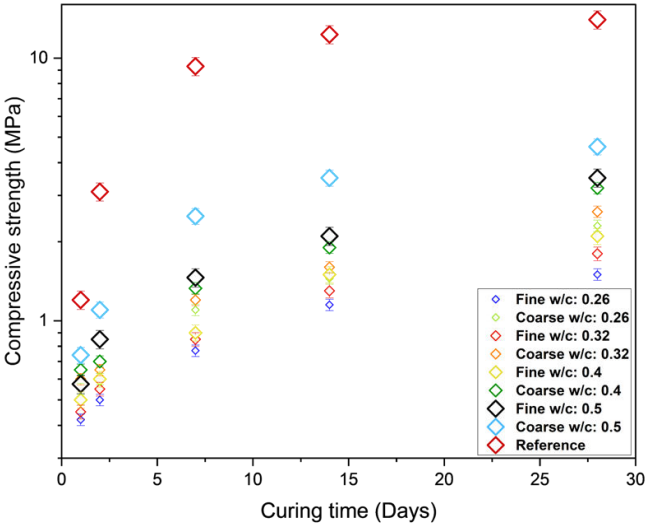

Figure VI: Effect of curing time on compressive strength of Mix – I and Mix-II at different w/c ratio

A clear trend emerges while evaluating the dimensional deviation ratio at different water-to-cement ratios, as shown in Figure VII. This indicates that discrepancies between the actual printed and the intended dimensions increase at higher water-cement ratios. Mix I, which primarily consists of fine particles, shows a much larger dimensional deviation ratio across all axes concerning Mix II.

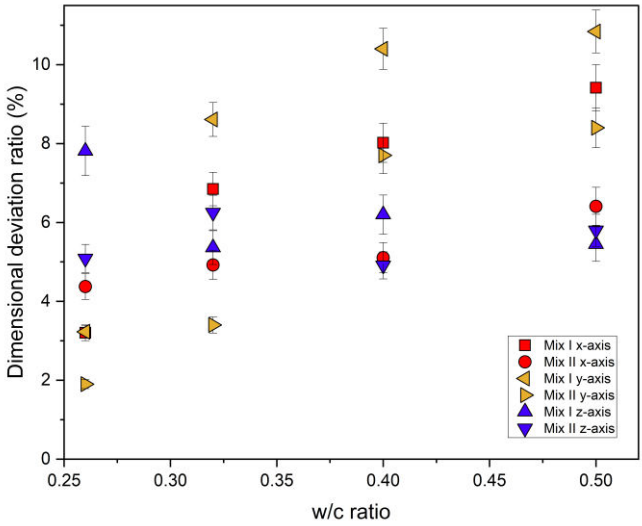

Figure VII: Dimensional deviation ratio for different water-to-cement ratio

The xy-axis printing precision shown in Figure VIII also confirms this trend. Each point is the average of three sets of four samples; error bars are also added to reflect variability. However, measurements involving layer shifting, clogging of the nozzle, or misinterpretation of CAD data were excluded. Notably, Mix-I is characterized by a higher discrepancy between the designed and the real dimensions than Mix-II, the effect being more evident for a larger water-to-cement ratio.

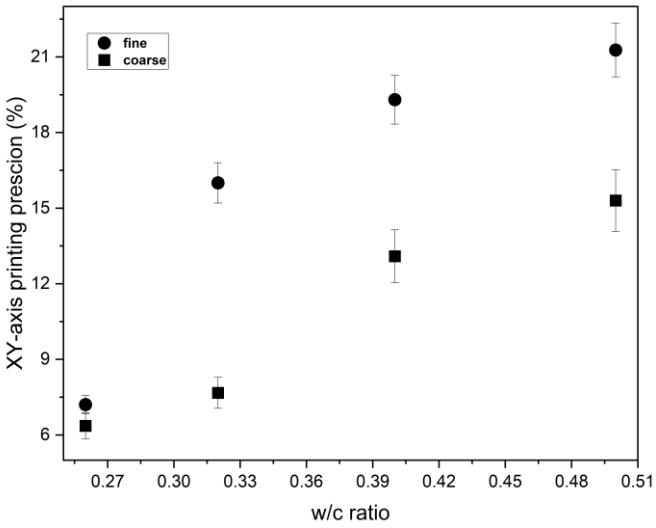

Figure VIII: XY-axis printing precision as a function of w/c ratio

The findings of this study are consistent with earlier research [55], which showed that when the water-to-cement ratio increases, so does the flow rate, which in turn causes the fluid pressure to rise and stronger interlayer connections to form. However, our findings further explore the variables affecting the printing precision and dimensional deviation ratio in binder jetting. Mix-II, which contains coarser aggregate, has a strong structure that allows for efficient water absorption by the powder bed, limiting bleeding and promoting subsequent cement-particle contact. On the other hand, bleeding may deviate more from the 3D geometry dimension in Mix-I, which contains finer siliceous sand, resulting in enlarging the area where cement particles contact. In conclusion, our findings point out a decrease in printing accuracy as the water-to-cement ratio rises.

3.5 Conclusion

The present study investigated the effect of two different mixtures produced with coarse and fine siliceous sand and quick-setting cement at different w/c ratios on the mechanical properties and printing precision of BJ3DP components.
The following important conclusions can be drawn from this work:

- The significant difference in density between specimens with bigger and smaller aggregates points out the crucial impact of aggregate size; minor density changes were observed with increasing water-cement ratio. The porosity of the specimen gradually decreases with increasing water/cement ratio.
- With the increase of the water-cement ratio flexural and compressive strength shows an increasing trend. The effect of different aggregate grain sizes, however, is negligible. Strength also improves significantly at longer curing time.
- Larger dimensional deviation ratios associated with finer aggregates highlight the need to adjust these parameters to achieve desired printing precision. In addition, decreasing the water-cement ratio improves printing accuracy.

In conclusion, mixture containing coarse aggregate exhibits good mechanical properties as the water cement ratio increases. These findings suggest that the performance of 3D-printed concrete can be optimized by adjusting grain size distribution and water-to-cement ratio.

References

[1] C. Gosselin, R. Duballet, P. Roux, N. Gaudillière, J. Dirrenberger, P. Morel, Large-scale 3D printing of ultra-high performance concrete – a new processing route for architects and builders, Mater Des 100 (2016) 102–109. https://doi.org/10.1016/J.MATDES.2016.03.097.

[2] I. Hager, A. Golonka, R.P.-P. Engineering, undefined 2016, 3D printing of buildings and building components as the future of sustainable construction?, Elsevier (n.d.). https://www.sciencedirect.com/science/article/pii/S1877705816317453 (accessed September 7, 2023).

[3] F. Bertolini, M. Mariani, E. Mercadelli, C. Baldisserri, C. Galassi, C. Capiani, R. Ardito, N. Lecis, 3D printing of potassium sodium niobate by binder jetting: Printing parameters optimisation and correlation to final porosity, Journal of Materials Research and Technology 29 (2024) 4597–4606. https://doi.org/10.1016/J.JMRT.2024.02.145.

[4] X. Liu, X. Zhao, N. Wang, Y. Zhang, Z. Dai, Powder-based 3D printed magnesium phosphate cement: Mechanical isotropy optimization using borax, Constr Build Mater 432 (2024) 136660. https://doi.org/10.1016/J.CONBUILDMAT.2024.136660.

[5] O. Davtalab, A. Kazemian, B. Khoshnevis, Perspectives on a BIM-integrated software platform for robotic construction through Contour Crafting, Autom Constr 89 (2018) 13–23. https://doi.org/10.1016/J.AUTCON.2018.01.006.

[6] S.C. Paul, G.P.A.G. van Zijl, I. Gibson, A review of 3D concrete printing systems and materials properties: current status and future research prospects, Rapid Prototyp J 24 (2018) 784–798. https://doi.org/10.1108/RPJ-09-2016-0154/FULL/HTML.

[7] F. Bos, R. Wolfs, Z. Ahmed, T.S.-V. and physical prototyping, undefined 2016, Additive manufacturing of concrete in construction: potentials and challenges of 3D concrete printing, Taylor & Francis 11 (2016) 209–225. https://doi.org/10.1080/17452759.2016.1209867.

[8] M. Li, X. Wei, Z. Pei, C. Ma, Binder jetting additive manufacturing: observations of compaction-induced powder bed surface defects, Manuf Lett 28 (2021) 50–53. https://doi.org/10.1016/j.mfglet.2021.04.003.

[9] I. Gibson, D. Rosen, B. Stucker, M. Khorasani, Development of Additive Manufacturing Technology, Additive Manufacturing Technologies (2021) 23–51. https://doi.org/10.1007/978-3-030-56127-7_2.

[10] A. Mostafaei, A.M. Elliott, J.E. Barnes, F. Li, W. Tan, C.L. Cramer, P. Nandwana, M. Chmielus, Binder jet 3D printing—Process parameters, materials, properties, modeling, and challenges, Prog Mater Sci 119 (2021) 100707. https://doi.org/10.1016/J.PMATSCI.2020.100707.

[11] F. Liravi, V. Jacob-John, A. Toyserkani, M. Vlasea, A Hybrid Method for Additive Manufacturing of Silicone Structures, (2017). https://doi.org/10.26153/16914.

[12] M. Shahid, V.M. Sglavo, Binder Jetting 3D Printing of Binary Cement—Siliceous Sand Mixture, Materials 2024, Vol. 17, Page 1514 17 (2024) 1514. https://doi.org/10.3390/MA17071514.

[13] M. Xia, B. Nematollahi, J. Sanjayan, Influence of Binder Saturation Level on Compressive Strength and Dimensional Accuracy of Powder-Based 3D Printed Geopolymer, Materials Science Forum 939 (2018) 177–183. https://doi.org/10.4028/WWW.SCIENTIFIC.NET/MSF.939.177.

[14] M. Xia, B. Nematollahi, J. Sanjayan, Compressive strength and dimensional accuracy of portland cement mortar made using powder-based 3D printing for construction applications, RILEM Bookseries 19 (2019) 245–254. https://doi.org/10.1007/978-3-319-99519-9_23/FIGURES/5.

[15] M. Xia, B. Nematollahi, J. Sanjayan, Printability, accuracy and strength of geopolymer made using powder-based 3D printing for construction applications, Autom Constr 101 (2019) 179–189. https://doi.org/10.1016/j.autcon.2019.01.013.

[16] P. Shakor, S. Nejadi, G. Paul, Investigation into the effect of delays between printed layers on the mechanical strength of inkjet 3DP mortar, Manuf Lett 23 (2020) 19–22. https://doi.org/10.1016/j.mfglet.2019.11.004.

[17] P. Shakor, S. Nejadi, N. Gowripalan, Effect of Heat Curing and E6-Glass Fibre Reinforcement Addition on Powder-Based 3DP Cement Mortar, RILEM Bookseries 28 (2020) 508–515. https://doi.org/10.1007/978-3-030-49916-7_52/FIGURES/4.

[18] Z. Zhou, C. Mitchell, F. Buchanan, N. Dunne, Effects of Heat Treatment on the Mechanical and Degradation Properties of 3D-Printed Calcium-Sulphate-Based Scaffolds, ISRN Biomaterials 2013 (2012).

[19] B. Panda, S. Chandra Paul, M. Jen Tan, Anisotropic mechanical performance of 3D printed fiber reinforced sustainable construction material,

Mater Lett 209 (2017) 146–149. https://doi.org/10.1016/J.MATLET.2017.07.123.

[20] P. Odaglia, V. Voney, B. Dillenburger, G. Habert, Advances in Binder-Jet 3D Printing of Non-cementitious Materials, RILEM Bookseries 28 (2020) 103–112. https://doi.org/10.1007/978-3-030-49916-7_11/FIGURES/7.

[21] New Trends in 3D Printing, (2016).

[22] G. Gibbons, R. Williams, … P.P.-A. in A., undefined 2010, 3D Printing of cement composites, Taylor & Francis 109 (2010) 287–290. https://doi.org/10.1179/174367509X12472364600878.

[23] E. Lloret, A.R. Shahab, M. Linus, R.J. Flatt, F. Gramazio, M. Kohler, S. Langenberg, Complex concrete structures: Merging existing casting techniques with digital fabrication, Computer-Aided Design 60 (2015) 40–49. https://doi.org/10.1016/J.CAD.2014.02.011.

[24] A.K. Maier, L. Dezmirean, J. Will, P. Greil, Three-dimensional printing of flash-setting calcium aluminate cement, J Mater Sci 46 (2011) 2947–2954. https://doi.org/10.1007/S10853-010-5170-4/FIGURES/7.

[25] S. Benvenuti, F. Ceccanti, X. De Kestelier, Living on the Moon: Topological Optimization of a 3D-Printed Lunar Shelter, Nexus Netw J 15 (2013) 285–302. https://doi.org/10.1007/S00004-013-0155-7.

[26] M.K. Mohan, A. V. Rahul, G. De Schutter, K. Van Tittelboom, Early age hydration, rheology and pumping characteristics of CSA cement-based 3D printable concrete, Constr Build Mater 275 (2021). https://doi.org/10.1016/J.CONBUILDMAT.2020.122136.

[27] A. Al Turk, G. Weheba, 3D printing of Portland cement using a binder jetting system, (2021). https://soar.wichita.edu/bitstream/handle/10057/24775/Turk%20and%20Weheba_v.14,no.1(2021).pdf?sequence=1 (accessed April 5, 2024).

[28] O. Na, K. Kim, H. Lee, H. Lee, Printability and Setting Time of CSA Cement with Na2SiO3 and Gypsum for Binder Jetting 3D Printing, Materials 2021, Vol. 14, Page 2811 14 (2021) 2811. https://doi.org/10.3390/MA14112811.

[29] P. Shakor, J. Sanjayan, A. Nazari, S. Nejadi, Modified 3D printed powder to cement-based material and mechanical properties of cement scaffold used in 3D printing, Constr Build Mater 138 (2017) 398–409. https://doi.org/10.1016/j.conbuildmat.2017.02.037.

[30] P. Shakor, S. Nejadi, G. Paul, J. Sanjayan, A. Nazari, Mechanical Properties of Cement-Based Materials and Effect of Elevated Temperature on 3-D Printed Mortar Specimens in Inkjet 3-D Printing, ACI Mater J 116 (2019) 55–67. https://doi.org/10.14359/51714452.

[31] A. Ur Rehman, V.M. Sglavo, 3D printing of Portland cement-containing bodies, Rapid Prototyp J 28 (2022) 197–203. https://doi.org/10.1108/RPJ-08-2020-0195.

[32] J. Pegna, Exploratory investigation of solid freeform construction, Autom Constr 5 (1997) 427–437. https://doi.org/10.1016/S0926-5805(96)00166-5.

[33] D. Lowke, E. Dini, A. Perrot, D. Weger, C. Gehlen, B. Dillenburger, Particle-bed 3D printing in concrete construction – Possibilities and challenges, Cem Concr Res 112 (2018) 50–65. https://doi.org/10.1016/j.cemconres.2018.05.018.

[34] A. Pierre, D. Weger, A. Perrot, D. Lowke, Penetration of cement pastes into sand packings during 3D printing: analytical and experimental study, Materials and Structures/Materiaux et Constructions 51 (2018) 1–12. https://doi.org/10.1617/S11527-018-1148-5/FIGURES/12.

[35] M. Xia, B. Nematollahi, J. Sanjayan, Compressive strength and dimensional accuracy of portland cement mortar made using powder-based 3D printing for construction applications, RILEM Bookseries 19 (2019) 245–254. https://doi.org/10.1007/978-3-319-99519-9_23/FIGURES/5.

[36] D. Lowke, D. Talke, I. Dressler, D. Weger, C. Gehlen, C. Ostertag, R. Rael, Particle bed 3D printing by selective cement activation – Applications, material and process technology, Cem Concr Res 134 (2020). https://doi.org/10.1016/j.cemconres.2020.106077.

[37] P. McEleney, G. Walker, J. Orr, N.J. Dunne, Investigations on drop penetration and wetting characteristics of powder-liquid systems in relation to the mixing of acrylic bone cement, International Journal of Nano and Biomaterials 3 (2010) 20–35. https://doi.org/10.1504/IJNBM.2010.036105.

[38] H. Miyanaji, N. Momenzadeh, L. Yang, Effect of printing speed on quality of printed parts in Binder Jetting Process, Addit Manuf 20 (2018) 1–10. https://doi.org/10.1016/J.ADDMA.2017.12.008.

[39] A. Butscher, M. Bohner, N. Doebelin, S. Hofmann, R. Müller, New depowdering-friendly designs for three-dimensional printing of calcium phosphate bone substitutes, Acta Biomater 9 (2013) 9149–9158. https://doi.org/10.1016/J.ACTBIO.2013.07.019.

[40] P. Shakor, S. Nejadi, G. Paul, J. Sanjayan, Dimensional accuracy, flowability, wettability, and porosity in inkjet 3DP for gypsum and cement mortar materials, Autom Constr 110 (2020) 102964. https://doi.org/10.1016/j.autcon.2019.102964.

[41] D. Geldart, E.C. Abdullah, A. Hassanpour, L.C. Nwoke, I. Wouters, CHARACTERIZATION OF POWDER FLOWABILITY USING MEASUREMENT OF ANGLE OF REPOSE, CHINA PARTICUOLOGY 4 (2006) 3–4.

[42] M. Moghadasi, W. Du, M. Li, Z. Pei, C. Ma, Ceramic binder jetting additive manufacturing: Effects of particle size on feedstock powder and final part properties, (2020). https://doi.org/10.1016/j.ceramint.2020.03.280.

[43] W. Du, X. Ren, Z. Pei, C. Ma, Ceramic Binder Jetting Additive Manufacturing: A Literature Review on Density, Journal of Manufacturing Science and Engineering, Transactions of the ASME 142 (2020). https://doi.org/10.1115/1.4046248/1074276.

[44] Y.F. Ling, P. Zhang, J. Wang, Y. Shi, Effect of Sand Size on Mechanical Performance of Cement-Based Composite Containing PVA Fibers and Nano-SiO2, Materials 2020, Vol. 13, Page 325 13 (2020) 325. https://doi.org/10.3390/MA13020325.

[45] J. Ingaglio, J. Fox, C.J. Naito, P. Bocchini, Material characteristics of binder jet 3D printed hydrated CSA cement with the addition of fine aggregates, Constr Build Mater 206 (2019) 494–503. https://doi.org/10.1016/j.conbuildmat.2019.02.065.

[46] X. Fan, N. Travitzky, P. Greil, Y. Ma, X. Yin, X. Fan, N. Travitzky, P. Greil, Fabrication of MAX-phase-based ceramics by three-dimensional printing, Researchgate.Net (2015) 6–8. https://doi.org/10.4416/JCST2015-00006.

[47] S.Y. Chun, T. Kim, B. Ye, M.J. Lee, G. Lee, B. Jeong, H. Lee, H.D. Kim, Penetrated surface characteristics of cement - mixed sand in powder bed 3D printing, Https://Doi.Org/10.1080/21870764.2021.2024734 10 (2022) 306–313. https://doi.org/10.1080/21870764.2021.2024734.

[48] P. Yang, S.K.A.O. Nair, N. Neithalath, Discrete element simulations of rheological response of cementitious binders as applied to 3D printing, RILEM Bookseries 19 (2019) 102–112. https://doi.org/10.1007/978-3-319-99519-9_10/FIGURES/7.

[49] L.N. Rabinskiy, S.A. Sitnikov, V.A. Pogodin, A.A. Ripetskiy, Y.O. Solyaev, Binder Jetting of Si3N4 Ceramics with Different Porosity, Solid State Phenomena 269 (2017) 37–50. https://doi.org/10.4028/WWW.SCIENTIFIC.NET/SSP.269.37.

[50] ASTM D7481, D7481 Standard Test Methods for Determining Loose and Tapped Bulk Densities of Powders using a Graduated Cylinder, (n.d.). https://www.astm.org/d7481-09.html (accessed September 7, 2023).

[51] EN 196-1:2016 - Methods of testing cement - Part 1: Determination of strength, (n.d.). https://standards.iteh.ai/catalog/standards/cen/37b8816e-4085-4dcc-a642-a383d9bddd6c/en-196-1-2016 (accessed June 18, 2024).

[52] C642 Standard Test Method for Density, Absorption, and Voids in Hardened Concrete, (n.d.). https://www.astm.org/c0642-21.html (accessed November 6, 2024).

[53] T. Tracz, T. Zdeb, Effect of hydration and carbonation progress on the porosity and permeability of cement pastes, Materials 12 (2019). https://doi.org/10.3390/ma12010192.

[54] M. Abas, A. Salem, R.K. Pandey, Effect of Cement-Water Ratio on Compressive Strengthand Density of Concrete, n.d. www.ijert.org.

[55] F. Salari, P. Bosetti, V.M. Sglavo, Binder Jetting 3D Printing of Magnesium Oxychloride Cement-Based Materials: Parametric Analysis of Manufacturing Factors, Journal of Manufacturing and Materials Processing 2022, Vol. 6, Page 86 6 (2022) 86. https://doi.org/10.3390/JMMP6040086.

Binder Jetting 3D Printing of Binary Cement—Siliceous Sand Mixture

“Binder Jetting 3D Printing of Binary Cement—Siliceous Sand Mixture”,
Mursaleen Shahid, Vincenzo M. Sglavo
Materials 2024, 17, 1514.

4.1 Abstract

3D printing allows to obtain accurate geometries across a wide range of applications and it is now facing also in the architecture and construction industry. In the present work, a unique binary mix composed of ordinary Portland cement (OPC) and quick-setting cement (QSC) was combined with silica sand aggregate in different proportions for a customized binder jetting 3D printing (BJ3DP) process. Specimens were printed using such blended dry powder with deionized water to find the impact of processing variables on the properties of the realized specimens. The results show that the properties are influenced by the binary mix proportion and the layer thickness. The investigation points out significant improvements in the mechanical performances by increasing the proportion of OPC and optimal conditions were identified at a mixed proportion of 35 wt% OPC and 5 wt% QSC. Notable enhancements are also observed as the layer thickness is reduced.

4.2 Introduction

The early development of 3D printing technology, commonly referred to as Additive Manufacturing (AM), began in the early 1980s [1]. This technique has brought a disruptive impact across numerous technologies [2–8]. Apart from the type of AM techniques as per ASTM standards[9] , the primary benefit of AM is its capacity to convert complex shapes from CAD files into physical prototypes [10]. Its usage for concrete printing has reduced the cost by up to 60 % based on the removal of formwork [11,12]. Robocasting and binder jetting are the two most adaptable techniques of AM in the field of construction, the former being mainly categorized in terms of material extrusion-based printing techniques [13] where interfacial porosity and low printing accuracy represent some specific drawbacks [14].

Binder jetting 3D printing (BJ3DP) technology was firstly proposed in 1993 at MIT [15–17] and it has some additional benefits compared to robocasting. The main advantage is that the material around the printed shape acts as a support [18] and, therefore, no additional scaffolds are required. Additionally, the removal of the un-bounded dry powder is easier for large, printed bodies and this technique is more ap-propriate for high scalability [19]. In said 3D printing technique one start with the build platform which is carefully covered with a fine layer of powder; particle distri-bution, size and

shape have an impact on the powder bed, which is important for later stages [20–22]. Subsequently, a liquid binder is selectively sprayed onto the powder layer by a precision inkjet printhead, and it binds the particles together in line with the digital design. The powder bed is then lowered to facilitate the spread of the next powder layer and the process continues layer-by-layer until the entire body immersed in unbounded powder is realized [23–28]. The finished geometry is then carefully separated from the unbounded powder using a vacuum or a brush [29–31].

The first binder used in the BJ3DP technology was calcium sulphate hemihydrate (generally referred as gypsum or plaster) [32]. The work of Zhou et al. mainly describes the procedure and process parameters of powder-based printing. Their findings conclude that fine powder is a general choice for high-resolution parts. Nevertheless, the choice of the layer thickness is mainly dependent on the maximum aggregate size. The BJ3DP process relies on the flowability of the powder which stands as a critical parameter. Maintaining a consistent flowability is essential for achieving the desired outcomes. A one-dimensional powder representation can be used to concisely describe flowability and provide a scale for grading powders accordingly. Powder flowability is typically measured using several parameters, such as the Hausner ratio, angle of repose, flow through an orifice, Carr's compressibility index, Shear cell method and cohesion index. These methods, which have been widely referenced in the literature [33–35], provide a comprehensive understanding of the various facets of powder behaviour in various contexts. Powders with low flowability can reduce the resolution of the printed item while high flowability powders help to improve resolution in the finished printed product. Among other parameters, Hausner ratio and Carr's index are vital reference points for describing the powder's flow characteristics. In general, Hausner ratio values less than 1.25 indicate good to exceptional flowability, while values more than 1.25 may indicate flowability issues. Carr's index values are also thought to indicate great flow when they are less than 15% and impaired flowability when they are larger than 25%. These specified ranges aid in the development of an extensive framework for assessing the powder's flow properties.

The type of cement used has a major impact on the density and mechanical strength of 3D printed concrete specimens; in addition, changes in density are linked to variations in porosity. Notably, variations in porosity result from the proportion of air-

filled gaps, which affects the weight of the concrete. The density of concrete, on the other hand, is determined by the specific gravity of its aggregate as well as the qualities of the other components. These factors highlight the complex interplay between the mechanical characteristics of 3D printed concrete structures, cement type and perceived density.

The goal of improving the physical and mechanical properties of the printed material can be achieved by optimizing the process parameters [36]. For all types of Additive Manufacturing processes, the layer thickness is the printing parameter that matters most [37]. When considering the thickness of a deposited layer, it has a significant impact on the characteristics of printed items including strength, printing time and quality of the printed geometry [38–41]. The calculation of layer thickness is intricately tied to the resolution of the printing component and particle size [42]. Yu et al.[43] investigated the void size distribution and mechanical performance of 3D-printed concrete using Mercury Intrusion Porosimetry (MIP) and X-ray Computed Tomography (CT). The obtained results show that 3D-printed materials have more macropores and big voids, which are related to printhead movement, decreased vibration and quick moisture loss. By comparing these specimens to mold-cast ones, the void morphologies are noticeably more irregular and extended, especially between layers, and this results in decreased strength. The time elapsed between successive printing layers affects the air voids in concrete [44]. Xin et al. [45] research focused on a modified cement combination made up of Ordinary Portland Cement (OPC) and rapid-hardening sulpho-aluminate cement. According to their work, specimens produced at lower velocities have larger layer thicknesses and the overall increased height. Using the extrusion-based technique (robocasting), Nair et al. [46] examined the layer thickness effect on the mechanical properties of fiber-reinforced 3D printed beams. Their work concluded that thinner layers are more beneficial for 3D-printed mortars. Ur Rehman et al. [47] explained that the geometrical and mechanical properties of OPC-based materials depend on the specific used binder [48].

The use of binary cement in 3D printing has been shown to be a potentially useful approach to improve mechanical properties. Soltan et al. [49] processed a composite using a modified dry mixture of calcium aluminate cement, fly ash and ordinary Portland Cement. The blend included aggregates of different kinds of silica,

superplasticizer admixtures and viscosity modifiers such as high-performance methylcellulose (HPMC) and nano-clay. Furthermore, 2 vol% polyvinyl alcohol fibers were incorporated. Extrusion with a manually controlled caulk gun was used and the resulting printed specimens showed failure strains between 2 and 4% and tensile strength between 2 and 4 MPa. Shakor et al.[50] also worked on the same binary cement mix of cement OPC and calcium aluminate cement along with Li2CO3 as an activator to reduce the setting time; the maximum compressive strength obtained was 14.68 MPa after 28 days. In another work [51], they emphasized the impact of heat curing on the mechanical properties of the same modified binary cement. In the study by Anderson et al. [52], four different kinds of plasters and particulate materials were analysed, in-corporating an aqueous solution composed of 95% water and 5% humectant and glycerol; potassium sulfate was also added as an accelerator.

In another work, Gibbons et al. [53] selected a superior composition consisting of 97 wt% Rapid Hardening Cement and 3 wt% Polyvinyl Alcohol. The researchers tested the material's performance using different curing procedures in water at room temperature and at 80°C. The results were based on different saturation levels for the shell and the core. Their analysis showed that flexural strength decreased because of a reduction in core saturation level. This thorough investigation emphasizes how crucially curing circumstances affect the resulting material's mechanical properties. Similarly, Zhou et al. [54] explored the 3D printing of various powder mixtures containing calcium phosphate and calcium sulphate in a water-based binder. Their goal was to understand the interactions between many factors, such as the wettability of the powder binder, the behaviour of the binder drop penetration, the packing of the powder bed during the process and the final quality of the printed samples. Their results emphasised how crucial calcium phosphate particle size and calcium phosphate/sulphate ratio are as critical elements affecting the 3D printing process. The application of magnesium ammonium phosphate, or struvite, in a neutral setting reaction was investigated in another study [55]. Klammert et al. printed farringtonite ($Mg_3(PO_4)_2$) powder using an ammonium phosphate solution as binder, obtaining a compressive strength ranging from 2 to 7 MPa (290 to 1015 psi). In a different method, Shakor et al. [56] used gypsum hemihydrate in place of cement mortar powder, allowing the resultant parts to be used in building applications.

The present study aims at identifying the most effective composition of binary cement mixture by considering the final mechanical properties and evaluating how the layer thickness during BJ3DP influences them.

4.3 Materials

The starting powder used for the BJ3DP process was composed of quick-setting cement (QSC) from Vicat cement - OBI Italy, ordinary Portland cement, OPC (Tecno-cem 32.5, Italy) and siliceous sand (grade 0.4 - 1.18 mm) from Sabbie di Parma (Italy) in different proportions as shown in Table I. Each composition was carefully mixed in a concrete mixture for 30 min to guarantee homogeneity of the dry mixture. Deionized water was used as liquid binder. Both OPC and QSC are hydraulic binding materials where OPC exhibits standard setting time and consists mainly of Portland cement clinker, the appropriate amount of gypsum and some percentage of blended materials. Conversely, quick-setting cement is formulated to take less time to set and harden when compared to Portland cement. This strategic blend aims at balancing the strength development and setting time of the 3D printed specimens.

Table I: Composition of the dry mixtures used in the BJ3DP process

Mixture	Content (Sand:OPC: QSC) wt%
Mix-I	50:40:10
Mix-II	60:35:5
Mix-III	70:30:0
Mix-IV	70:25:5
Mix-V	70:20:10
Mix-VI	70:15:15
Mix-VII	75:25:0

4.4 Methodology

A customized 3D printer was employed to produce concrete-based specimens through a sequential layering process. The schematic of a customized 3D printer is shown in Figure I.

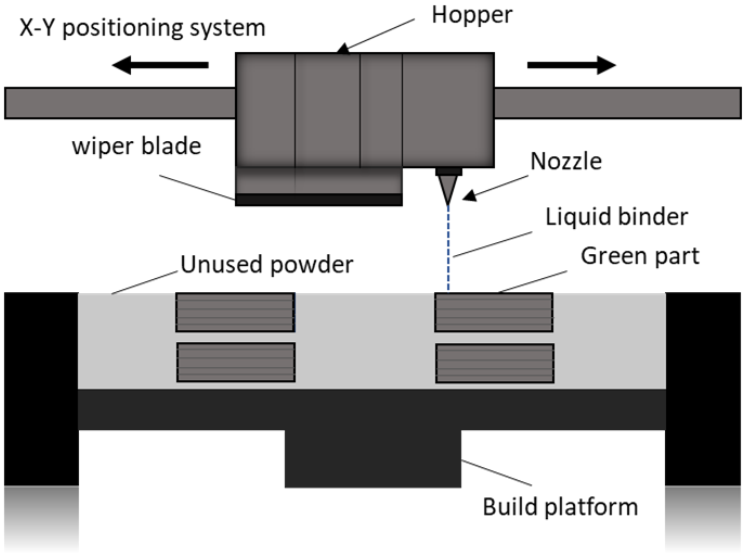

Figure I: Schematic of 3D printing machine

The printer was equipped with a pressurized opening and closing of a hopper for dry powder supply and a liquid binder dispensing system. The dry powder was deposited on the powder bed in the X direction where a wiper blade allowed to uniformly distribute the powder on the bed. A Staiger valve along with a nozzle of internal diameter 0.19 mm by Lee Co. (USA) was used for a drop-on-demand supply of the water. The pressure was controlled by the system's precision valve to provide the needed amount of binder and these values were monitored and recorded by a pressure sensor. In the regions where water was in contact with dry powder, the part consolidated it being surrounded by the unaffected dry powder which continued to

serve as a supportive material. Printed parts were allowed for 24 h controlled curing within the powder bed in the lab atmosphere. Subsequently, they were extracted from the powder bed and the excess dry powder attached to the printed surface was carefully removed. The printed specimens were placed under the hood to cure at the temperature of 20-25 ^{o}C while maintaining the humidity of 50%. The specimens' CAD model was created using SolidWorks to obtain the geometries suitable for flexural and compressive strength testing and it was then sliced to generate a G-code script that was associated to each printing batch. The details of the 3D printing process were defined by such G-code program, which contained parameters like hatch distance, feed rate, print head height from the powder bed and layer thickness.

The hatch distance and the print head from the powder bed were maintained at 2 mm and 10 mm, respectively and the layer thickness was varied from 1 mm to 2 mm. To ensure stable water-cement ratios and similar outcomes for varied layer thicknesses, the feed rate was regulated within the range of 7.2 to 14.0 m/min.

The Hausner ratio and the Carrs Index are discussed in this paper to describe the flowability of the mixtures. Hausner ratio (HR) is calculated by dividing the tapped density ρ_t by the bulk density ρ_b as:

$$HR = \frac{\rho_t}{\rho_b} \tag{1}$$

Carr's index which expresses the material compressibility is calculated using the following relation:

$$CI = \frac{\rho_b - \rho_t}{\rho_b} x100 \tag{2}$$

Notably, Hausner ratios below 1.25 imply exceptional flowability, whilst values beyond this cutoff can suggest possible flowability problems. Comparably, values of Carr's index that are less than 15% indicate optimal flow, whereas values that are more than 25% may indicate poor flowability. The evaluation criteria used in this study are

compatible with accepted standards and procedures specified in previous research [34].

Apparent density of the printed specimens was measured in accordance with ASTM C 642 norm [57]. The specimens were first oven-dried for at least 24 h at 110 °C. They were then immersed in water for 48 h and boiled for 5 h in beaker on a hot plate and cooled for 3 h by immersion in water. Following the steps specified in the cited norm, the mass of the specimens was carefully reported at every stage.

Standardized parameters described in the EN-196-1 norm were carefully followed in the creation of specimens for both three-point bending and compressive strength test [58]. Specimens of dimensions 160 mm x 40 mm x 40 mm and 40 mm edge cubes were printed for the flexural and compressive strength testing respectively.

The mechanical tests were carried out by using a universal testing machine (Model 810, MTS System, USA). Bending tests were performed with a rate of 50 N/s. The flexural strength was calculated as:

$$f_f = \frac{3FL}{2bd^2} \tag{3}$$

where F is the failure load, L the span length (140 mm), b and d the specimen width and thickness, respectively.

Compression tests were performed with a rate of 2400 N/s and the compressive strength was determined as:

$$f_c = \frac{F_c}{A} \tag{4}$$

where Fc is the failure load and A the specimen cross sectional area. Here the constant loading rate was kept at 2400 N/s.

SEM analysis was conducted on seven-day cured specimens printed with layer thicknesses of 1 mm and 1.5 mm. Carefully polished specimens were used for the

SEM analysis. The samples were dried in an oven set at 105°C. They were carefully cleaned with ethanol and coated with a nonometric layer of Pt-Pd alloy to make the electrically conductive so to be suitable for the analysis by SEM (JEOL, JSM5500) according to the ASTM C 1723 [59] norm.

The lateral surface of the 3D printed specimens was examined also using a digital microscope (DSX 1000, Olympus, Italy). After 7 days curing, specimens printed with layer thicknesses of 1 mm and 2 mm were analysed.

4.5 Results

The macroscopic pictures shown in Figure II provide important information about the appearance of the printed specimens and how they relate to the mix ratios that were used. One noteworthy finding is the considerable color variation among the specimens, which suggests discrete compositional variations brought about by variations in the mix ratio. This color variation highlights the sensitivity of additive manufacturing to minute changes in formulation. It may result from variations in material composition, density, or chemical reactions occurring during the printing process. Additionally, nozzle blockage in the mix-VII specimen is an important observation since it affects the final geometry's finishing. Nozzle blockage can cause inconsistencies in layer deposition and reduced structural integrity by interfering with the extrusion process. This result emphasizes how crucial it is to optimize material compositions and printing conditions in order to reduce the possibility of printing errors and guarantee reliable print quality. Overall, the macroscopic examination of printed specimens reveals opportunities for additive manufacturing process optimization and offers insightful qualitative information about the effects of mix ratio variations.

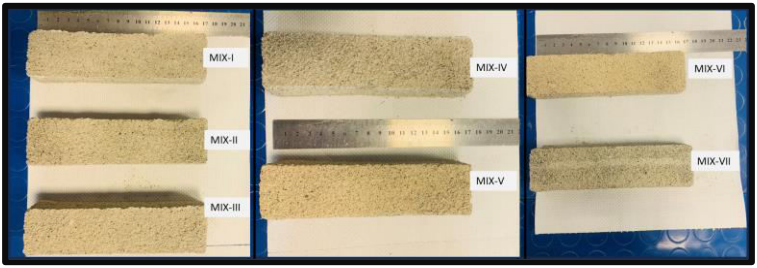

Figure II: Top view of the images printed at varying mix ratio

4.5.1 Flowability

The flowability of Mix-I to Mix-VII was measured and the data in Table II clearly show that the Hausner ratio and the Carr's index decrease together when one moves from Mix-I to Mix VII. As the mixtures' composition changes, this descending pattern points to a gradual increase in flowability, offering important information on packing and flow properties of the powder.

Table II: Flowability of dry powder mixture

Mixture	HR	CI	Flow Character
Mix-I	1.35	26	Cohesive/poor
Mix-II	1.31	24	Passable
Mix-III	1.28	22	Passable
Mix-IV	1.28	22	Passable
Mix-V	1.21	18	Fair
Mix-VI	1.17	15	Good
Mix-VII	1.23	19	Fair

4.5.2 Density

Figure III shows the relationship between OPC content and apparent density. As the OPC content increases, it likely contributes to improved particle packing, leading to more tight arrangement.

When OPC and quick-setting cement are combined, the increased density is still due to OPC's higher specific gravity.

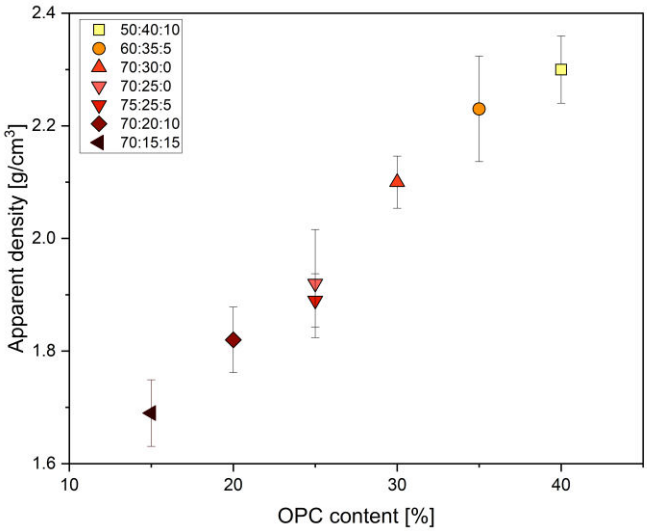

Figure III: Impact of OPC content on the density of 3D printed specimens

4.5.3 Mechanical properties

Figure IV shows the mechanical properties of printed specimens. Throughout the course of the 28-day curing period, mixes II shown a notable superiority in terms of compressive and flexural strengths. The results of these compositions likely promote the interfacial bonding within the concrete [60] and the improved particle packing based of the concrete matrix which improves its mechanical properties. Another

important factor of improved mechanical properties of the mixtures is the specific proportion of the ingredients that may result in superior hydration kinetics and improved microstructural development during the process. Furthermore, it is possible that the chemical interactions and phase transitions that occur within these mixtures during hydration play an important role in reinforcing the material structure and increasing mechanical performance over time.

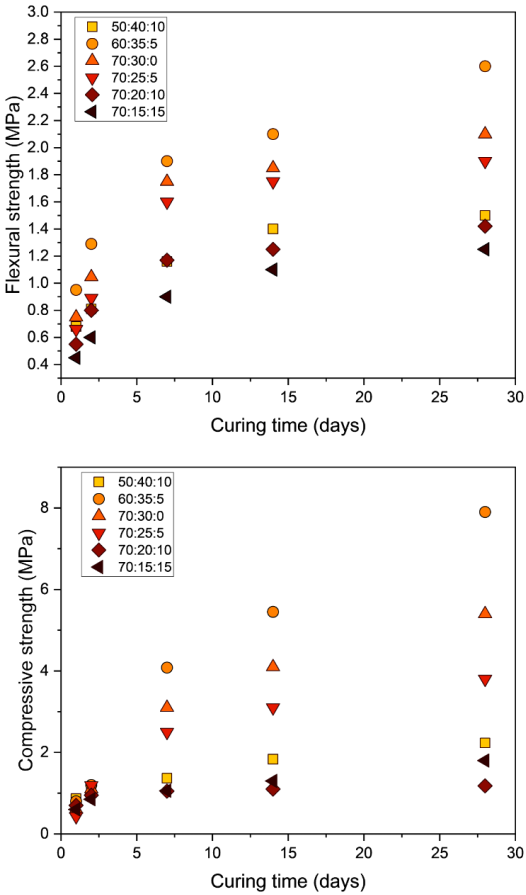

Figure IV: Mechanical properties of printed specimens

The mix proportions utilized in the trials to get the flexural strength findings are shown in Table 1. The results are classified into three zones [61] based on the different proportion of cement content, namely active, inert and deterioration zones. The active zone is the region where larger cement content enhances bonding at grain contact points, leading to increased strength. In the inert zone, the strength development gradually slows down at some level and further addition of cement content decreases the strength instead of improving it thus being named the deterioration zone (Figure V). These results suggest that increasing the cement content beyond a certain limit may not contribute significantly to strength improvement and, for the binary mixture considered here, the limit corresponds to the mix-II.

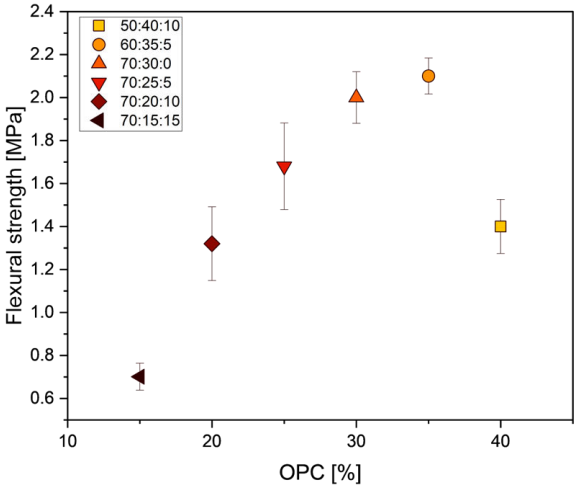

Figure V: Behaviour of 3D printed specimens at varying OPC content across active, Inert and deterioration zone after 7 days of curing

We observe an inverse proportionality between the mechanical strength and the printed layer thickness for mix-VI, as shown in Figure VI. Reduced layer thickness appears to lead to more compact powder bed packing, stability and uniformity, these contributing to higher strength.

The study identified limitations pertaining to powder size, layer thickness, and flowability, all of which are essential for attaining the best possible outcomes in additive manufacturing. Proper adhesion and compaction are ensured by keeping the powder size lower than the printed layer. Also, proper flowability is necessary for uniform distribution of powder on the bed.

The findings of this study have important significance for the construction sector, particularly in the optimization of concrete mixtures and additive manufacturing techniques. The study determined a particular configuration of mixture that demonstrated better mechanical qualities after 28 days of curing by thoroughly examining several combinations of binary mixtures. For professionals in the industry looking to improve the performance of concrete compositions, this finding provides insightful information. Furthermore, layer thickness study demonstrated that lowering the thickness from 2 mm to 1 mm using concrete binder jetting resulted in increased performance.

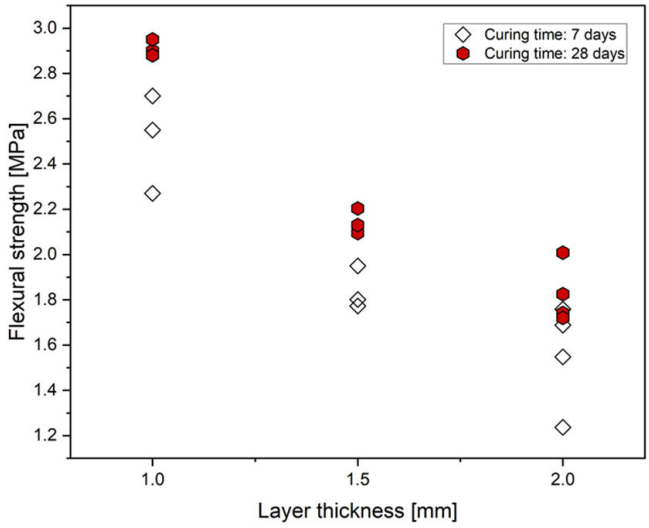

Figure VI: Flexural strength of 3D printed specimens at varying layer thickness

4.5.4 Microscopic Analysis

To analyse further the impact of layer thickness, side view images of printed specimens from optical digital microscope and top surface SEM images of the polished specimens are shown in Figure VII and VIII. The SEM images clearly show the voids that can also be observed at higher value of layer thickness. The images suggest that reduced strength at higher layer thickness in Figure VI is linked to larger number of voids.

Apart from the trends that have been noted in terms of void formation and mechanical strength, it is imperative to take into account the compaction behavior of the printed layers about variation in layer thickness. Since the wiper blade is applied consistently, the compaction of each layer becomes more uniform as the layer thickness decreases, resulting in more densely packed layers. The reason for this improved com-paction is because the material is deposited over a reduced distance, which facilitates greater consolidation of the printed layers. On the other hand, specimens created at larger layer thicknesses can show less consistent compaction because of the possibility of uneven material distribution and compaction due to the increased distance between layers. Thus, decreasing the layer thickness leads to both a decrease in void formation and a greater degree of uniform compaction of the layers, which improves the mechanical strength overall. Future studies could investigate more sophisticated compaction methods and printing strategies to further optimize the compaction process and maximize the mechanical properties of printed concrete structures.

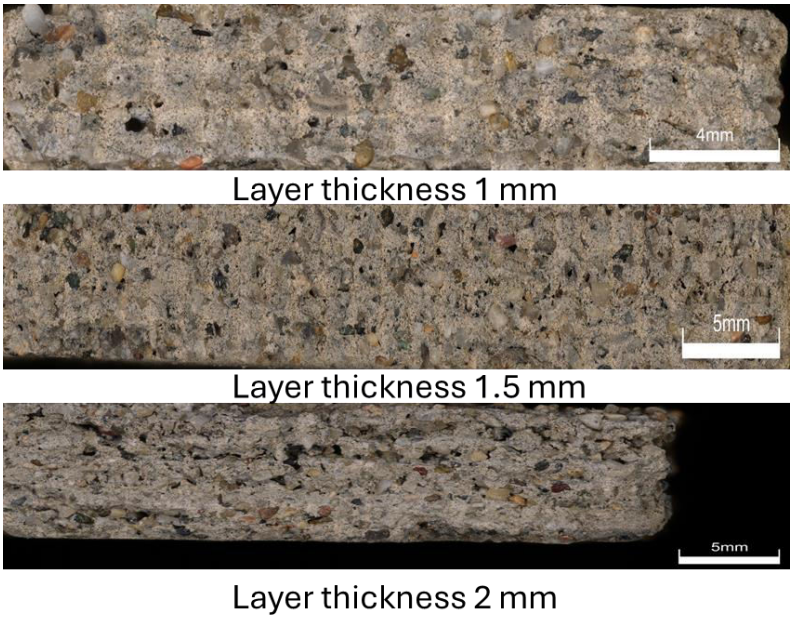

Figure VII: Microscopic optical images of printed samples

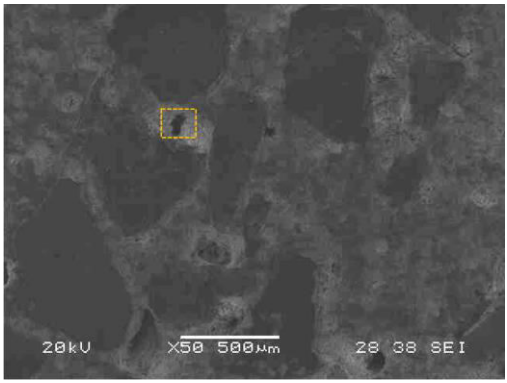

Layer thickness 1 mm

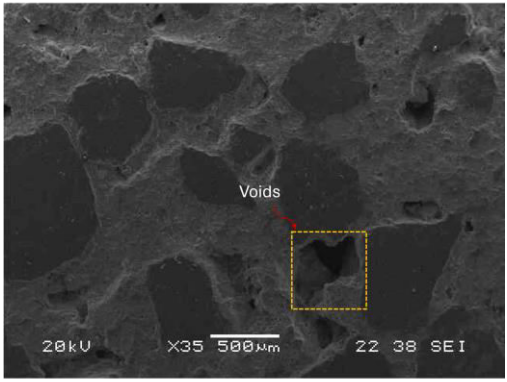

Layer thickness 1.5 mm

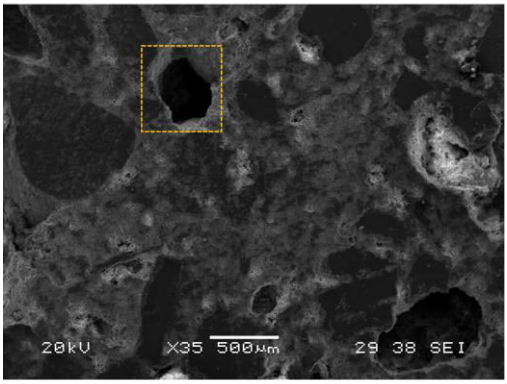

Layer thickness 2 mm

Figure VIII: SEM images of the printed specimens

4.6 Conclusion

The study investigated the behaviour of a modified binary cement mixture composed of ordinary Portland cement and quick setting cement while printing with a customized binder jetting 3D printer.

This work leads to the following significant conclusions.

- The flow characteristics of mixtures with lesser OPC content were good to fair, while those with higher OPC content showed passable to cohesive/poor flow. Hausner ratio (HR) and Carr's index (CI) show that flow dynamics were affected by the steady increase in OPC concentration. These results point out the significance of OPC concentration in determining the general flow behaviour of binary cement mixtures and provide important information for uses in 3D printing technology.

- The OPC content plays a critical role in improving the overall density of the 3D printed specimens. As the proportion of OPC cement exceeds that of quick setting cement, the higher specific gravity of OPC becomes the primary factor in improving the overall density and the mechanical properties of the material.

- Mix VII exhibits relatively high flexural strength, peaking at 1.9 MPa after 7 days and increasing to 2.7 MPa by the 28th day. Further highlighting Mix VII's strong mechanical performance is this positive trend in compressive strength over time.
- Variable binary cement content improves mechanical properties up to 35:5:60 wt% of OPC:QSC:Sand; above that, more cement content causes the strength to decrease.

- The findings show that there is an apparent reduction in mechanical strength as layer thickness increases. This result implies that the mechanical characteristics and layer thickness are inversely related. This observed pattern emphasizes how crucial it is to take layer thickness into account as an essential.

- Microscopic analysis confirms a correlation between strength and voids at different layer thicknesses, the increase in voids appearing as the source of strength decrease. In conclusion, our research clearly shows how layer thickness affects void

formation and mechanical strength in printed concrete samples. As a consequence of the printed layers' more even compaction, our results show that decreasing the layer thickness reduces voids and improves mechanical characteristics.

References

1. Labonnote, N.; Rønnquist, A.; Manum, B.; Rüther, P. Additive Construction: State-of-the-Art, Challenges and Opportunities. *Autom Constr* **2016**, *72*, 347–366, doi:10.1016/J.AUTCON.2016.08.026.
2. Bos, F.; Wolfs, R.; Ahmed, Z.; prototyping, T.S.-V. and physical; 2016, undefined Additive Manufacturing of Concrete in Construction: Potentials and Challenges of 3D Concrete Printing. *Taylor & Francis* **2016**, *11*, 209–225, doi:10.1080/17452759.2016.1209867.
3. Tay, Y.W.D.; Panda, B.; Paul, S.C.; Noor Mohamed, N.A.; Tan, M.J.; Leong, K.F. 3D Printing Trends in Building and Construction Industry: A Review. *https://doi.org/10.1080/17452759.2017.1326724* **2017**, *12*, 261–276, doi:10.1080/17452759.2017.1326724.
4. Miranda, P.; Pajares, A.; Saiz, E.; Tomsia, A.P.; Guiberteau, F. Mechanical Properties of Calcium Phosphate Scaffolds Fabricated by Robocasting. *J Biomed Mater Res A* **2008**, *85*, 218–227, doi:10.1002/JBM.A.31587.
5. Khoshnevis, B. Automated Construction by Contour Crafting - Related Robotics and Information Technologies. *Autom Constr* **2004**, *13*, 5–19, doi:10.1016/j.autcon.2003.08.012.
6. Casas-Luna, M.; Torres-Rodríguez, J.A.; Valdés-Martínez, O.U.; Obradović, N.; Slámečka, K.; Maca, K.; Kaiser, J.; Montúfar, E.B.; Čelko, L. Robocasting of Controlled Porous CaSiO3–SiO2 Structures: Architecture – Strength Relationship and Material Catalytic Behavior. *Ceram Int* **2020**, *46*, 8853–8861, doi:10.1016/J.CERAMINT.2019.12.130.

7. Böckin, D.; Tillman, A.M. Environmental Assessment of Additive Manufacturing in the Automotive Industry. *J Clean Prod* **2019**, *226*, 977–987, doi:10.1016/J.JCLEPRO.2019.04.086.

8. Haleem, A.; Javaid, M. 3D Printed Medical Parts with Different Materials Using Additive Manufacturing. *Clin Epidemiol Glob Health* **2020**, *8*, 215–223, doi:10.1016/J.CEGH.2019.08.002/ATTACHMENT/379404EC-9976-471E-98FC-F379F198C8E5/MMC1.XML.

9. ISO/ASTM 52900:2021 - Additive Manufacturing — General Principles — Fundamentals and Vocabulary Available online: https://www.iso.org/standard/74514.html (accessed on 13 March 2024).

10. Vaezi, M.; Chua, C.K. Effects of Layer Thickness and Binder Saturation Level Parameters on 3D Printing Process. *International Journal of Advanced Manufacturing Technology* **2011**, *53*, 275–284, doi:10.1007/s00170-010-2821-1.

11. Lloret, E.; Shahab, A.R.; Linus, M.; Flatt, R.J.; Gramazio, F.; Kohler, M.; Langenberg, S. Complex Concrete Structures: Merging Existing Casting Techniques with Digital Fabrication. *Computer-Aided Design* **2015**, *60*, 40–49, doi:10.1016/J.CAD.2014.02.011.

12. Johnston, D.W. Design and Construction of Concrete Formwork. *Concrete Construction Engineering Handbook, Second Edition* **2008**, 233–282, doi:10.1201/9781420041217-7.

13. Daguano, J.K.M.B.; Santos, C.; Alves, M.F.R.P.; Silva, J.V.L. da; Souza, M.T.; Fernandes, M.H.F.V. State of the Art in the Use of Bioceramics to Elaborate 3D Structures Using Robocasting. *International Journal of*

Advances in Medical Biotechnology - IJAMB **2019**, *2*, 55–70, doi:10.25061/2595-3931/IJAMB/2019.v2i1.28.

14. Zocca, A.; Colombo, P.; Gomes, C.M.; Günster, J. Additive Manufacturing of Ceramics: Issues, Potentialities, and Opportunities. *Journal of the American Ceramic Society* **2015**, *98*, 1983–2001, doi:10.1111/JACE.13700.
15. Sachs, E.; Cima, M.; Williams, P.; Brancazio, D.; Cornie, J. Three Dimensional Printing: Rapid Tooling and Prototypes Directly from a CAD Model. *Journal of Engineering for Industry* **1992**, *114*, 481–488, doi:10.1115/1.2900701.
16. Ziaee, M.; Crane, N. Binder Jetting: A Review of Process, Materials, and Methods. *Faculty Publications* **2019**.
17. Gibson, I.; Rosen, D.; Stucker, B. Binder Jetting. *Additive Manufacturing Technologies* **2015**, 205–218, doi:10.1007/978-1-4939-2113-3_8.
18. Seitz, H.; Rieder, W.; Irsen, S.; Leukers, B.; Tille, C. Three-Dimensional Printing of Porous Ceramic Scaffolds for Bone Tissue Engineering. *J Biomed Mater Res B Appl Biomater* **2005**, *74B*, 782–788, doi:10.1002/JBM.B.30291.
19. Zocca, A.; Günster, J.; Zocca, A.; Lima, P.; Günster, J. LSD-Based 3D Printing of Alumina Ceramics. *J. Ceram. Sci. Tech* **2017**, 8–9, doi:10.4416/JCST2016-00103.
20. Xia, M.; Nematollahi, B.; Sanjayan, J. Influence of Binder Saturation Level on Compressive Strength and Dimensional Accuracy of Powder-Based 3D Printed Geopolymer. *Materials Science Forum* **2018**, *939*, 177–183, doi:10.4028/WWW.SCIENTIFIC.NET/MSF.939.177.

21. Lv, X.; Ye, F.; Cheng, L.; Fan, S.; Liu, Y. Binder Jetting of Ceramics: Powders, Binders, Printing Parameters, Equipment, and Post-Treatment. *Ceram Int* **2019**, *45*, 12609–12624, doi:10.1016/J.CERAMINT.2019.04.012.

22. Miyanaji, H.; Momenzadeh, N.; Yang, L. Effect of Printing Speed on Quality of Printed Parts in Binder Jetting Process. *Addit Manuf* **2018**, *20*, 1–10, doi:10.1016/J.ADDMA.2017.12.008.

23. Wu, C.; Fan, W.; Zhou, Y.; Luo, Y.; Gelinsky, M.; Chang, J.; Xiao, Y. 3D-Printing of Highly Uniform CaSiO 3 Ceramic Scaffolds: Preparation, Characterization and in Vivo Osteogenesis. *J Mater Chem* **2012**, *22*, 12288–12295, doi:10.1039/C2JM30566F.

24. Bergmann, C.; Lindner, M.; Zhang, W.; Koczur, K.; Kirsten, A.; Telle, R.; Fischer, H. 3D Printing of Bone Substitute Implants Using Calcium Phosphate and Bioactive Glasses. *J Eur Ceram Soc* **2010**, *30*, 2563–2567, doi:10.1016/J.JEURCERAMSOC.2010.04.037.

25. Jones, J.R.; Hench, L.L. Regeneration of Trabecular Bone Using Porous Ceramics. *Curr Opin Solid State Mater Sci* **2003**, *7*, 301–307, doi:10.1016/J.COSSMS.2003.09.012.

26. Utela, B.; Storti, D.; Anderson, R.; Ganter, M. A Review of Process Development Steps for New Material Systems in Three Dimensional Printing (3DP). *J Manuf Process* **2008**, *10*, 96–104, doi:10.1016/J.JMAPRO.2009.03.002.

27. Zhou, Z.; Lennon, A.; Buchanan, F.; McCarthy, H.O.; Dunne, N. Binder Jetting Additive Manufacturing of Hydroxyapatite Powders: Effects of

Adhesives on Geometrical Accuracy and Green Compressive Strength. *Addit Manuf* **2020**, *36*, 101645, doi:10.1016/J.ADDMA.2020.101645.

28. Withell, A.; Diegel, O.; Grupp, I.; Reay, S.; De Beer, D.; Potgieter, J. Porous Ceramic Filters through 3D Printing. *Innovative Developments in Virtual and Physical Prototyping - Proceedings of the 5th International Conference on Advanced Research and Rapid Prototyping* **2012**, 313–318, doi:10.1201/B11341-50.

29. Butscher, A.; Bohner, M.; Doebelin, N.; Hofmann, S.; Müller, R. New Depowdering-Friendly Designs for Three-Dimensional Printing of Calcium Phosphate Bone Substitutes. *Acta Biomater* **2013**, *9*, 9149–9158, doi:10.1016/J.ACTBIO.2013.07.019.

30. Chumnanklang, R.; Panyathanmaporn, T.; Sitthiseripratip, K.; Suwanprateeb, J. 3D Printing of Hydroxyapatite: Effect of Binder Concentration in Pre-Coated Particle on Part Strength. *Materials Science and Engineering: C* **2007**, *27*, 914–921, doi:10.1016/J.MSEC.2006.11.004.

31. Butscher, A.; Bohner, M.; Doebelin, N.; Galea, L.; Loeffel, O.; Müller, R. Moisture Based Three-Dimensional Printing of Calcium Phosphate Structures for Scaffold Engineering. *Acta Biomater* **2013**, *9*, 5369–5378, doi:10.1016/J.ACTBIO.2012.10.009.

32. Zhou, Z.; Mitchell, C.A.; Buchanan, F.J.; Dunne, N.J. Effects of Heat Treatment on the Mechanical and Degradation Properties of 3D-Printed Calcium-Sulphate-Based Scaffolds. *Corporation ISRN Biomaterials* **2013**, *2013*, doi:10.5402/2013/750720.

33. Geldart, D.; Abdullah, E.C.; Hassanpour, A.; Nwoke, L.C.; Wouters, I. CHARACTERIZATION OF POWDER FLOWABILITY USING MEASUREMENT OF ANGLE OF REPOSE. *CHINA PARTICUOLOGY* **2006**, *4*, 3–4.

34. Shakor, P.; Nejadi, S.; Paul, G.; Sanjayan, J. Dimensional Accuracy, Flowability, Wettability, and Porosity in Inkjet 3DP for Gypsum and Cement Mortar Materials. *Autom Constr* **2020**, *110*, 102964, doi:10.1016/j.autcon.2019.102964.

35. Moghadasi, M.; Du, W.; Li, M.; Pei, Z.; Ma, C. Ceramic Binder Jetting Additive Manufacturing: Effects of Particle Size on Feedstock Powder and Final Part Properties. **2020**, doi:10.1016/j.ceramint.2020.03.280.

36. Chen, Y.; Jansen, K.; Zhang, H.; Romero Rodriguez, C.; Gan, Y.; Çopuroğlu, O.; Schlangen, E. Effect of Printing Parameters on Interlayer Bond Strength of 3D Printed Limestone-Calcined Clay-Based Cementitious Materials: An Experimental and Numerical Study. *Constr Build Mater* **2020**, *262*, 120094, doi:10.1016/J.CONBUILDMAT.2020.120094.

37. Du, W. Imece2017-70344 Binder Jetting Additive Manufacturing of Ceramics : A Literature. **2017**, 1–12.

38. Yao, A.W.L.; Tseng, Y.C. A Robust Process Optimization for a Powder Type Rapid Prototyper. *Rapid Prototyp J* **2002**, *8*, 180–189, doi:10.1108/13552540210431004/FULL/PDF.

39. Gonzalez, J.A.; Mireles, J.; Lin, Y.; Wicker, R.B. Characterization of Ceramic Components Fabricated Using Binder Jetting Additive Manufacturing

Technology. *Ceram Int* **2016**, *42*, 10559–10564, doi:10.1016/j.ceramint.2016.03.079.

40. Farzadi, A.; Solati-Hashjin, M.; Asadi-Eydivand, M.; Osman, N.A.A. Effect of Layer Thickness and Printing Orientation on Mechanical Properties and Dimensional Accuracy of 3D Printed Porous Samples for Bone Tissue Engineering. *PLoS One* **2014**, *9*, e108252, doi:10.1371/JOURNAL.PONE.0108252.

41. Dini, F.; Ghaffari, S.A.; Jafar, J.; Hamidreza, R.; Marjan, S. A Review of Binder Jet Process Parameters; Powder, Binder, Printing and Sintering Condition. *Metal Powder Report* **2020**, *75*, 95–100, doi:10.1016/J.MPRP.2019.05.001/ASSET/IMAGES/LARGE/J.MPRP.2019.05.001_GR8.JPEG.

42. Mostafaei, A.; Elliott, A.M.; Barnes, J.E.; Li, F.; Tan, W.; Cramer, C.L.; Nandwana, P.; Chmielus, M. Binder Jet 3D Printing—Process Parameters, Materials, Properties, Modeling, and Challenges. *Prog Mater Sci* **2021**, *119*, 100707, doi:10.1016/J.PMATSCI.2020.100707.

43. Yu, S.; Xia, M.; Sanjayan, J.; Yang, L.; Xiao, J.; Du, H. Microstructural Characterization of 3D Printed Concrete. *Journal of Building Engineering* **2021**, *44*, 102948, doi:10.1016/J.JOBE.2021.102948.

44. Kloft, H.; Krauss, H.; Hack, N.; … E.H.-C. and C.; 2020, undefined Influence of Process Parameters on the Interlayer Bond Strength of Concrete Elements Additive Manufactured by Shotcrete 3D Printing (SC3DP). *Elsevier*.

45. Huang, X.; Yang, W.; Song, F.; Zou, J. Study on the Mechanical Properties of 3D Printing Concrete Layers and the Mechanism of Influence of Printing Parameters. *Constr Build Mater* **2022**, *335*, 127496, doi:10.1016/J.CONBUILDMAT.2022.127496.

46. Nair, S.A.O.; Tripati, A.; Neithalath, N. Examining Layer Height Effects on the Flexural and Fracture Response of Plain and Fiber-Reinforced 3D-Printed Beams. *Cem Concr Compos* **2021**, *124*, 104254, doi:10.1016/J.CEMCONCOMP.2021.104254.

47. Ur Rehman, A.; Sglavo, V.M. 3D Printing of Geopolymer-Based Concrete for Building Applications. *Rapid Prototyp J* **2020**, *26*, 1783–1788, doi:10.1108/RPJ-09-2019-0244.

48. Ur Rehman, A.; Sglavo, V.M. 3D Printing of Portland Cement-Containing Bodies. *Rapid Prototyp J* **2022**, *28*, 197–203, doi:10.1108/RPJ-08-2020-0195.

49. Soltan, D.G.; Li, V.C. A Self-Reinforced Cementitious Composite for Building-Scale 3D Printing. *Cem Concr Compos* **2018**, *90*, 1–13, doi:10.1016/J.CEMCONCOMP.2018.03.017.

50. Shakor, P.; Nejadi, S.; Paul, G.; Sanjayan, J.; Nazari, A. Mechanical Properties of Cement-Based Materials and Effect of Elevated Temperature on 3-D Printed Mortar Specimens in Inkjet 3-D Printing. *ACI Mater J* **2019**, *116*, 55–67, doi:10.14359/51714452.

51. Shakor, P.; Nejadi, S.; Paul, G.; Sanjayan, J.; Aslani, F. Heat Curing as a Means of Postprocessing Influence on 3D Printed Mortar Specimens in Powderbased 3D Printing. *Indian Concrete Journal* **2019**, *93*, 65–74.

52. Bredt, J.; Anderson, T.; DB Russell - US Patent 7, 332,537; 2008, undefined Three Dimensional Printing Material System and Method. *Google Patents*.

53. Gibbons, G.; Williams, R.; … P.P.-A. in A.; 2010, undefined 3D Printing of Cement Composites. *Taylor & Francis* **2010**, *109*, 287–290, doi:10.1179/174367509X12472364600878.

54. Zhou, Z.; Buchanan, F.; Mitchell, C.; Dunne, N. Printability of Calcium Phosphate: Calcium Sulfate Powders for the Application of Tissue Engineered Bone Scaffolds Using the 3D Printing Technique. *Mater Sci Eng C Mater Biol Appl* **2014**, *38*, 1–10, doi:10.1016/J.MSEC.2014.01.027.

55. Klammert, U.; Vorndran, E.; Reuther, T.; Müller, F.A.; Zorn, K.; Gbureck, U. Low Temperature Fabrication of Magnesium Phosphate Cement Scaffolds by 3D Powder Printing. *J Mater Sci Mater Med* **2010**, *21*, 2947–2953, doi:10.1007/s10856-010-4148-8.

56. Shakor, P.; Sanjayan, J.; Nazari, A.; Nejadi, S. Modified 3D Printed Powder to Cement-Based Material and Mechanical Properties of Cement Scaffold Used in 3D Printing. *Constr Build Mater* **2017**, *138*, 398–409, doi:10.1016/j.conbuildmat.2017.02.037.

57. C642 Standard Test Method for Density, Absorption, and Voids in Hardened Concrete Available online: https://www.astm.org/c0642-21.html (accessed on 6 November 2024).

58. UNI EN 196-1:2016 - UNI Ente Italiano Di Normazione Available online: https://store.uni.com/uni-en-196-1-2016 (accessed on 6 September 2023).

59. C1723 Standard Guide for Examination of Hardened Concrete Using Scanning Electron Microscopy Available online: https://www.astm.org/c1723-16r22.html (accessed on 4 December 2023).

60. Qiu, M.; Sun, Y.; Qian, Y. Interfacial Bonding Performance of 3D-Printed Ultra-High Performance Strain-Hardening Cementitious Composites (UHP-SHCC) and Cast Normal Concrete. *Journal of Building Engineering* **2024**, *82*, 108268, doi:10.1016/J.JOBE.2023.108268.

61. Horpibulsuk, S.; Horpibulsuk, S. Strength and Microstructure of Cement Stabilized Clay. *Scan Electron Microsc* **2012**, doi:10.5772/35225.

Conclusion

This study validated the mechanical properties and print accuracy of binder jetting 3D-printed (BJ3DP) parts manufactured with different mixtures of coarse and fine siliceous sand combined with quick-setting cement at different water-to-cement (w/c) ratios. This work also investigated the properties of a modified binary cement mix from ordinary Portland cement (OPC) and quick-setting cement (QSC) by using BJ3DP. By intense experimentation and analysis, the primary understanding of the impact of aggregate size, water-to-cement ratio, cement type, and layer thickness on mechanical performance and print accuracy has been established.

Effect of Aggregate Size and Density Variations

The influence of the aggregate size was evident from the difference in density that was observed in the specimens due to different grain distribution. Larger-than-average aggregates resulted in significant improvement in the density. More significantly, porosity was reduced in the specimens with an increase in the w/c ratio, which confirms that the quantity of water plays a basic role in consolidation for printed objects. This development is necessary for the guarantee of the superior performance of BJ3DP components, as higher density and lower porosity tend to mean better mechanical properties.

The trade-off between aggregate size and density indicates that the use of finer aggregates, while it contributes to maintaining uniform density, is problematic from the perspective of print accuracy. Thus, aggregate size has to be selected according to the trade-offs between density, porosity, and print accuracy. These findings provide a platform for additional optimization of the 3D printing material with respect to providing enhanced performance in construction uses.

Influence of Water-to-Cement Ratio on Strength

The mechanical strength of printed specimens correlated positively with the increase in w/c ratio. Both flexural and compressive strengths improved with an increase in water content, revealing that the correct hydration is a controlling parameter for cementitious bond development and attainment of strength. Most notably, variation in grain sizes at the aggregate level did not play a strong role in affecting strength, indicating that water content and cement chemistry play a more deterministic role in governing the final mechanical properties of printed structures. Development over time in strength further validated this correlation, whereby longer curing periods were correlated with significant compressive and flexural strength increases, pointing to the importance of curing conditions post-printing.

Dimensional Precision in BJ3DP

Dimensional precision in binder jetting 3d printing was yet another key topic of research. Samples comprised of smaller aggregates had higher dimensional disparities, for which parameter adjustments had to be done to achieve increased print precision. This finding showcases the role that careful aggregate choice plays during printing, particularly in situations where highly precise prints need to be printed. Minimization of the w/c ratio also proved to have the effect of increased print accuracy, echoing the interplay of mechanical functionality and print resolution when using BJ3DP.

Print accuracy is influenced by several factors including compaction of the powder, and layer deposition uniformity. Optimization of interactions between these parameters should thus be optimized to achieve uniform dimensional accuracy. More advanced monitoring techniques such as real-time layer scanning need to be employed in future work to further enhance print quality and uniformity.

Role of OPC Content in Flow Behavior and Strength

With the modified binary cement blends, the study examined the effect of the concentration of OPC on flow properties and mechanical strength. Flow characteristics

of the less concentrated OPC content cement blends were generally graded as fair to good, whereas OPC at higher concentration yielded more cohesive and less flowing blends. Hausner ratio (HR) and Carr's index (CI) values confirmed this tendency and demonstrated that OPC content has a direct impact on powder flow dynamics. These findings are significant for powder composition optimization in BJ3DP to maintain the maximum degree of flowability and deposition uniformity.

A major observation was that the OPC concentration had a direct influence on printed specimen density. As the ratio of OPC increased above that of QSC, the higher specific gravity of OPC became a dominant factor for increased overall density and mechanical performance. This relationship is extremely relevant in BJ3DP, where density variation can be a cause of final part performance variation.

From the strength properties perspective, Mix VII exhibited excellent flexural strength of 1.9 MPa at 7 days and then increased to 2.7 MPa at day 28. The progressive enhancement in mechanical properties over time testifies to the effectiveness of the selected binary cement composition in developing integrity-rich BJ3DP parts. Besides that, an optimum mix of OPC, QSC, and sand was obtained with the proportion 35:5:60 wt%, beyond which higher cement content led to falling strength improvement. This work would suggest that higher cement content might negatively impact the structural properties of the printed structure, perhaps via greater shrinkage, cracking, or lower cohesiveness of powder particles.

Influence of Layer Thickness on Strength

Another critical aspect of the research was the effect of layer thickness on mechanical performance. There was a clear inverse relationship between layer thickness and strength, in which greater layer thickness resulted in lower mechanical performance. Microscopy revealed that this effect was associated with void formation, in which greater layer thicknesses resulted in greater voids, undermining the structural integrity of the material. This observation highlights the necessity to optimize layer thickness during printing to enhance material strength. Reducing layer thickness was

found to minimize voids, thus mechanical properties were enhanced and a more uniform distribution of the material in the printed specimen was obtained.

Future Directions and Applications

Mix-II with improved mechanical properties at increasing water-to-cement ratio, is a potential selection for BJ3DP applications where strength and durability are the overriding requirements. Similarly, Mix VII also demonstrated reasonable mechanical possessions in the form of flexural strength, which can be used for structural applications with demands of improved load-carrying capacities. The outcome of the study on the optimization of layer thickness also contributes to the advancement of BJ3DP technology by the implication of cautious print parameter selection. From a general perspective, these findings create opportunities for further research in BJ3DP of cementitious materials. More binder formulations, alternative aggregates, and the use of additives for enhancing printability and mechanical strength must be investigated in future studies. Also, the influence of curing conditions, environmental exposure, and post-processing treatments on long-term durability must be investigated to determine the viability of 3D-printed cement structures for real-world applications.

By the methodical experimentation of material mixtures and printing parameters, this research contributes to the growing body of literature on digital construction technologies. Optimization steps identified herein will help improve BJ3DP processes for producing high-performance, precisely printed cement components with ubiquitous application in construction, infrastructure, and industrial manufacturing.

As BJ3DP technology continues to evolve, the ability to customize material compositions and printing parameters will be instrumental in pushing the boundaries of additive construction manufacturing. The results of this study offer a foundation for future generations of 3D-printed concrete by offering actionable information on improving the structural integrity, printing accuracy, and material performance of large-

scale applications. Lastly, ongoing BJ3DP method development will contribute to the attainment of ever more sustainable, efficient, and economical construction practices in the years to come.

Appendix – Selective Alkali Activation of Limestone for Additive Manufacturing in Construction: Influence of Alkali Concentration on Physical and Mechanical Properties

"Selective Alkali Activation of Limestone for Additive Manufacturing in Construction: Influence of Alkali Concentration on Physical and Mechanical Properties",

Mursaleen Shahid[a], Alexandre Pierre[b], Annelise Couture[b], Vincenzo M. Sglavo[a]

a. Department of Industrial Engineering, University of Trento, 38123 Trento, Italy

b. CY Cergy Paris Université, L2MGC, CERGY F-95000, France

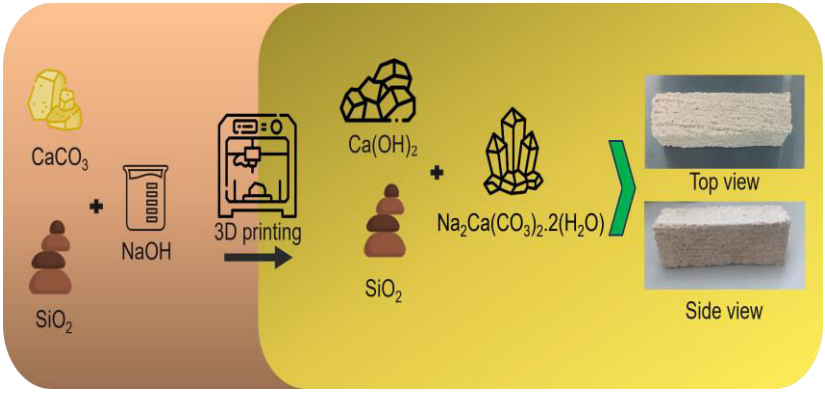

Figure I: Graphical Abstract

6.1 Abstract

Alkali-activated binders are gaining much importance in the construction industry because of their environmental and mechanical advantages. This paper focuses on the selective limestone activation (SLA) using aqueous sodium hydroxide solutions to be used as non-hydraulic binder material. This study investigates the mechanical performance of 3D-printed specimens cured at 45°C produced with different NaOH concentrations. The results show that mechanical strength and physical properties are influenced by NaOH concentration, the strength decreasing at higher sodium hydroxide loads.

6.2 Introduction

The construction industry is a major contributor to the global economy, but it has been mainly relying on traditional technologies although the trend is changing after the digitalization in industry after the 1970's. Based on this, Additive Manufacturing (AM) has achieved significant progress in the construction industry, bringing innovative approaches to the design and production of building elements. AM is a process to fabricate physical objects directly from computer-aided design models in a layer-by-layer manner [1,2]. Among the different additive manufacturing techniques that can be used in construction, as shown in Figure II, selective cement activation is a process of interest in the field of selective particles bed binding.

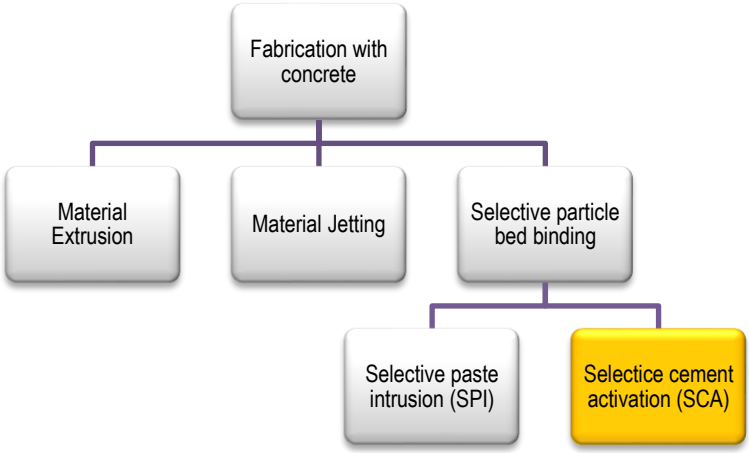

Figure II:Additive manufacturing processes for concrete fabrication

The "selective particles bed binding" technique can be divided into two methods[3]. In the so-called "selective paste intrusion", a component is fabricated by spreading thin layers of aggregate, followed by the local application of cement paste to achieve hardening [4]. The second method, "selective cement activation (SCA)", relates to local hardening obtained by spraying water on a layer of mixed cement and aggregate [5–8]. This process is composed of two main steps. In the first one, the dry powder is uniformly distributed as a thin layer with the aid of a roller or doctor blade of the required layer thickness. The second step involves the activation of the powder by the liquid phase sprayed through a travelling nozzle. The technique when used for the activation of limestone is called selective limestone activation (SLA).

Lowke et al.[9] examined the use of water in selective cement activation in two configurations: (a) spraying very small droplets (in the picoliter range) onto the particles bed or (b) jetting water at variable pressure. The strength achieved without post-treatment reaches 15.5 MPa, which classifies the material as lightweight concrete with a bulk density of 1.6 g/cm³. The authors did observe that higher water-to-cement ratios decrease porosity and increase strength but reduce shape accuracy. Similarly,

larger aggregate particle sizes gave superior strengths with loss of shape accuracy, while higher water jet pressure had insignificant effects on strengths and shape accuracy, but increased porosity and reduced homogeneity. Lowke et al. [10] extended the original model based on the Washburn equation for the time-dependent prediction of fluid intrusion into particle beds. Their study indicated that the initial fluid penetration (capillary intrusion) is very rapid and almost spontaneous with no significant influence from the particle size, followed by further capillary action, which is responsible for inter-layer bonding and geometric precision.

Shahid et al.[11] focused on the behaviour of a blended binary cement mixture, consisting of ordinary Portland cement (OPC) and quick-setting cement in binder jetting 3D printing. It was observed that OPC content in the dry mixtures affected the flow properties, lower OPC concentration showing better flowability. Higher OPC content enhanced the density of the 3D-printed specimens, together with the mechanical properties. Salari et al.[12] used magnesium oxychloride cement-based material and investigated the interaction of powder and binder to point out how the binder droplets interact with the powder bed to affect the quality of the printed blocks. The mechanical strength was generally correlated with the volume of cementitious bonds; finer particles provided larger surface area for bonding, thereby improving the resistance. In another work, Ur Rahman et al. [13] focused on the 3D printing of geopolymer-based concrete: metakaolin was selectively activated using an alkaline activated solution and the maximum modulus of rupture obtained was 4.4 MPa.

Despite the growing interest in materials obtained by alkali activation, very little research has been focused on the alkali activation of calcium carbonate-containing compounds like, for example, limestone. It was through a patent published in 2006 that early investigations into the use of limestone as a precursor, activated by sodium hydroxide without the addition of silicate phases, came [14]. Studies concerned with recent cement production have increasingly focused on its minimal environmental impact. Limestone offers considerable advantages due to its structural purity, availability, and cost-effectiveness compared to conventional cement. Many researchers have explored its potential to act as a substitute for cement for this reason. An inceptive study considered aspects such as CO_2 emissions, temperature effects, workability, density, shrinkage, compressive strength, mortar strength, and porosity

[15]. From the results, it was concluded that higher percentages of limestone contributed largely to CO2 emissions reduction, and with 10% increase in limestone powder, the percentage reduction in emission was about 8-9%. It was also found that the replacement strengthens the distribution and workability while reducing porosity and shrinkage, the compressive strength anyway decreasing. In addition, for mortar and concrete, the limestone particle size has a minor effect on all the levels of replacement. Nevertheless, studies on the development of alkali activation of calcium carbonate are few [16–18].

The present study investigates the properties of 3D-printed limestone material activated with different NaOH water solutions. The phase stability, mineral composition and mechanical properties were studied. The results obtained from this work allow for a better understanding of the influence of NaOH concentration on properties that make the printed limestone materials suitable for applications in the construction industry.

6.3 Materials and Methods

A customized 3D printer was utilized for the dry powder supply and the liquid binder supply. A positive displacement metering valve MV 250 was integrated into the printer to ensure accurate binder deposition using a 700 ETC+ controller thus enhancing the precision in the specimens fabrication. The hopper was used for the dry powder supply while the binder was precisely sprayed in proper places to be effectively activated using a nozzle operating using a positive displacement valve.

The printed samples had dimensions of 160 mm x 40 mm x 40 mm and were produced with a layer thickness of 4 mm and a hatch distance of 4 mm. The velocity of the powder spread was 700 mm/min and the liquid binder was also operated at the same velocity while maintaining the pressure at 2 – 4 bar using a 700 ETC+ valve controller.

The dry mix included limestone (BETOCARB P2-MX from OMYA France containing 98.4% calcite) - density 2700 kg/m^3 - and standardized sand - density 2640 kg/m^3 - (in accordance with EN 196-1 [19]) in a ratio of 1:3.

The particles size distribution of limestone and standardized sand was analysed by the laser scattering technique (Partica LA-960V2 - Horiba Scientific) (Figure III), the distibutions being in agreement with the technical data provided by the suppliers.

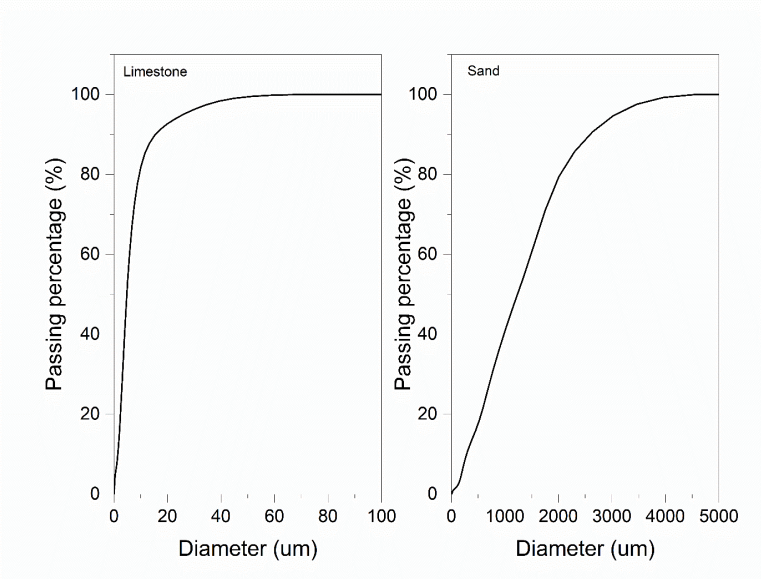

Figure III: Particle size distribution for limestone and sand

Three different concentrations of NaOH in water solution (12.9 mol/l, 15.6 mol/l and 19 mol/) were considered in the present work. The solutions were prepared in an airtight polypropylene Erlenmeyer flask and stored under a controlled hood, along with the other materials, at 20°C for at least 24 h. The properties of the liquid binders were analysed using the Anton Paar rheometer MCR 102, the relationship between shear stress and shear strain being shown in Figure IV.

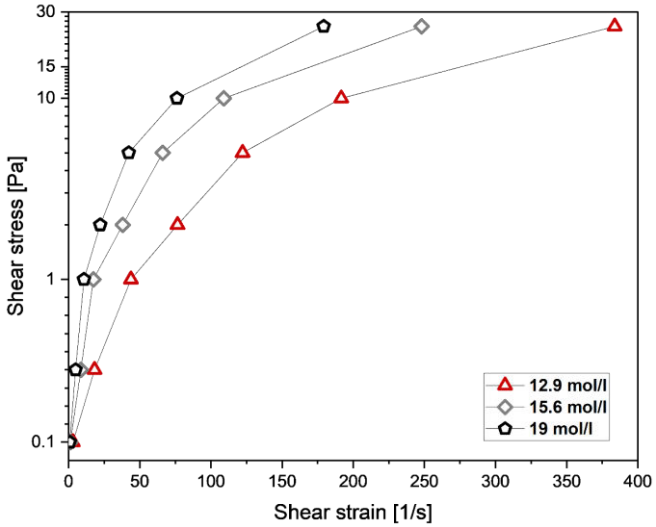

Figure IV: Rheological behaviour of the NaOH water solutions

Printing was carried out by depositing successive 4 mm thick layers (ten) of a mixture of dry limestone and normalized sand, each one activated using a NaOH water solution over a defined area of 160 mm × 40 mm. The specimens, after printing, were first cured in situ on the powder bed for 24 h, followed by an additional curing period of 48 h at ambient temperature. After printing and curing, the excess powder was firstly removed (de-powdering). Smoothening of the specimens was carried out by using grit paper to ensure balanced edges for mechanical testing. The printed specimens were dried at 45^{o}C for 96 h and 600 h before the mechanical testing for the curing time 7 days and 28 days respectively.

The weight loss of the printed specimens was measured after post-processing to the end of curing time (28 days).

The flexural strength of the cured specimens was measured by three-point bending at curing times of 7 and 28 days as per norm EN-196-1, using a 3R Quantech apparatus with a loading rate of 50 N/s and a span of 100 mm. The resulting values were the mean of three individual values.

The porosity of the printed specimens was measured by the Archimedes' method, using portions of the specimens obtained from the mechanical tests. Ethanol was used instead of water to avoid possible dissolution. These measurements were performed 1 to 2 days after the mechanical tests.

The 3D printed specimens were examined by scanning electron microscopy (SEM, I-Mat, CY Cergy Paris Université). The microstructure of fracture surfaces (collected from samples used in the mechanical tests) was observed using a Gemini 300 microscope (ZEISS) in high vacuum mode with a voltage of 2 kV and a working distance of 7.5 mm. In addition to SEM, EDX analysis was performed on different areas of the printed specimen. Sodium and calcium quantification was obtained by the PB-ZAF method.

XRD analysis was carried out with a D8 Advanced instrument (Bruker) with a copper anode ($\lambda_{(K\alpha)}$=1.5406 Å). Scans were run with a step of 0.0167° and a counting time of 0.5715 s/step from 2θ = 10° to 2θ = 90°.

Differential thermal analysis and thermogravimetric analysis (DTA-TGA) were carried out with an STA 449 F1 Jupiter analyzer (Netzsch) from 25°C to 1000°C with a heating rate of 10°C/min under a nitrogen flux (50 mL/min). All the tests were performed using approximately 110 mg of powder.

6.4 Results

6.4.1 Weight loss after printing

The weight loss results are shown in Figure V as a function of NaOH concentration up to 28 days aging. A very fast loss occurs during the first two days, most likely caused by moisture evaporation and initial curing reactions. The 19 mol/l NaOH sample shows the least weight loss and levels off at around −5.5%, while the values for the 15.6 mol/l and 12.9 mol/l specimens level off at around −6.7% and −8.2%, respectively[20]. By increasing the NaOH concentrations, the water quantity decreases, and so the weight loss, since the weight loss is due to evaporation of the free water that is not required for the curing process. Drying is compulsory to eliminate free water and to improve mechanical strength. However, rapid drying at higher temperature results in a decrease in the strength, possibly due to the development of stabilizing phases which

better resist further dehydration [18,20]. All the samples evidence that, after 10 days, there is a minimal change in weight, this meaning that most of the reactions and drying processes had stabilized by then. Overall, larger NaOH concentration appears to enhance the stability of the samples over time.

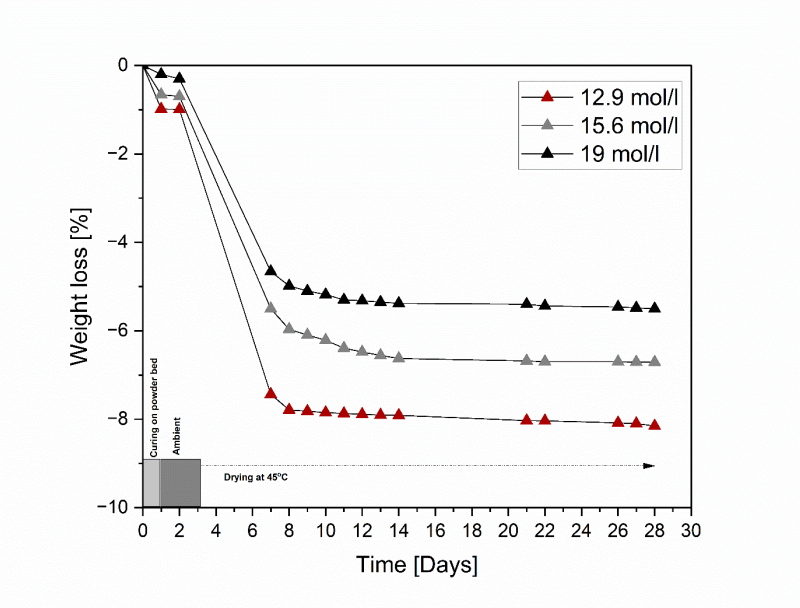

Figure V: Weight loss of printed samples after printing (24 h curing on the powder bed, 48 h curing at ambient conditions and then drying at 45 C)

6.4.2 Identification of the reaction products

The XRD spectra of the 3D-printed specimens are shown in Figure VI.

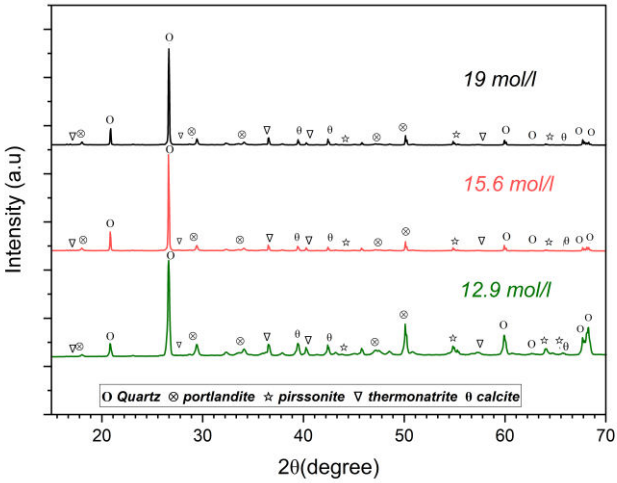

Figure VI: XRD analysis patterns and identified crystalline phases

All the XRD patterns show the peaks of quartz related to the presence of standardized sand and calcite from unreacted limestone in the 3D-printed samples. Irrespective of the NaOH molarity, the reaction products are thermonatrite (Na_2CO_3, H_2O), portlandite ($Ca(OH)_2$) and pirssonite ($Na_2Ca(CO_3)_2$, $2H_2O$). Moreover, calcite peaks are visible. They could be associated with unreacted limestone.

Initially, limestone ($CaCO_3$) dissolves in NaOH to form $Ca(OH)_2$ and soluble Na_2CO_3 (Eq. 1). The freed Ca^{2+} and CO_3^{2-} then recombine with Na^+ and H_2O to precipitate hydrated sodium-calcium carbonate (pirssonite, $Na_2Ca(CO_3)_2 \cdot 2H_2O$, Eq. 2). At elevated Na^+ concentrations, sodium carbonate monohydrate (thermonatrite, $Na_2CO_3 \cdot H_2O$) also forms (Eq. 3), competing with pirssonite.

TGA-DTA diagrams of samples printed with different NaOH water solutions are shown in Figure VII. Below 200°C, the observed peaks were attributed to dissociation reaction

(water release) in thermonatrite (around 112°C) and pirssonite (around 170°C) [21] according to the following reactions, respectively.

$Na_2CO_3, H_2O \rightarrow Na_2CO_3 + H_2O$ (1)

$Na_2Ca\ (CO_3)_2, 2H_2O \rightarrow Na_2Ca\ (CO_3)_2 + 2H_2O$ (2)

The peak around 440°C was related to the dehydration of portlandite (equation 3) and consistent with the literature [22].

$Ca\ (OH)_2 \rightarrow CaO + H_2O$ (3)

Upper 600°C, the peaks were linked to the decarbonation of calcareous compounds: nyerereite ($Na_2Ca\ (CO_3)_2$ from dehydration of pirssonite) [21] and limestone, according to the following reactions.

$Na_2Ca(CO_3)_2 \rightarrow Na_2CO_3 + CaO + CO_2$ (4)

$CaCO3 \rightarrow CaO + CO_2$ (5)

The peaks without weight loss, at 386°C and around 568°C were associated with crystallographic transformations in nyerereite structure (low-temperature form to high-temperature form) [23] resulting from dehydration of pirssonite and to allotropic transformation of quartz ($\alpha \leftrightarrow \beta$) [24].

The identified compounds (i.e. thermonatrite, pirssonite, portlandite, calcite and quartz) were previously identified with XRD analysis. This indicates that all the reaction products are crystallized whatever the NaOH concentration. The main differences between samples came from the TGA curves and so, from the quantities of reaction products. Table I summarises all the weight loss measured on TGA curves and the final weight loss after curing (i.e. free water evaporation).

Table I: Weight loss and water balance of prismatic specimens under different concentrations of NaOH

NaOH molarity (mol/l)		12.9	15.6	19.0
Related products and temperature range (°C)	Thermonatrite (25-140)	1.8	1.1	1.3
	Pirssonite (140-335)	0.6	3.1	1.9
	Portlandite (335-560)	1.6	1.5	1.5
	Carbonated phases (560-1100)	9.1	10.5	9.5
Weight loss from curing (%)		8.2	6.7	5.5
Total water (%)		12.2	12.4	10.2

The amount of portlandite appears to remain stable, regardless of the NaOH solution's molarity while the amount of the other reaction products varies with the molarity.

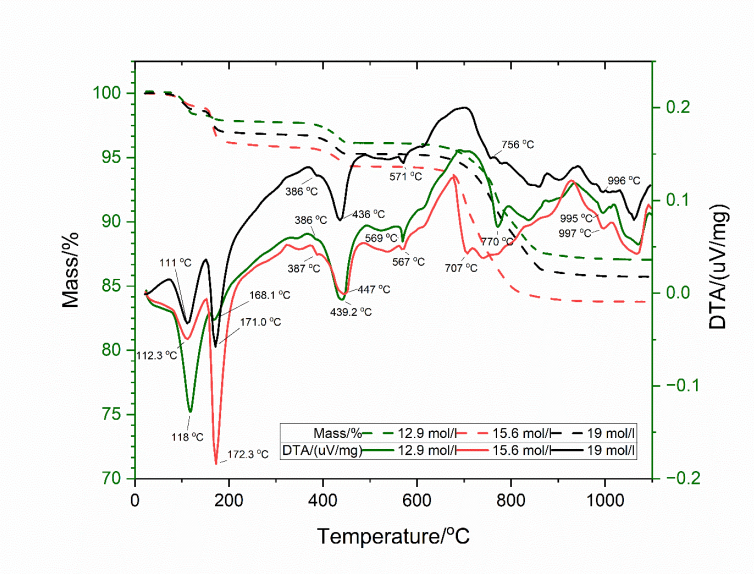

Figure VII: TGA/DTA analysis diagrams

6.4.3 SEM analysis

SEM images of the printed specimen with the different NaOH solutions are shown in Figure VIII.

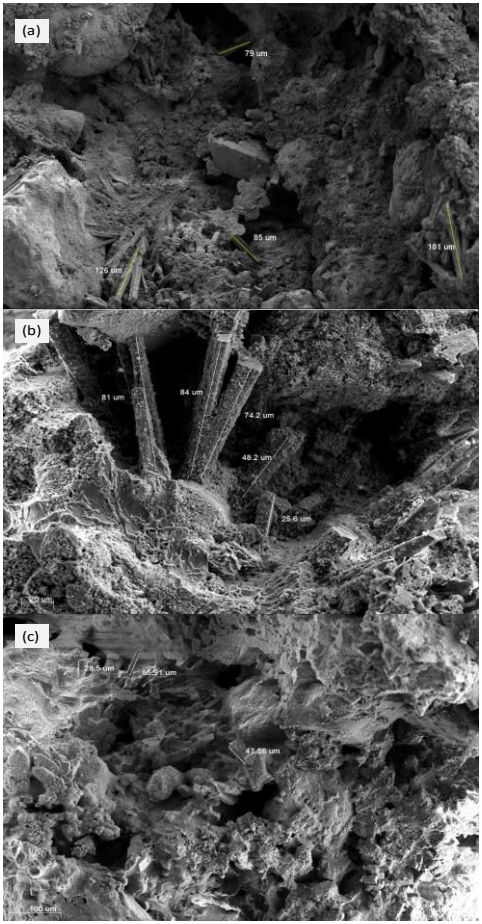

Figure VIII: SEM images of the 3D printed sample with different NaOH concentrations: (a) 12.9 mol/l, (b) 15.6 mol/l and (c) 19 mol/l respectively

Different microstructures were observed, regardless of the used NaOH concentration, including dense areas, grainy areas and needles of different lengths. These microstructures were associated with the compounds identified by XRD and thermal analysis (i.e. thermonatrite, pirssonite, portlandite and calcite, Figure VI and Figure VII). To link a microstructure to a compound, a point-counting procedure was conducted. EDX analysis was performed in selected areas, identifying and quantifying the elements present. The quantification was done in atomic percentages using the standardless PB-ZAF method in the EDX software. Then, the Na:Ca ratios are calculated and compared to the theoretical ratios of the identified compounds. They were: 1.15 for pirssonite and 0.00 for calcite and/or portlandite. Figure IX shows the selected areas for the EDX analysis.

The Na:Ca ratios were 0.1, 1.6, 2.3 and 3.1 for areas III, I, IV and II, respectively. The shape and the Na:Ca ratio of area III are very close to the shape and values reported in the literature [19] that confirm unreacted or partially reacted calcite. The shape of areas I and II were similar but their Na:Ca ratio is different. This suggests that their degree of crystallisation might be different or that these crystals may have different natures. They could be related to pirssonite and/or thermonatrite. Area IV presents a

different shape and an intermediate Na:Ca ratio, indicating a possible mix of the reaction products (i.e. portlandite; pirssonite and thermonatrite).

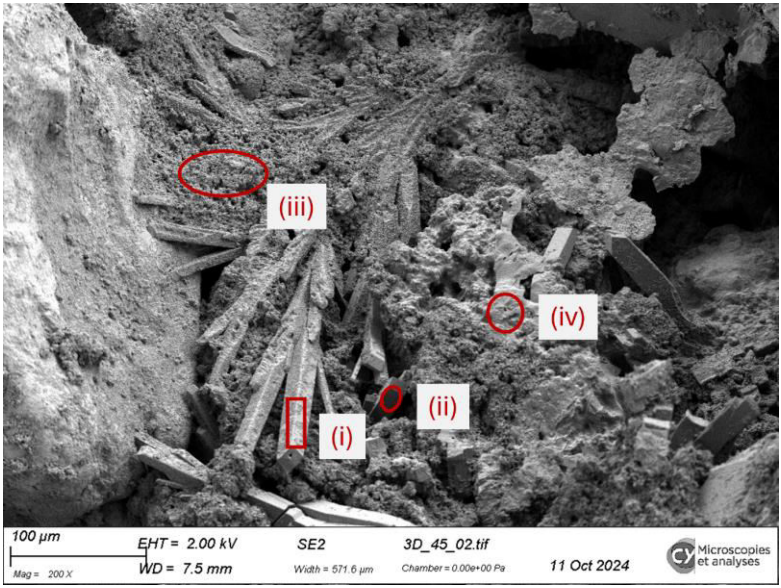

Figure IX: SEM-EDX analysis of sample printed with 12.9 mol/l NaOH concentration

Different microstructures were observed, regardless of the used NaOH concentration, including dense areas, grainy areas and needles of different lengths.

6.4.4 Porosity

The porosity and the density of the printed specimens are shown in Table II.

Table II: Density and porosity of the 3D printed specimens

Concentration mol/l	Density (g/cm^3)	Porosity (%)
12.9	1.6±0.2	33±1
15.6	1.6±0.1	32±2
19	1.8±0.1	30±4

The total porosity and the density of the specimens are about 31% and 1.7 g/cm^3, respectively, regardless of the concentration of NaOH. The porosity value is larger and the density is slightly smaller than that found in conventional mortar after 28 days (18% and 2.0 g/cm^3) [25]. This important difference very likely depends on the method used for preparing the material and the different water-to-binder ratios used in 3D printing [26].

6.4.5 Mechanical Properties

Flexural strength at 7 and 28 days is presented in Figure X.

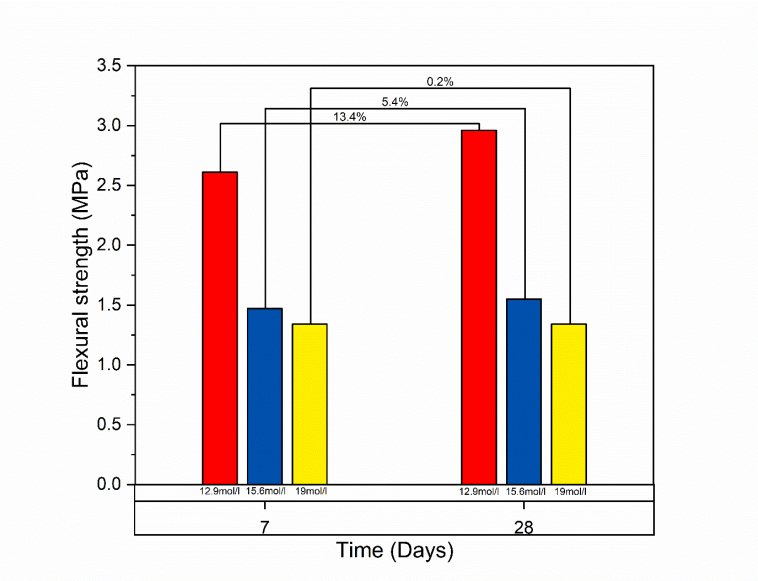

Figure X: Flexural strength vs curing time; the strength increase between 7 and 28 curing days is shown

Lowering alkalinity lessens the dissolution of $CaCO_3$ but increasing binder penetration from lower viscosity creates more homogeneous network. Increased alkalinity improves dissolution of $CaCO_3$ but increased viscosity slows down binder flow. The precipitated phases, as identified by XRD and SEM, form a discontinuous microstructure, which leads to incomplete and weak interparticle bonding.

The samples printed with a 12.9 mol/L NaOH concentration show an increased flexural strength by 13.4% from 7 to 28 days of curing. The results of flexural strength can be related to the penetration dynamics of the NaOH solution, which in turn is dependent on its rheological properties. The rheological behaviour of a solution, including its properties of flow and viscosity, makes it more challenging to penetrate directly into a powder bed as represented by the equation derived from Hagen-Poiseuille's law [27]:

$$v = \frac{d(l)}{d(t)} = \frac{r\,\gamma\,cos\,\varphi}{4\,\mu\,l(t)} \qquad (8)$$

where v is the penetration velocity, l penetration length, r the pore radius, γ the surface tension of the air-liquid interface, φ the contact angle between the solid and liquid particles, μ the dynamic viscosity of the liquid and t is time.

Equation (8) suggests that the penetration velocity *v is* inversely proportional to the length *l(t)* and the solution's viscosity. From Figure 3, it is obvious that the 12.9 mol/l NaOH solution has the lowest slope, which means the lowest viscosity. Low viscosity is desirable for penetration into the powder bed since it can flow into fine pores and capillaries easily.

The gain in strength is minimal when the results of printed samples cured after 7 and 28 days are compared. This suggests that the mechanical properties are influenced by the NaOH concentrations, capillary-driven penetration and curing dynamics. Properties of printed specimens can be further optimized using these factors.

Since this process is selective activation using 3D printing was done with in a controlled environment—where the printer is enclosed inside the glass chamber—the application of these higher concentrations of NaOH activating solutions was safely contained within the laboratory setting. For large-scale industrial use, careful handling procedures and safety measures would need to be in place to mitigate the dangers of using such high molarity activating solutions.

6.5 Conclusion

The present work investigates the effects of the concentration of sodium hydroxide water solution on the particles bed bonding during selective activation of limestone. The results reveal the influence of NaOH concentration on the mechanical properties of the printed materials, despite the porosity and density remain similar for all concentrations. XRD analysis shows progressive mineralogical changes, involving portlandite formation at all concentrations and pirssonite reduction with higher NaOH loads. SEM images confirm always variable microstructures, such as dense regions, grainy textures and needle-like formations with different lengths. Flexural strength decreases with NaOH concentration thus pointing out how critical is this parameter to optimize the mechanical properties of selective limestone-activated materials printed with selective activation.

References

1. Bhushan, B.; Caspers, M. An Overview of Additive Manufacturing (3D Printing) for Microfabrication. *Microsystem Technologies* **2017**, *23*, 1117–1124, doi:10.1007/s00542-017-3342-8.
2. Doyle, M.; Agarwal, K.; Sealy, W.; Schull, K. Effect of Layer Thickness and Orientation on Mechanical Behavior of Binder Jet Stainless Steel 420 + Bronze Parts. *Procedia Manuf* **2015**, *1*, 251–262, doi:10.1016/J.PROMFG.2015.09.016.
3. Lowke, D.; Dini, E.; Perrot, A.; Weger, D.; Gehlen, C.; Dillenburger, B. Particle-Bed 3D Printing in Concrete Construction – Possibilities and Challenges. *Cem Concr Res* **2018**, *112*, 50–65, doi:10.1016/j.cemconres.2018.05.018.
4. Pierre, A.; Weger, D.; Perrot, A.; Lowke, D. Penetration of Cement Pastes into Sand Packings during 3D Printing: Analytical and Experimental Study. *Mater Struct* **2018**, *51*, 22, doi:10.1617/s11527-018-1148-5.
5. Shakor, P.; Sanjayan, J.; Nazari, A.; Nejadi, S. Modified 3D Printed Powder to Cement-Based Material and Mechanical Properties of Cement Scaffold Used in 3D Printing. *Volume 138, Pages 398 - 409* **2017**, *138*, 398–409, doi:10.1016/j.conbuildmat.2017.02.037.
6. Ingaglio, J.; Fox, J.; Naito, C.J.; Bocchini, P. Material Characteristics of Binder Jet 3D Printed Hydrated CSA Cement with the Addition of Fine

Aggregates. *Constr Build Mater* **2019**, *206*, 494–503, doi:10.1016/j.conbuildmat.2019.02.065.

7. Xia Ming and Nematollahi, B. and S.J. Compressive Strength and Dimensional Accuracy of Portland Cement Mortar Made Using Powder-Based 3D Printing for Construction Applications. In Proceedings of the First RILEM International Conference on Concrete and Digital Fabrication – Digital Concrete 2018; Wangler Timothy and Flatt, R.J., Ed.; Springer International Publishing: Cham, 2019; pp. 245–254.
8. Weger, D.; Lowke, D.; Gehlen, C. 3D Printing of Concrete Structures Using the Selective Binding Method – Effect of Concrete Technology on Contour Precision and Compressive Strength.; December 2016.
9. Lowke, D.; Talke, D.; Dressler, I.; Weger, D.; Gehlen, C.; Ostertag, C.; Rael, R. Particle Bed 3D Printing by Selective Cement Activation – Applications, Material and Process Technology. *Cem Concr Res* **2020**, *134*, doi:10.1016/j.cemconres.2020.106077.
10. Mai, I.; Lowke, D.; Perrot, A. Fluid Intrusion in Powder Beds for Selective Cement Activation – An Experimental and Analytical Study. *Cem Concr Res* **2022**, *156*, 106771, doi:10.1016/j.cemconres.2022.106771.
11. Shahid, M.; Sglavo, V.M. Binder Jetting 3D Printing of Binary Cement—Siliceous Sand Mixture. *Materials 2024, Vol. 17, Page 1514* **2024**, *17*, 1514, doi:10.3390/MA17071514.
12. Salari, F.; Bosetti, P.; Sglavo, V.M. Binder Jetting 3D Printing of Magnesium Oxychloride Cement-Based Materials: Parametric Analysis of Manufacturing

Factors. *Journal of Manufacturing and Materials Processing 2022, Vol. 6, Page 86* **2022**, *6*, 86, doi:10.3390/JMMP6040086.

13. Ur Rehman, A.; Sglavo, V.M. 3D Printing of Geopolymer-Based Concrete for Building Applications. *Rapid Prototyp J* **2020**, *26*, 1783–1788, doi:10.1108/RPJ-09-2019-0244.
14. Philippe Pichat Fabrication d ' Un Matériau Solide à Partir d' Un Hydroxyde Alcalin 2006.
15. Leeuwen, R. van; Kim, Y.-J.; Sriraman, V. The Effects of Limestone Powder Particle Size on the Mechanical Properties and the Life Cycle Assessment of Concrete. *Journal of Civil Engineering Research* **2016**, *6*, 104–113, doi:10.5923/J.JCE.20160604.03.
16. Ortega-Zavala, D.E.; Santana-Carrillo, J.L.; Burciaga-Díaz, O.; Escalante-García, J.I. An Initial Study on Alkali Activated Limestone Binders. *Cem Concr Res* **2019**, *120*, 267–278, doi:10.1016/J.CEMCONRES.2019.04.002.
17. Avila-López, U.; Almanza-Robles, J.M.; Escalante-García, J.I. Investigation of Novel Waste Glass and Limestone Binders Using Statistical Methods. *Constr Build Mater* **2015**, *82*, 296–303, doi:10.1016/J.CONBUILDMAT.2015.02.085.
18. Cousture, A.; Renault, N.; Ndiaye, K.; Gallias, J.L. Mechanisms of Alkali-Activation of Limestone: Reaction Kinetics and Influence of Drying Parameters. *Constr Build Mater* **2024**, *441*, 137501, doi:10.1016/J.CONBUILDMAT.2024.137501.
19. EN 196-1:2016 - UNI Ente Italiano Di Normazione Available online: https://store.uni.com/en-196-1-2016 (accessed on 18 June 2024).

20. Couture, A.; Renault, N.; Gallias, J.-L.; Ndiaye, K. Study of a Binder Based on Alkaline Activated Limestone. *Constr Build Mater* **2021**, *311*, 125323, doi:10.1016/j.conbuildmat.2021.125323.

21. Bottcher, M.E.; Gehlken, P.L. Dehydration of Natural Gaylussite (Na2Ca (CO3)(2) Center Dot 5H (2) O) and Pirssonite (Na2Ca (CO3)(2) Center Dot 2H (2) O) as Illustrated by FTIR Spectroscopy. *Neues Jahrbuch fur Mineralogie-Monatshefte* **1996**, 73–91.

22. Menéndez, E.; Andrade, C.; Vega, L. Study of Dehydration and Rehydration Processes of Portlandite in Mature and Young Cement Pastes. *J Therm Anal Calorim* **2012**, *110*, 443–450, doi:10.1007/S10973-011-2167-4/FIGURES/8.

23. Zucchini, A.; Gavryushkin, P.N.; Golovin, A. V.; Bolotina, N.B.; Stabile, P.; Carroll, M.R.; Comodi, P.; Frondini, F.; Morgavi, D.; Perugini, D.; et al. Crystal Structure of Nyerereite: A Possible Messenger from the Deep Earth. *American Mineralogist* **2022**, *107*, 2054–2064, doi:10.2138/am-2022-8106.

24. Raman, C. V.; Nedungadi, T.M.K. The α-β Transformation of Quartz. *Nature 1940 145:3665* **1940**, *145*, 147–147, doi:10.1038/145147a0.

25. Couture, A.; Renault, N.; Ndiaye, K.; Gallias, J.L. Mechanisms of Alkali-Activation of Limestone: Reaction Kinetics and Influence of Drying Parameters. *Constr Build Mater* **2024**, *441*, 137501, doi:10.1016/J.CONBUILDMAT.2024.137501.

26. Shahid, M.; Sglavo, V.M. Effect of Water-to-Quick Setting Cement Ratio and Aggregate Size on Mechanical Properties and Dimensional Accuracy of Binder Jetting 3D-Printed Bodies. *Open Ceramics* **2024**, *20*, doi:10.1016/j.oceram.2024.100704.

27. Poiseuille (M. le docteur, J.-L.-M. *Experimental Investigations Upon the Flow of Liquids in Tubes of Very Small Diameter*; E. C. Bingham, Ed.; 1940; Vol. 1;.

Scientific Publications

Shahid M, Sglavo VM (2024) Binder Jetting 3D Printing of Binary Cement—Siliceous Sand Mixture. Materials 2024, Vol 17, Page 1514 17:1514. https://doi.org/10.3390/MA17071514

Shahid M, Sglavo VM (2024) Effect of water-to-quick setting cement ratio and aggregate size on mechanical properties and dimensional accuracy of binder jetting 3D-printed bodies. Open Ceramics 20:. https://doi.org/10.1016/j.oceram.2024.100704

Shahid M, Pierre A, Cousture A, Sglavo VM.(2025) Selective Alkali Activation of Limestone for Additive Manufacturing in Construction: Influence of Alkali Concentration on Physical and Mechanical Properties. Applied Sciences.; 15(8):4453. https://doi.org/10.3390/app15084453

Participations to Congresses, Schools and Workshops

3D Printing of ceramics workshop ACERS, additive manufacturing methods, applications, emerging technologies, commercial manufacturing (April-2022, Virtual)

Young ceramists additive manufacturing 2022, the need of the industry, the required skills, and how they can be evaluated in order to build a skills framework for R&D experts on Additive Manufacturing (Nov-2022, Barcelona)

Young ceramists additive manufacturing 2023, additive manufacturing of advanced ceramics materials and its need in industry. (29th Aug 23 – 1st Sep 23, Leoben)

Young ceramists additive manufacturing 2024, additive manufacturing of advanced ceramics materials and its need in industry. (5th May –9th May 24, Tampere)

NON-CONVENTIONAL SINTERING: SCIENCE AND TECHNOLOGY, **Summer School** (5th June 23 – 7th June 23, Trento Italy)

Acknowledgement

I would like to thank Prof. Vincenzo M. Sglavo, Department of Industrial Engineering, University of Trento, for his invaluable advice, precious guidance, and constant encouragement throughout my research. His wisdom, patience, and motivation were the door-opening keys that molded this work into what it has become today, and I am truly blessed to have been given the opportunity to learn from him.

I also have an equally indebted to the entire staff of the Glass and Ceramics Laboratory of the University of Trento. Their technical know-how, collaborative work, and provocative discussion made this research in the laboratory significantly richer beyond the laboratory.

I owe a debt of gratitude to my parents all my life for their unconditional love, support, and encouragement throughout this journey. Their belief in me has been the motivating factor.

I would also like to thank my wife sincerely. Her patience, tolerance, and unflinching support have been priceless. Her faith in me and her encouragement at each step have not only enabled me to overcome obstacles but have also made this process outstanding.

Lastly, I thank the University of Trento for providing access to the facilities, resources, and learning environment conducive to this research. All, however small, have contributed to the completion of this thesis.